Silicon nitride deformable mirrors for focus and spherical aberration correction in micro-optical systems
by Phillip Alexander Himmer

A dissertation submitted in partial fulfillment of the requirements for the degree of Doctor of Philosophy m Engineering
Montana State University

Abstract:
Laser beam scanning systems benefit from dynamic focus control and aberration correction using a deformable mirror, enabling 3D real-time scanning. Designed for focus and spherical aberration control in optical beam scanning systems, these mirrors are capable of video rate bandwidths allowing real-time 3D imaging in micro-optical scanning systems. Field curvature aberration can also be corrected with the same mirror. Previous work with polysilicon deformable mirrors validated the concept of using specialized deformable optics in beam scanning systems. Fabrication of micro-optics in this dissertation was achieved using a modified surface micromachining technique with silicon nitride replacing polysilicon as the structural material. A bulk anisotropic silicon etch following a PSG release etch allows the creation of a variable cavity depth, overcoming the typical deformation limitations of standard surface micromachining. To perform as desired, parabolic curvature of the mirror surface is required with the ability to introduce positive and negative quartic curvature. Analytical theory showed that deformed simply supported plates have curvature closer to parabolic than deformed clamped plates. Segmentation and thinning of the perimeter was done to in order to emulate this simply supported boundary. Two annular actuation zones were implemented to give independent control over the second and fourth order curvatures. It was found that residual stress present in the silicon nitride structural plate improved the surface curvature and mechanical resonance at the expense of a larger actuation pressure. Mirrors with diameters of 1500, 1000, 750, and 300μm were built and tested. Zonal actuation with annular electrodes proved successful in providing sufficient correction of the mirror surface curvature, allowing spherical aberration free focus control. Perimeter segmentation greatly reduced required actuation loads allowing improved focal ranges. It was found that the sacrificial layer thickness has a significant impact on the initial curvature of the mirror. Sacrificial layers 0.2 μm thick proved sufficient for release, improved device yield, and resulted in an initially flat mirror.

SILICON NITRIDE DEFORMABLE MIRRORS FOR FOCUS AND SPHERICAL ABERRATION CORRECTION IN MICRO-OPTICAL SYSTEMS

By

Phillip Alexander Himmer

A dissertation submitted in partial fulfillment
of the requirements for the degree

of

Doctor of Philosophy

in

Engineering

MONTANA STATE UNIVERSITY
Bozeman, Montana

November, 2002

APPROVAL

of a dissertation submitted by

Phillip Alexander Himmer

This dissertation has been read by each member of the dissertation committee and has been found to be satisfactory regarding content, English usage, format, citations, bibliographic style, and consistency, and is ready for submission to the College of Graduate Studies.

David Dickensheets — David L. Dickensheets — 11/20/02
Committee Chair — (Signature) — (Date)

Approved for the Department of Electrical & Computer Engineering

Jim Peterson — James Peterson — 11/21/02
Department Head — (Signature) — (Date)

Approved for the College of Graduate Studies

Bruce McLeod — Bruce R. McLeod — 11-25-02
Graduate Dean — (Signature) — (Date)

STATEMENT OF PERMISSION OF USE

In presenting this dissertation in partial fulfillment of the requirements for a doctoral degree at Montana State University, I agree that the Library shall make it available to borrowers under the rules of the Library. I further agree that copying of this dissertation is allowable only for scholarly purposes, consistent with "fair use" as prescribed in the U.S. Copyright Law. Request for extensive copying or reproduction of this dissertation should be referred to Bell & Howell Information and Learning, 300 North Zeeb Road, Ann Arbor, Michigan 48106, to whom I have granted "the exclusive right to reproduce and distribute my dissertation in and from microform along with the non-exclusive right to reproduce and distribute my abstract in any format in whole or in part."

Signature [signature]

Date Nov 22, 2002

ACKNOWLEDGMENTS

David Dickensheets as my advisor is hereby applauded for his bravery and tenacity for assisting me in my pursuit of a doctoral degree. Having the opportunity to began my PhD career at the same time he began his professorial career has been a wonderful opportunity. I have learned much from his scientific insight as an advisor and personal insight as a friend.

I also wish to thank friends and family for their support while I have been working on this project. Many thanks to my family; Karin, Tariq, Peter, Katie, Ali, mom (Nancy) and dad (Jerome). To my friends, whom are also like family, this work would not be possible without your daily support. To Phil, Rand, Gregg, Marilou, and David, thank you for your encouragement, advice and the occasional beer.

To my friend and colleague, Chelle, I wish to thank you for all of the great discussions, in the lab and on the slopes. Colleagues, Micheal, Jeff, Paul and others thanks for your friendship and help along the way.

To Hugo Schmidt, my former advisor and present day committee member, who was there from the beginning, I am glad you were there at the end.

TABLE OF CONTENTS

TABLE OF CONTENTS - CONTINUED

TABLE OF CONTENTS - CONTINUED

LIST OF FIGURES

LIST OF FIGURES – CONTINUED

LIST OF FIGURES – CONTINUED

LIST OF FIGURES – CONTINUED

LIST OF TABLES

ABSTRACT

Laser beam scanning systems benefit from dynamic focus control and aberration correction using a deformable mirror, enabling 3D real-time scanning. Designed for focus and spherical aberration control in optical beam scanning systems, these mirrors are capable of video rate bandwidths allowing real-time 3D imaging in micro-optical scanning systems. Field curvature aberration can also be corrected with the same mirror. Previous work with polysilicon deformable mirrors validated the concept of using specialized deformable optics in beam scanning systems. Fabrication of micro-optics in this dissertation was achieved using a modified surface micromachining technique with silicon nitride replacing polysilicon as the structural material. A bulk anisotropic silicon etch following a PSG release etch allows the creation of a variable cavity depth, overcoming the typical deformation limitations of standard surface micromachining. To perform as desired, parabolic curvature of the mirror surface is required with the ability to introduce positive and negative quartic curvature. Analytical theory showed that deformed simply supported plates have curvature closer to parabolic than deformed clamped plates. Segmentation and thinning of the perimeter was done to in order to emulate this simply supported boundary. Two annular actuation zones were implemented to give independent control over the second and fourth order curvatures. It was found that residual stress present in the silicon nitride structural plate improved the surface curvature and mechanical resonance at the expense of a larger actuation pressure. Mirrors with diameters of 1500, 1000, 750, and 300μm were built and tested. Zonal actuation with annular electrodes proved successful in providing sufficient correction of the mirror surface curvature, allowing spherical aberration free focus control. Perimeter segmentation greatly reduced required actuation loads allowing improved focal ranges. It was found that the sacrificial layer thickness has a significant impact on the initial curvature of the mirror. Sacrificial layers 0.2μm thick proved sufficient for release, improved device yield, and resulted in an initially flat mirror.

CHAPTER 1

INTRODUCTION

Optics that change their surface shape are present in the biological world (e.g., the eye) but only recently has technology progressed sufficiently for mankind to fabricate these shape changing optics. Proposed as a solution to atmospheric turbulence in the early 1950's by Babcock[1], adaptive optics are presently being incorporated into astronomical telescopes. As a low cost alternative to the large scale astronomical adaptive optic systems, micromachined adaptive optics are being developed that are also capable of correcting atmospheric turbulence. Adaptive optics capable of arbitrary wavefront correction require complex feedback control schemes which limit their operational bandwidth from Hz to kHz. Optical aberrations that are not random can be corrected by using deformable mirrors that do not require the ability to arbitrarily deform their surface shape. Laser beam scanning systems that suffer from known aberrations can be corrected with these simpler adaptive optics. This thesis presents work on miniature deformable mirrors specifically made to control focus and spherical aberration operating at "video rate speeds" used in beam scanning systems.

Miniature aberration correction and focusing optical elements are needed for the development of miniaturized optical systems. Elimination of aberration from an imaging system using conventional refractive lens design can require several groups of stacked lenses. For example, modern microscope objective lenses can have up to 14 lens elements for a fully corrected objective lens[2]. This adds complexity, weight, size, and cost to the optical system. Furthermore, complex multielement lenses for millimeter scale applications are a large technical challenge. Changing optical properties of an optical system, such as focus or magnification, requires physically moving lens elements with respect to one another, adding more weight, size, and complexity to the system.

Incorporating a dynamic lens that adjusts focus and corrects spherical aberration into an optical beam scanning system would reduce the number of lens elements in that system. Spherical aberration associated with spherical lenses can potentially be removed and field curvature (image forms on a spherical surface rather than a plane) can be eliminated with dynamic focus control adjustment. Dynamically adjusting the focal length eliminates the mechanical apparatus associated with focusing. This benefits an optical system in terms of weight, size and speed. Physically moving lens elements is relatively slow, while deformable mirrors with 20kHz bandwidths can have 50μsec operating times

Optical wavefront modification

Optical components that can dynamically modify the shape of an optical wavefront are called adaptive optics. By dynamically modifying the phase (optical path length) of the wavefront, time varying wavefront changes can be made in an optical system. The earliest account of adaptive optics being used is in 215 B.C. at Syracuse harbor when Archimedes is reported to have used a "burning glass" to ignite ships of the attacking Roman fleet. It is thought that the burning glass was actually sunlight reflected from an array of metal mirrors[3]. Focus control, as demonstrated by Archimedes, is obtained, as is aberration correction, by modifying the wavefront phase.

The time varying index of refraction of the air due to atmospheric turbulence or, in the case of high power laser beams propagating in air, thermal blooming[4] introduces aberration to a wavefront traveling through the local atmospheric region. Aberrations of this type are random in nature and their correction requires a closed loop feedback system with a wavefront detector and computer control. Other optical systems suffer from predictable, time varying, aberration. This predictive aberration can be corrected using an adaptive optic without feedback. Adaptive optics used with an open loop control scheme (no feedback) are also called active optics. An example of an optical system with predictive time varying aberration is a laser beam scanning system. Off-axis aberration resulting from beam rastering can be corrected with an open loop adaptive optic (active optic) because the aberration is known apriori.

Micromachined deformable mirrors

The bulk of work in adaptive optics has been oriented towards correction of earth based, astronomic and satellite based, terrestrial viewing telescopes. Both of these applications experience random aberration incurred due to light propagating through the atmosphere and require corrective surfaces that can be arbitrarily shaped. Modern optical systems requiring micro-adaptive optics are optical communications applications and high power laser systems. Two common mirror designs for arbitrary wavefront correction are continuous mirrors actuated with an electrode array[5,6,7] and segmented mirror arrays[8,9]. Either of these systems can dynamically correct for spherical aberration and control focus but the complexity of the deformable mirror is a barrier for incorporation into ultra miniature optical systems. Both physical size and interconnect complexity limit use in the smallest systems. Moreover, these mirrors have relatively slow response time. For example, a bandwidth of 75 Hz has been reported for a continuous membrane mirror, capable of arbitrary wavefront correction,[10] which is insufficient for many applications. The infrastructure and operation of these arbitrarily deformable mirror systems is complex, requiring complex feedback systems for the actuator/mirror arrays with interconnections for each actuated element. For specific wavefront variation, focus control for instance, mirrors with only a few actuators requiring few interconnections, may be a more appropriate choice.

Recently, micromachined deformable mirrors have been used in a variety of focus control applications. Free space-fiber coupling[11], fiber-laser diode coupling[12], fiber switching[13], and waveguide switching[14] have all been demonstrated using micromachined deformable mirrors. Besides optical switching, other applications such as barcode scanners, optical read/write heads, and scanned-beam imaging or display systems can profit from a micro-optical focus and aberration control mirror.

Several types of deformable optical elements exist for focus control. Wavefront correction optics have been fabricated using techniques other than micromachining and such optics include refractive focus control lenses using liquid crystal[15], acousto-optic crystals[16], and pneumatic[17] and piezoelectric driven glass plates.[18] Additionally, solid state lead lanthanum-modified zirconate titanate (PLZT)[19] lenses have been built and demonstrated.

Micromachined random wavefront correction optics typically are reflective mirrors that can be comprised of an array of small mirrors, individually controlled, or a continuous mirror controlled with an array or actuators. Actuation mechanisms utilized in micromachining include electrostatic, piezoelectric bimorphs, and thermal actuators, electrostatic actuation being the most widely used. Mirrors developed for specific optical wavefront correction include a piezoelectric and a thermally actuated continuous mirror. The thermally actuated, polysilicon mirrors are circular, 1 mm diameter mirrors with a focal length adjustable from 7.39 mm to 14.36 mm[20]. Focus control using specialized deformable micromachined mirrors has also been demonstrated with piezoelectric actuation of polysilicon.[21] Focus and astigmatism control was concurrently demonstrated using circular and rectangular continuous-membrane polysilicon mirrors with a bandwidth in excess of 20 kHz[22].

Beam scanning systems

One area of interest in the medical field, in-situ imaging of tissue, was a driving motivation for this thesis work[23]. To obtain in-situ 3D images of tissue, miniaturizing of the confocal microscope is necessary and development of a miniaturized focus control system is needed. Other applications include incorporating the mirror into a beam scanning confocal micro-spectrometer allowing 3D focus control without requiring any movable mechanical parts in the system[24]. These micromachined mirrors have speed, and reliability advantages over classical systems because of the simplicity of the devices.

Beam scanning imaging systems suffer from cyclical aberration as the laser beam rasters across the pupil aperture. To reduce off-axis aberration, reducing the aperture of the system thus limiting the field of view is often necessary. This cyclical aberration can be corrected using an adaptive optic in an open loop configuration. The use of a specialized deformable mirror in a beam scanning system will allow the adjustment of focal length, correction of astigmatism and field curvature. The ability to correct spherical aberration can be beneficial by relaxing the objective lens requirements in a beam scanning system. The first reported variable focus mirror for a display was fabricated in 1967 by Alan Traub. [25]. It used a metallized Mylar film stretched over an aluminum frame. Mirrors were made 20-38cm in diameter and the Mylar film was 6-25μm thick. Actuation of the mirror was achieved pneumatically using air pressure generated from a loudspeaker. The mirror was based on a design conceived by Muirhead in 1961.[26]

Proposed research

The primary goal of this project is to design, fabricate and characterize silicon nitride deformable mirrors built specifically for focus control and spherical aberration correction for use in beam scanning systems. For infinite conjugate imaging, a parabolic surface is required for aberration free focus control. Control of spherical aberration is required for maintaining a parabolic shape during focus control and it enables correction of apriori spherical aberration in the optical system. Perimeter modifications and a two zone actuation scheme are incorporated into the design to provide a precise surface shape of the mirrors. Because these variable optical elements are mirrors, chromatic aberrations do not occur.

Thesis organization

This thesis is separated into theory, fabrication, experimental apparatus and results chapters. The chapter on theory discusses the optical requirements and basic geometrical optical theory necessary to guide the mechanical design. The mechanical theory is comprised of analytical and finite element analysis which were used to predict the sensitivity of the mirror surface figure to specific designs. Using results from the mechanical theory section, the fabrication process discussed in chapter 3 is developed. To obtain the surface curvature necessary for focus adjustment in the scanning system, large mirror deflections, on the order of 5 μm, are needed. A modified surface micromachining process is discussed in chapter 3 that allows a tailored cavity depth to be formed in an post- fabrication process. Chapter 4 details the experimental apparatus used in characterizing the surface figure and dynamic behavior of the mirrors. Surface figure is characterized in terms of the quadratic and quartic curvature of the mirror's surface for a given applied pressure. Information on operating voltage requirements can also be obtained from these measurements. Frequency response of the mirrors is used to evaluate their ability to operate at the desired SVGA video rates, as proposed for operation in beam scanning systems. Data obtained from these measurements are presented in chapter 5. Perimeter modifications and process variations are discussed in the context of how they affect the operational characteristics of the deformable mirror. A summary of results regarding the effects of various design parameters is given in chapter 6.

Mirror performance summary

The proposed deformable mirrors were designed, fabricated, and have been tested. It was found that these mirrors are capable of fulfilling the requirements necessary for operation in a beam scanning system. Focus control with zero spherical aberration has been demonstrated and results show that focal lengths as small as 1.3 cm are possible using the deformable mirrors based on current fabrication design. The two-zone actuation scheme allowed spherical aberration due to non-uniform pressure gradients to be corrected, giving spherical aberration free focus control. Operation bandwidth exceeded the SVGA requirements except for the largest 1500 μm diameter mirrors that were hampered by weakened support. The modified surface micromachining process allowed tailored cavity depths and resulted in the ability to use thin sacrificial layers in the fabrication process. Consequentially, released mirrors were flat within the error of our measurement apparatus. The use of thin sacrificial layers also resulted in a greatly improved device yield. Residual stress in the structural layer played a pivotal role, influencing the surface curvature, frequency response, and actuation properties of the mirror.

CHAPTER 2

DESIGN OF DEFORMABLE MIRRORS

Chapter Overview

This chapter covers the design of deformable mirrors for focus control and aberration correction in laser beam scanning systems. The goal is to produce membranes that will form conical surfaces for use as on-axis, variable focus and aberration correction mirrors. Device analysis compares these ideal conic shapes to surface figures obtained by deforming a micro-optical electromechanical (MOEM) structure which is modeled as a mechanical plate. Analytical plate theory and finite element analysis (FEA) are used to examine geometric and structural influences on surface figure and resonant behavior of these deformable plates. Conclusions drawn from these studies are used to arrive at device designs.

The intended goal of this research effort is the development of deformable mirrors that can focus and/or correct an optical beam at video rates. Super video graphic array (SVGA) video rate operational speed in scanned-beam systems requires horizontal scan frequencies on the order of 20 kHz. This leads to periodic variation of off-axis aberrations such as curvature of field at twice the scan frequency. The consequence is corrective optical elements require bandwidths in excess of 40kHz. Focus length adjustment from a few millimeters to infinity while maintaining less than $\lambda/10$ aberration over the full focal range is the operational goal of the focus control devices.

Optical Design

In this section, an idealized optical surface is derived for infinite conjugate focusing of laser beams. Conical surfaces (paraboloids) are distinguished by the property that light incident from one focus is focused to the second focal point. For a paraboloid, one focus is finite while the other is located at infinity. Paraboloids, therefore, have the property that an on-axis infinite object (light parallel to the optic axis) is focused at the other finite focal point without introducing aberration into the beam. This attribute makes paraboloids especially useful as optic devices in laser system applications.

Aberration theory

The design of any optical component requires understanding what aberrations may be added to the wavefront by the addition of the component into an optical system and how such aberration can be minimized via component and/or system design. Optical aberration is defined to be the optical path length difference between the converging wavefront and a spherical wavefront that functions as the reference surface for the calculation of aberration. For numerical purposes, the path length difference between the reference wavefront and the image wavefront is calculated at the exit pupil of the optical system. An exit pupil is the limiting aperture defined by the marginal rays exiting an optical system. Approximations made in the geometrical ray calculations for axially-symmetric geometries give rise to 1^{st}, 3^{rd}, 5^{th}, etc. order degrees of accuracy for the optical path lengths. The 1^{st} order gives rise to linear imaging. The 3^{rd} order approximations are called the primary (Siedel) aberrations.

For an axially-symmetric optical system optical aberration can be separated into five components. The five primary aberrations can be defined as given in equation 2-1 where w(x,y) is the total aberration.[22] The coordinate systems used in this equation are shown in figure 2-1.

$$w(x,y) = a_s r^4 + a_c r^2 (xx' + yy') + a_a (xx' + yy')^2 + a_d r^2 r'^2 + a_t (xx' + yy') r'^2 \qquad (2\text{-}1)$$

The five aberrations, (a_s, a_c, a_a, a_d, a_t) in the order presented in equation 2-1, are spherical, coma, astigmatism, field curvature (a.k.a. defocus) and distortion. Of these five aberrations, spherical aberration and field curvature can be corrected using the deformable mirrors discussed in this thesis. These mirror surfaces need only deform with variable second and fourth order curvature.

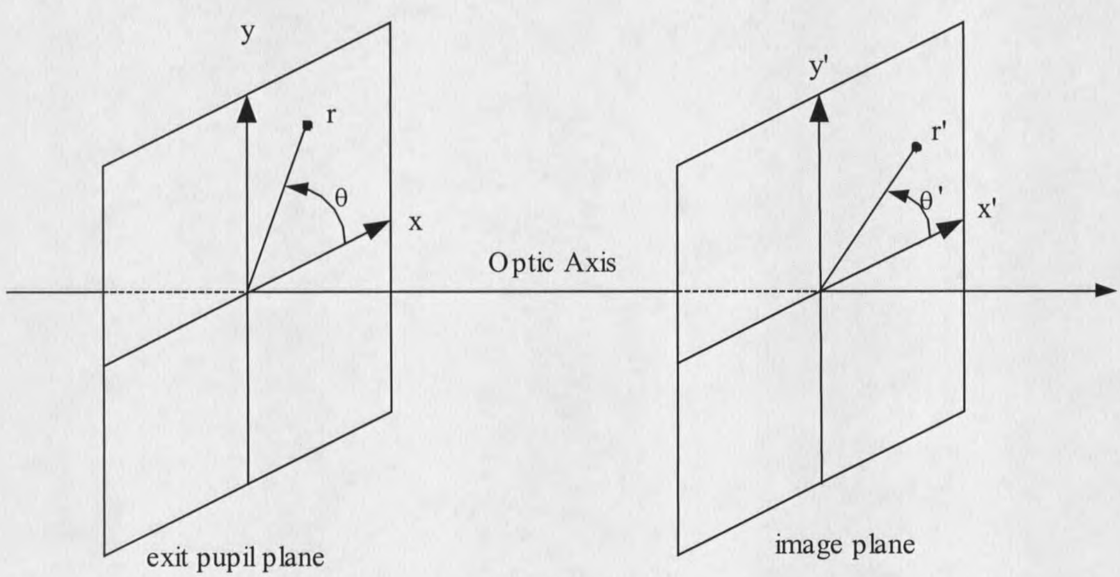

Figure 2-1. Coordinate system used in equation 2-1.

Except for spherical aberration, the aberrations are dependent upon both the pupil and image plane coordinates. Therefore, light originating at the same pupil plane location, focused at different spatial locations in the image plane, has a different wavefront aberration so simultaneously correcting aberration over a full field of view is not possible with a single deformable mirror. A laser beam scanning system probes the image plane one spot at a time, making dynamic correction of aberration with a deformable mirror possible.

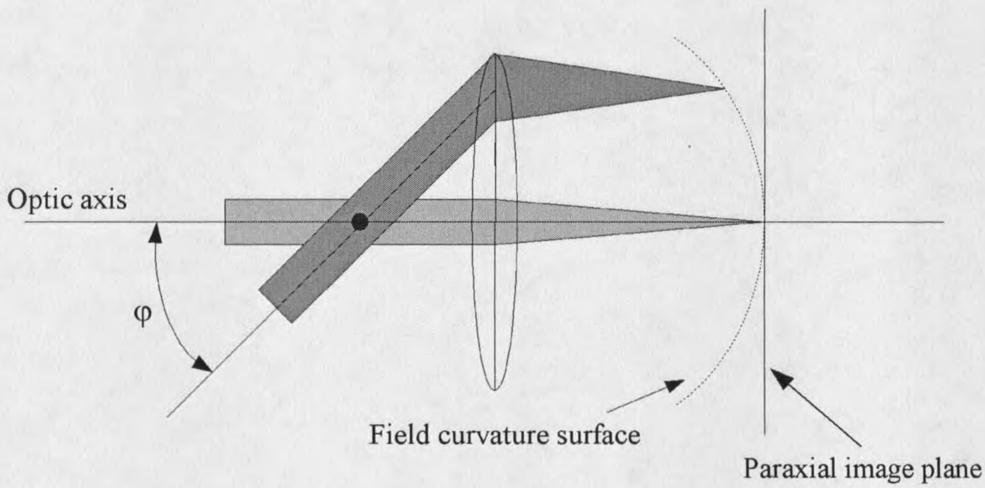

Figure 2-2. Field curvature aberration. The effect of field curvature due to positive(convex) lens is to image a planar object onto a spherical surface. The field curvature (Petzval) image plane intersects the paraxial image plane at the optic axis.

<u>Field curvature</u> Curvature of the image plane in an optical system is known as field curvature, or Petzval curvature, and is illustrated in figure 2-2. This aberration, given by $a_d r^2 r'^2$, depends upon the location of the beam in the exit pupil plane as well as within the image plane, hence dynamic correction is required in a beam scanning system. For the object shown (an off-axis collimated beam) in figure 2-2, correction of the aberration can be achieved by using the proposed deformable mirror. As the beam is swept off the

optic axis and through the angle φ, defocus of the mirror can move the beam's focus spot back onto the paraxial image plane.

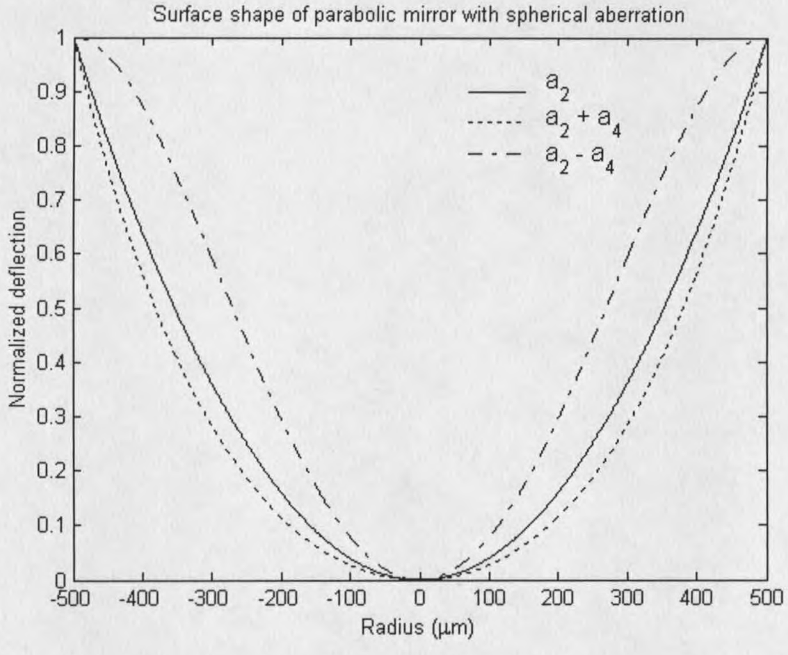

Figure 2-3. Calculated surface figures for a parabolic mirror with positive, negative and zero spherical aberration

<u>Spherical Aberration</u> Spherical aberration is only dependent on the location of the incident optical beam within the pupil plane so an axially symmetric deformable mirror with static fourth order curvature can be used to correct this aberration. The term $a_s r^4$ gives the maximum spherical aberration of the aberrated wavefront. Figure 2-3 illustrates the surface shape of a parabolic mirror having positive, negative, and zero spherical aberration. The effect of spherical aberration, shown in figure 2-4, on the image is to blur the image spot by focusing marginal rays closer to the exit pupil plane for a convex lens. A concave lens causes the marginal rays to focus further from the lens.

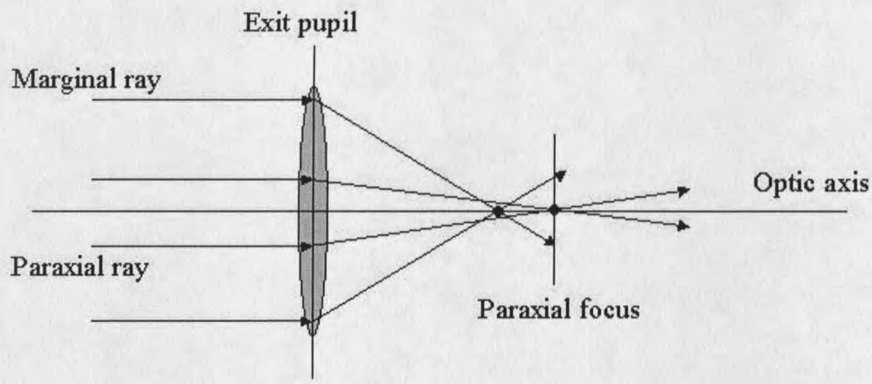

Figure 2-4. Illustration of longitudinal shift in focus caused by spherical aberration of lens. Meridian rays come to focus closer to the lens than paraxial rays for a positive lens.

On-axis imaging

A deformed circular plate that deforms with parabololic curvature can be used as focus control mirror in a laser beam scanning system. A parabolic mirror acts as an infinite conjugate optic. That is, an infinite object is focused to a point on the optical axis. This object point, as per definition, is the focal point of the parabola.

The parabola shown in figure 2-5 is given by equation 2-2.

$$z = ax^2 \tag{2-2}$$

The quadratic coefficient, a, is related to the focal length, f, of the paraboloid by the relation $a = \frac{1}{4f}$. On-axis infinite objects are imaged without aberration by a parabolic

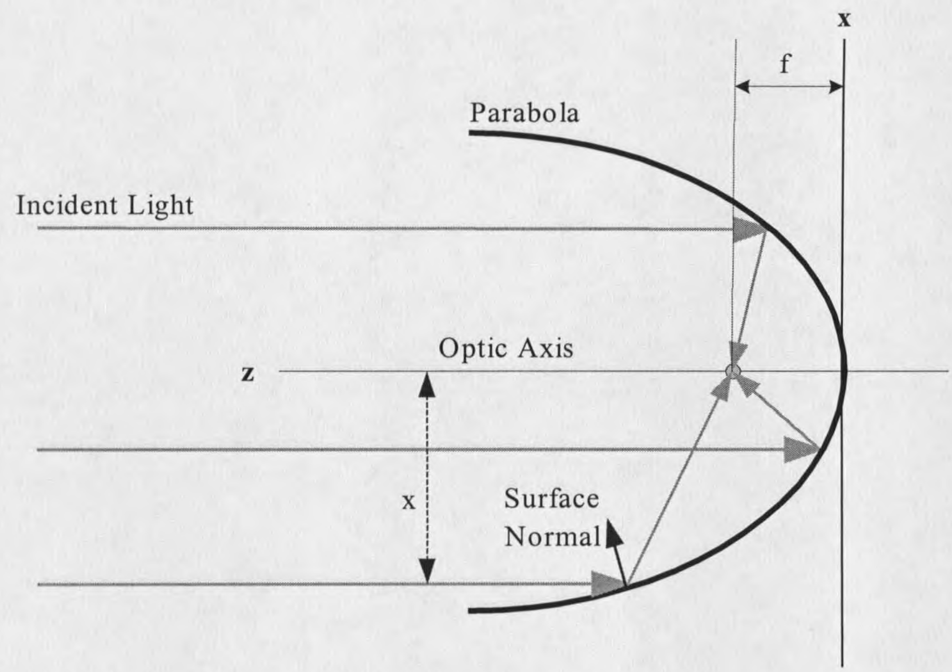

Figure 2-5. Infinite conjugate focusing using a parabolic mirror.

mirror. A non-axial infinite object imaged by a parabolic mirror will suffer from only coma and astigmatism, provided the exit pupil is located at the mirror. The aberration due to a non-axial object is given in equation 2-3 and is the same as for a spherical mirror with the exit pupil at the mirror[27]. The first term in equation 2-3 gives coma and the second term astigmatism of the reflected beam. In equation 2-3 the angle the incident beam makes with the optic axis is ϕ, the location in the exit pupil where the aberration is calculated is given by the polar coordinate (r,θ), as defined in figure 2-1, and f is the focal length of the mirror.

$$w(\varphi, r, \theta) = \frac{1}{4f^2}\varphi r^3 \cos(\theta) - \frac{1}{2f}\varphi^2 r^2 \cos^2(\theta) \qquad (2\text{-}3)$$

Aberration caused by an off-axis infinite object requires that the deformable mirrors discussed in this thesis must be used in an on-axis arrangement or at very shallow angles to prevent degradation of the imaging quality. For non-infinite objects parabolic mirrors can suffer from all aberration types.

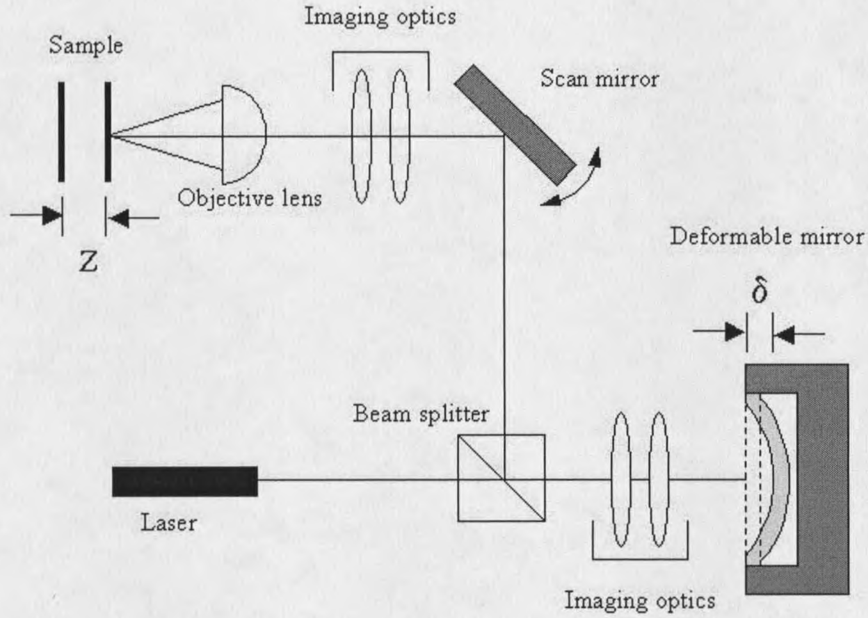

Figure 2-6. Optical layout incorporating a deformable mirror for focus and aberration correction.

For the infinite conjugate beam scanning optical system, illustrated in figure 2-6, the laser beam is scanned over a 2-D area via a scan mirror placed in the back focal plane of the objective lens. To incorporate a deformable mirror into the system for focus and aberration correction, a beamsplitter with additional imaging optics is used to image the deformable mirror onto the scan mirror. The range of focus adjustment made possible with the deformable mirror can be estimated using equation 2-4. The change in focus is given by z, the center deflection of the deformable mirror is w, and the numerical aperture of the system is NA.

$$z = \frac{4w}{(NA)^2} \tag{2-4}$$

This relation is only strictly valid for the optical arrangement illustrated in figure 2-6 where the deformable mirror is imaged onto the optical system's objective lens and the incident beam is collimated.

Analytical Mechanical Design

From the optical design section it was shown that a mirror surface that has quadratic curvature will provide focus control and correct field curvature. Similarly, a mirror with quartic curvature can correct spherical aberration. To construct mirrors that deform with the desired curvature, the influence of mechanical plate parameters on surface figure and resonance are studied. Mechanical plate parameters depend on both geometry and material properties. Geometric parameters are easily altered in the design phase while material properties are, for the most part, fixed by the selection of material and deposition process used for the mirror plate.

Table 2-1 lists the geometric parameters examined for their effect on quartic and quadratic mirror curvature. The boundary geometric shapes were chosen to be circular, based on the symmetry of the desired structure. Clamped mechanical plates deform with quadratic, quartic and higher, even-order curvatures resulting from the physical requirement of a clamped perimeter. A simply supported boundary, as will be shown subsequently, bends with less quartic curvature than a plate with a clamped perimeter, so it is desirable to weaken the perimeter of the plate. To emulate a simply supported boundary, the mirror boundary is weakened via segmentation and thinning of the perimeter. The load distribution also affects the plate curvature. It will be shown in the finite element section that applying a separate load between outer and inner zones on the plate permits control over the quadratic and quartic surface curvature.

Table 2- 1 Mechanical plate parameters

Geometric parameters
Geometry
Perimeter segmentation
Perimeter thickness
Plate thickness
Load distribution

Plate Theory

Mechanical plates with circular boundaries have analytical solutions for their surface curvature and frequency response. In addition, approximate analytic solutions exist for surface curvature that account for an initial in-plane tension in the plate.

Surface Figure Following the work of Sheplak and Dugundji[28], and using their notation, the surface figure of circular plates with in-plane tension is governed by the differential equation 2-5. Sheplak and Dugundji solved equation 2-5 for just the clamped boundary. The simply supported boundary is also of interest here because, as will be shown later, a plate with simply supported boundary conditions has curvature with less spherical aberration than a clamped plate.

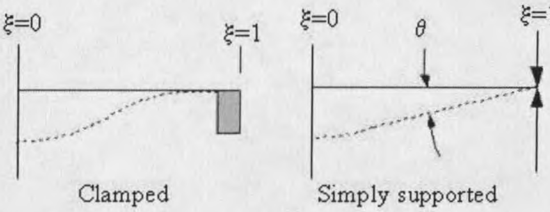

Figure 2-7. Graphical illustrations of the two boundary conditions considered in this work. For clamped boundary at $\xi = 0$ $\theta = 0$ and at $\xi = 1$ $\theta = 0$. For simply supported boundary conditions at $\xi = 0$ $\theta = 0$ and at $\xi = 1$ $M_r = 0$

Analytical solutions of equation 2-5 for simply supported and clamped boundary conditions are possible assuming a small deflection. Clamped and simply supported boundary conditions are illustrated in figure 2-7 where ξ , the dimensionless radial distance, varies from 0 at the center of the plate to 1 at the perimeter. For a simply supported boundary the radial bending moment (M_r), is set to zero. Equation 2-5 is expressed using the parameters preceding equation 2-5. Theta, θ, is the angle the plate makes with respect to the undeformed plate. The variable κ contains an initial tension that arises from the in-plane tension that exists in the plates due to fabrication processes. The origin of the initial in-plane tension will be elaborated upon in chapter 3.

Equation 2-5 is written in terms of the unitless parameters defined below

$$\xi = \frac{r}{a} \quad \theta = \frac{dW}{d\xi} \quad W = \frac{w}{h} \quad P = \frac{p_o a^4}{Eh^4} \; D = \frac{Eh^3}{12(1-\upsilon^2)} \; \kappa = \sqrt{\frac{N_o a^2}{D}}$$

The circular plate geometry is defined by a radius **a** and thickness **h**. The material parameters are Young's modulus E, Poisson's ratio ν, and the stress, T which appears as the tension term N_o. The in-plane tension $N_o=T*h$ is defined as the stress, T, multiplied by the plate thickness, h.

$$\theta'' + \frac{\theta'}{\xi} - \left(\kappa^2 + \frac{1}{\xi^2}\right)\theta - 12\left(1-\upsilon^2\right)S_r\theta = 6\left(1-\upsilon^2\right)P\xi \qquad (2\text{-}5)$$

Equation 2-5 can be solved for θ in terms of Modified Bessel functions, then integrated to give the deflection W in terms of the normalized radial distance ξ.

Table 2- 2 Parameter definitions for equation 2-5

w = vertical deflection	E = Young's Modulus
h = plate thickness	υ = Possion's Ratio
a = radius	P_o = Uniform pressure
r = radial distance	N_o = Initial tension

A uniformly loaded circular plate can be deformed until the center deflection becomes near the plate thickness. Theoretically at this point stress in the plate which resists the load, contained in the term S_r cannot be neglected. However, it is noted by Sheplak and Dugundji, that approximate solutions work very well at larger deflections for plates with a large in-plane tension. For a clamped boundary and a uniform load, the solution to equation 2-5 is given by equation 2-6 in terms of the modified Bessel function $I_v(\kappa\xi)$.

$$W(\xi) = 3(1-\upsilon^2)p\left[\frac{2(I_o(\kappa\xi) - I_o(\kappa))}{\kappa^3 I_1(\kappa)} + \frac{1-\xi^2}{\kappa^2}\right] \qquad (2\text{-}6)$$

For a simply supported boundary the solution to equation 2-5 is

$$W(\xi) = 3(1-\upsilon^2)p\left[\frac{2(1+\upsilon)}{\kappa^3}\frac{(I_o(\kappa\xi) - I_o(\kappa))}{(\kappa I_0(\kappa) + (\upsilon - 1)I_1(\kappa))} + \frac{1-\xi^2}{\kappa^2}\right] \qquad (2\text{-}7)$$

Using equations 2-6 and 2-7 the surface curvatures of deformed plates are plotted in figure 2-8 with no initial tension ($\kappa = 0$). For comparison, a plate with quadratic curvature is also plotted. The clamped plate has significant discrepancy from the desired quadratic curvature while the simply supported plate's curvature is much closer to quadratic.

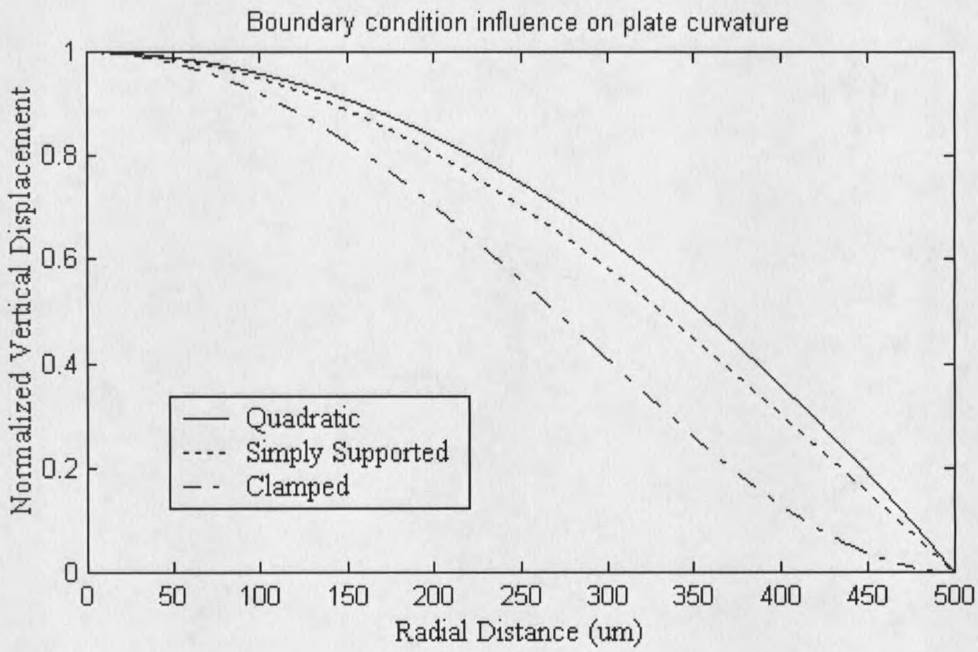

Figure 2-8. The normalized curvature of a 1 mm diameter mechanical plate is shown for simply supported and clamped edge conditions along with a parabolic curve. The mirror center is located at 0 μm and the clamped perimeter is located on the graph at the radial distance of 500 μm

The influence of the in-plane tension on the surface curvature is studied using equations 2-6 and 2-7. Figures 2-9 and 2-10 illustrates how an increasing residual stress forces both the clamped and simply supported plate to deform with less quartic curvature, ultimately deforming with only quadratic curvature. Discussed further in chapter 3, the

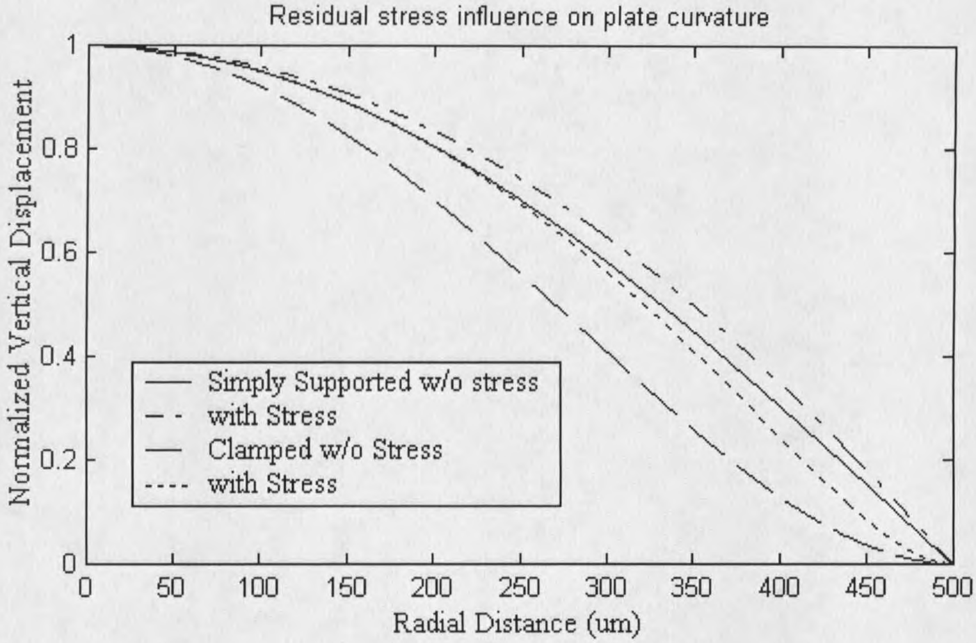

Figure 2-9. Clamped and simply supported plate curvatures of a 1 mm diameter plate are shown with and without an initial tension (residual stress) of 5 Mpa. The mirror center is located at 0 μm and the clamped perimeter is located on the graph at the radial distance of 500 μm

in-plane tension is process dependent, and may not be a parameter available to the designer for modification.

The mirror perimeter design was chosen so that the mirror's boundary emulates a simply supported condition. The two techniques used for creating a simply supported mirror perimeter are segmenting and thinning the perimeter. To investigate the effectiveness of these perimeter modifications finite element analysis is used. This analysis is discussed in the Finite Element Analysis section.

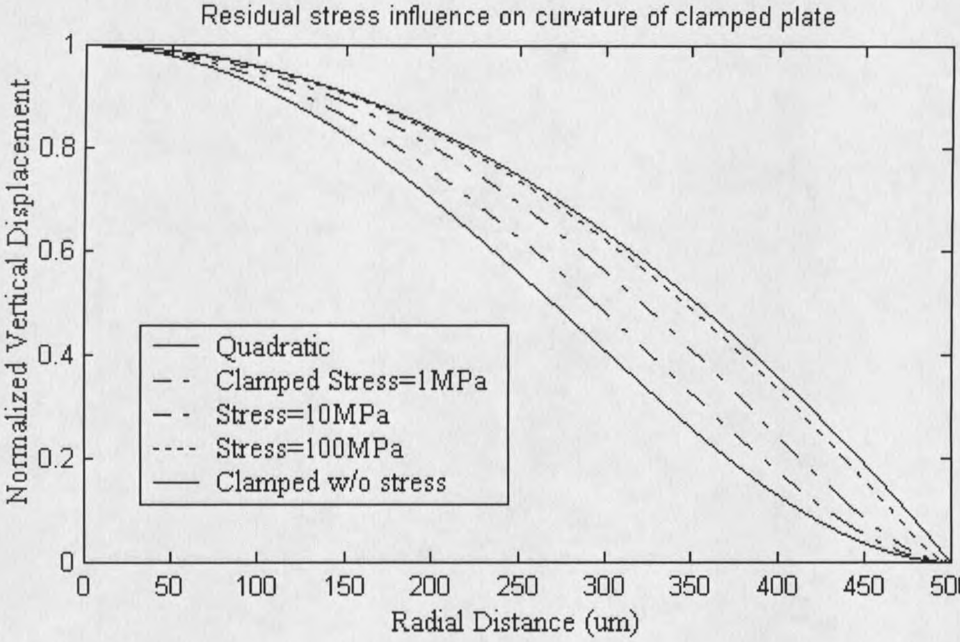

Figure 2-10. Effect of residual stress on a clamped 1 mm diameter mechanical plate The mirror center is located at 0 μm and the clamped perimeter is located on the graph at the radial distance of 500 μm.

Finite element analysis

Geometric variations that do not have analytic solutions can be studied using finite element analysis. From the mechanical theory section it was determined that simply supported plates have less spherical aberration than clamped plates. To emulate the simply supported boundary condition, thinning and segmentation of the plate perimeter was considered. To test the sensitivity of the surface curvature on these perimeter modifications finite element analysis (FEA) was used. In addition, FEA was used to model the effects of multiple actuation zones on surface curvature. Analytical analysis assumed a homogeneous, uniform load across the surface of the plate.

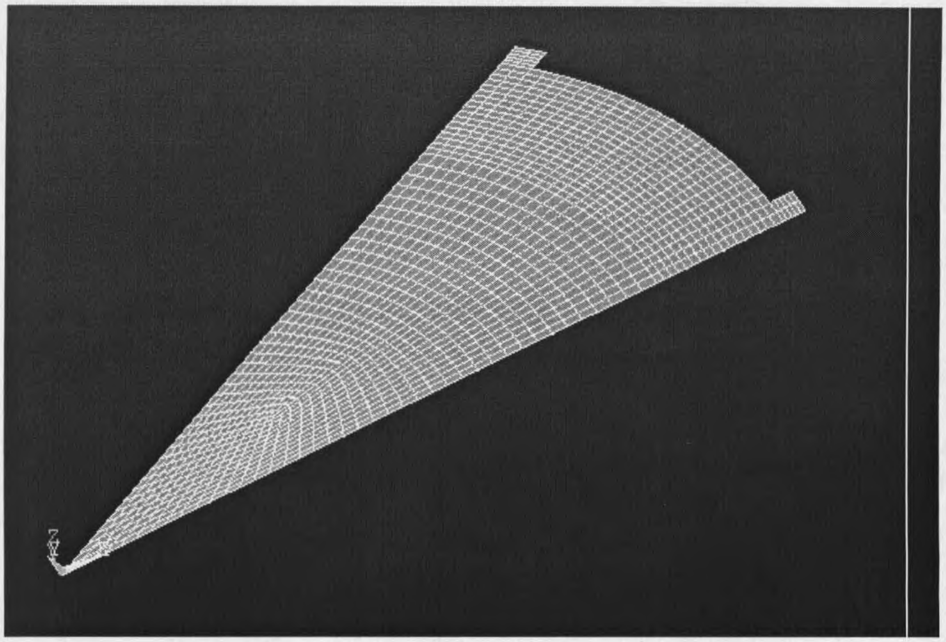

Figure 2-11. A mesh plot of the FEA model with 10% segmentation along the perimeter.

The FEA model used in this study is a 2-D geometric model using shell elements. The FEA model consist of two layers: a geometric model and a mesh model. The geometric model contains keypoints(specified points in space), and lines and is used to generate the mesh model. The mesh model contains nodes and elements that are combined together to form a lattice which is shown in figure 2-11. The smaller mesh elements along the perimeter are necessary for modeling a thinned perimeter.

In finite element analysis meshing discretizes the geometry of the object to be modeled. The meshed model shown takes advantage of the axial symmetry of the circular geometry which is limited by the segmentation of the perimeter. Using the appropriate boundary conditions along the edge the 15^{o} wedge shown represents the entire plate, simplifying the model building and saving computational time. For 10%

segmentation and 20 hinges, each support tab is 1.5 ° so in figure 2-11 the support strips are each 0.75 ° representing ½ the support strip on each side of the model.

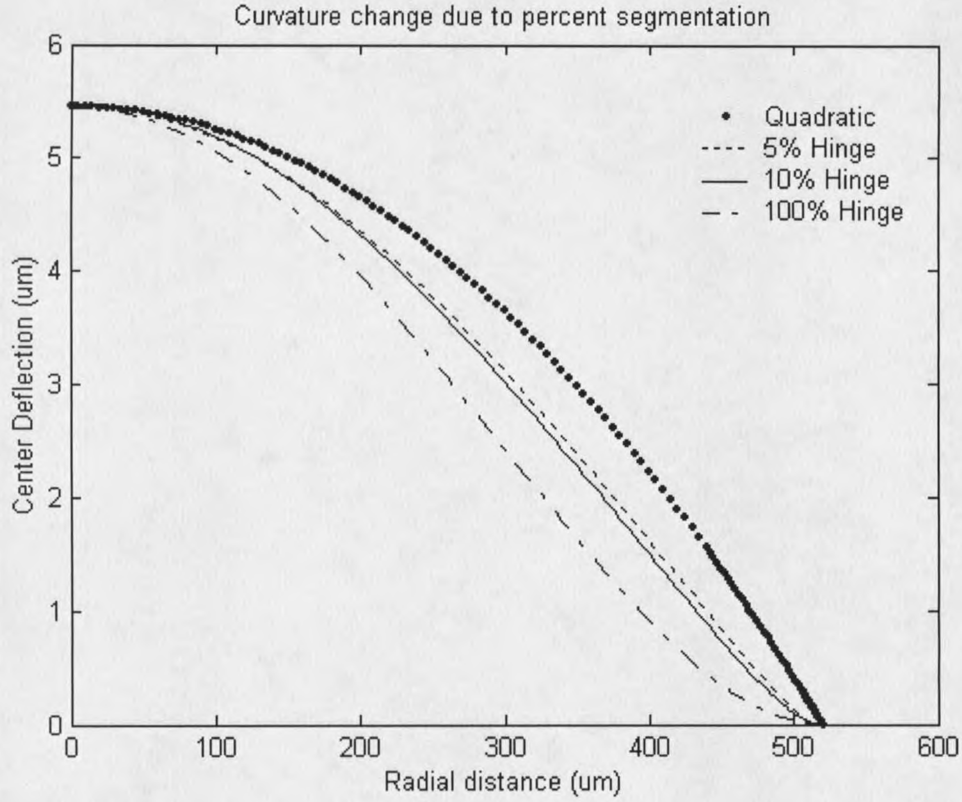

Figure 2-12. Variation of plate curvature with perimeter support. A non-segmented perimeter with 100% support.

Using a simplified FEA model that ignored residual stress, a parameter study was made that examined the sensitivity of plate curvature to perimeter thinning, segmentation, and actuation zones. In figure 2-12 segmenting the perimeter is seen to improve the parabolic nature of the surface curvature. In addition, a segmented perimeter reduces the applied load necessary to achieve the same deflection as a fully supported perimeter. The degree of improvement is seen to diminish rapidly so 10% support was chosen as adequate.

Zonal actuation was incorporated as an additional design parameter to allow active control of the surface curvature. It is seen in figure 2-13 that variation of the pressure load from the inner to outer zone shifted the curvature from negative spherical aberration to positive aberration for approximately a 90% aperture.

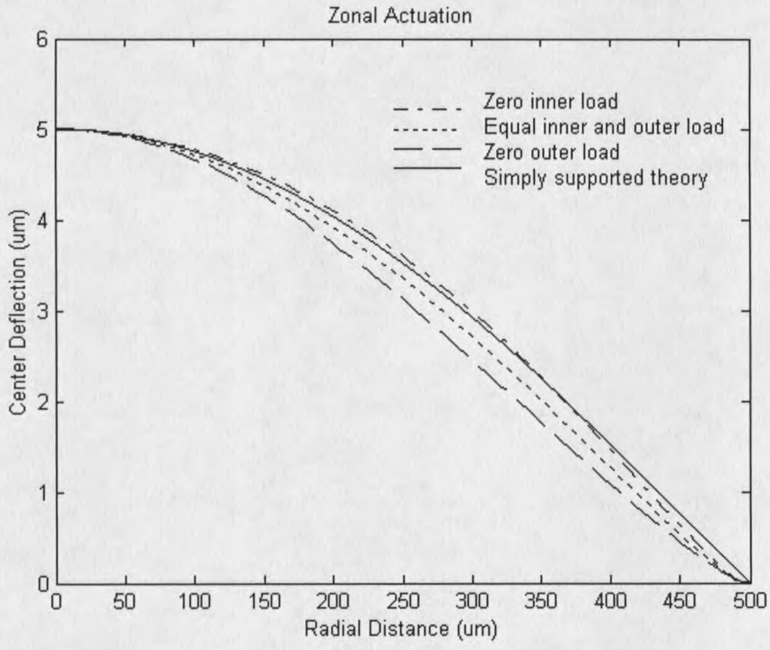

Figure 2-13. Zonal actuation of a clamped circular plate.

FEA analysis suggest that 10% segmentation will improve the surface curvature but by itself is not sufficient to eliminate aberration. The use of two actuation zones demonstrated that active control of the surface figure is possible enabling the spherical aberration to be varied from positive to negative. Since this FEA analysis did not account for in-plane tension, the results are used as a test of the parameter's sensitivity rather than giving quantitative results.

Actuation/Electrical

By means of an electrostatic force, a load can be applied to the plate. A differential voltage applied to the plate and an underlying electrode gives rise to an attractive electrostatic force. The attractive electrostatic force is balanced by the mechanical spring constant of the bending plate. A simplified model of the actuation is shown in figure 2-14 where a parallel plate geometry is assumed for simplicity of theory and the mechanical restoring force is depicted as a simple spring.

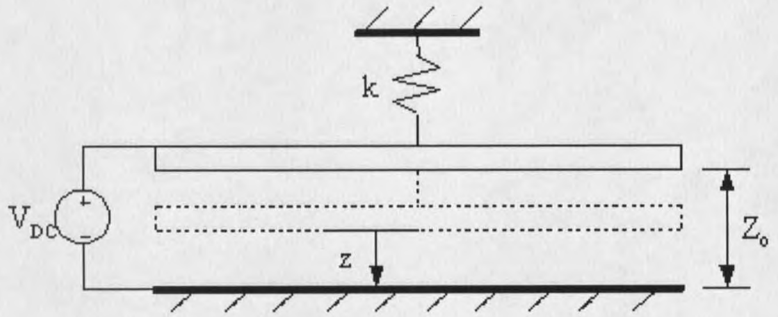

Figure 2-14. Parallel plate electrostatic deformation.

From electrostatic theory the force between two conductive plates is given as

$$F = \frac{\varepsilon_o A V^2}{2z^2} \tag{2-8}$$

The distance z is as defined in figure 2-14, ϵ_o is the electrical permitivity of air (8.854e-12), A is the area of the plate, and V is the applied voltage between the plates. As seen in equation 2-8 the force between the plates is always attractive and is inversely proportional to the square of the distance between the plates.

A result of the balance between the linear mechanical restoring force, approximated as a linear spring, and the non-linear electrostatic attractive force is a phenomenon called "snap down". By equating equation 2-8 with the mechanical restoring force, $k(Z_o - z)$, and setting the derivative $\frac{dV}{dz} = 0$ it can be shown that when the plate is deflected beyond 1/3 of the gap distance, Z_o, the electrostatic attractive force overwhelms the mechanical restoring force causing the deformable plates to "snap" down in contact with the fixed electrode. For a 5μm effective range of motion, a 15μm gap between the surfaces becomes necessary.

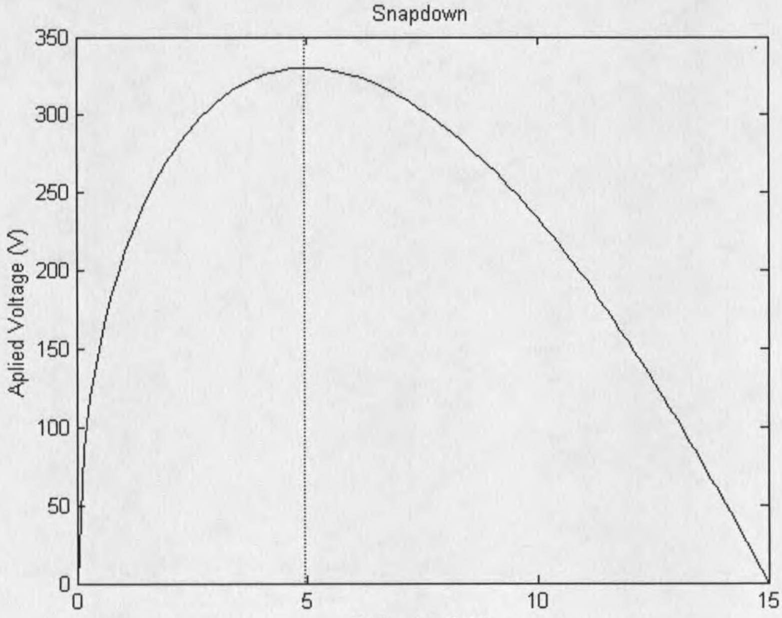

Figure 2-15. Pressure from an electrostatic force applied between two infinite conductors. The dotted line is the maximum distance the plate can be deflected before snapdown occurs.

In figure 2-15 the horozontial axis is the distance the plates travels (Z_o-z) and the vertical axis is the applied voltage. The data shown in figure 2-15 is for a 1000μm diameter mirror with clamped boundary conditions giving a spring constant of 820N/m calculated using equation 2-6. The dotted line represents the maximum deflection of the plate before the electrostatic force overcomes the mechanical restoring force.

CHAPTER 3

DEVICE FABRICATION

Chapter Overview

Beginning with an overview of micromachining technology, this chapter presents the steps used to fabricate the micro-optical deformable membranes. Implementing the device design with a working process flow requires melding fabrication process issues, material compatibilities and material properties with the desired design. Guided by the design parameters developed in the previous chapter and fabrication criteria to be discussed in the beginning of this chapter, an operational device was constructed at Stanford University's Center for Integrated Systems.

Fabrication facilities

Our devices were fabricated at the Stanforn Nanofabrication Facility (SNF) through participation in the national science foundation's NNUN (National Nanofabrication Users Network) program. The Stanford facility, the Center for Integrated Systems, was selected because of the availability of LPCVD (low pressure chemical vapor deposition) equipment for growing silicon nitride and silicon dioxide thin films and our prior experience with the facility.

Micromachining Overview

Micromachining arose from microelectronic industry, using the same suite of materials to create micron scale mechanical devices instead of transistors. The process of micromaching can be broken down into three general steps: deposition, lithography, and etching which are illustrated in figure 3-1. These three sequential steps constitute a process cycle, each cycle forming a structural layer. The thickness of each layer can range from nanometers to several microns; this limits the vertical size of a structure to microns in height. Hence, the devices formed are quasi-3D while laterally the structure's size is restricted by the diameter of the substrate.

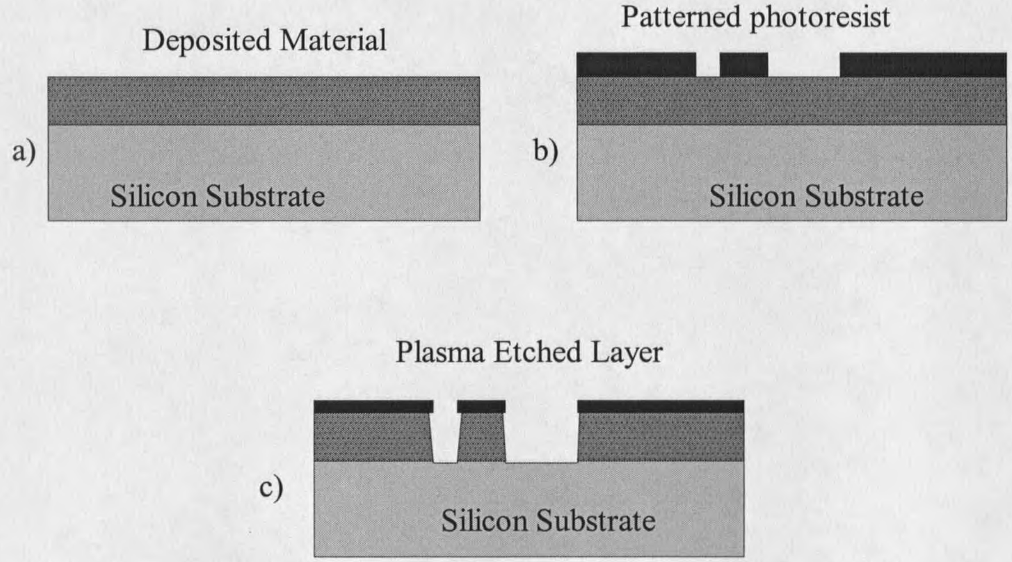

Figure 3-1. Three step micromachining process needed to produce a structural layer

The first step in a process cycle is material deposition. Deposition techniques include low pressure chemical vapor deposition (LPCVD), plasma enhanced chemical vapor deposition (PECVD), thermal oxidation, thermal evaporating, and sputtering.

Most materials can be deposited using several of the techniques mentioned. Which technique is chosen depends upon desired material parameters, deposition conditions, and equipment availability.

To pattern a material layer, an overlying mask layer is needed with the desired pattern in it. Photolithography is used to create the pattern in the mask; a typical mask is photoresist. Photoresist is a light-sensitive polymer that is deposited by spinning a liquid solution onto the wafer and baking to harden the solution. A photolithographic aligner then images the desired pattern onto the photoresist. During development, the exposed regions of photoresist are removed (positive resist) exposing regions of the underlying layer which is depicted in figure 3-1b. The thickness of the photoresist used is dependent on the subsequent etch processing needed and the pattern resolution required. A limitation of the process is that thicker resist coatings yield poorer pattern resolution.

Two common etching technologies used in micromachining are plasma etching and chemical wet etching. Plasmas can etch amorphous or polycrystalline materials anisotropically or isotropically, while most chemical solutions are isotropic etchants. Etching features through a layer require a mask, as previously discussed, and an etch stop to limit the depth of etching. As depicted in figure 3-1c the etch ratio between the etched material and the photoresist must be large enough that the photoresist is not completely etched away. Additionally, a large etch ratio between the etched layer and material beneath is needed to prevent unwanted etching through the underlying layer.

Modified Surface Micromachining Design

To create moveable devices with micromachining fabrication, clearances must exist between moving components. Surface micromachining is a technique where a sacrificial layer of material is deposited beneath the device layer and is later removed leaving the device layer free to move. A typical surface micromachining process flow uses a silicon oxide layer as the sacrificial layer and polysilicon as the device layer. The structural layer of polysilicon has via holes etched through the layer so that a subsequent oxide etch removes the underlying oxide layer leaving an air gap beneath selected areas of the polysilicon. These vias are illustrated in figure 3-2.

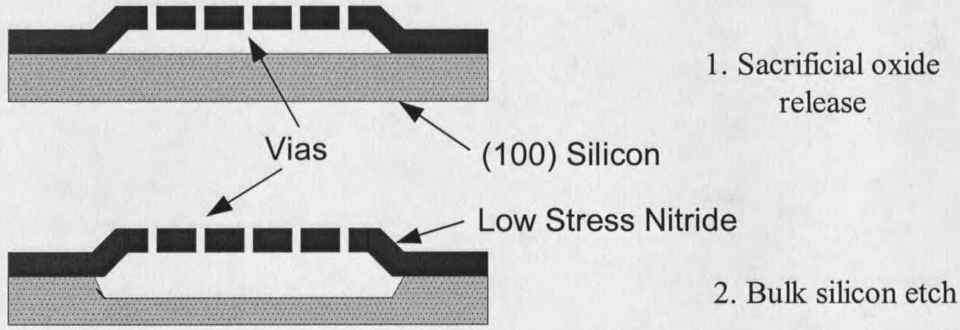

Figure 3-2. A two step release process for creating an variable depth cavity. a)The sacrificial oxide release creates the initial air gap. b) The final air cavity depth is formed by the anisotropic etch of the silicon (100) plane with perimeter undercutting shown

Because of technical and practical problems, sacrificial layers beneath the overlying polysilicon layer are limited to a thickness of a few microns. Realized movement of the mechanical component is then approximately one third of the sacrificial layer thickness due to snapdown (see chapter 2 actuation section) so actuation distances are limited to approximately one micron. Our modified surface micromachining process incorporates a bulk silicon etch after the sacrificial oxide pad etch. By using a structural layer of silicon nitride instead of polysilicon after the sacrificial oxide etch, a bulk silicon etch can be performed. An anisotropic etchant preferentially etches the (100) surface creating a uniform cavity beneath the silicon nitride structural layer. The combination of the sacrificial layer followed by the anisotropic bulk silicon etch is what will be referred to as modified surface micromachining.

Sacrificial Layer

Using the modified surface micromachining technique, the function of the sacrificial layer is then to expose the (100) silicon surface rather than create a clearance gap beneath the mirror. The etch rate of the sacrificial layer is controlled by the material used and the geometry of the device.

Material used for a sacrificial layer must have a large differential etch rate between the sacrificial layer and the structural materials used. Silicon dioxide is a common sacrificial layer material because it can be etched using hydrofluoric acid (HF) which does not etch silicon and only very slowly etches silicon nitride. For the deformable mirror, the sacrificial layer chosen is a variant of silicon dioxide with phosphorus doping known as phosphosilicate glass(PSG). PSG has a faster etch rate than pure silicon dioxide giving it a high differential etch rate for silicon nitride in hydrofluoric acid.

The device geometry controls the etch rate through the sacrificial pad thickness and via placement in the overlying structural layer. The sacrificial pad thickness determines the release etch rate and mirror support profile. Minimizing the thickness of the sacrificial layer is beneficial for structural reasons[29]; therefore, the sacrificial layer is deposited as thin as diffusion of the oxide etchants will allow. Thick sacrificial pads have shorter etch times because diffusion rates of the HF etch solution are higher. The via spacing and size also controls the flow of etchant and etch products into and out of the sacrificial pad etch front.

Anisotropic Etching

Etching crystalline silicon with an anisotropic etchant is known as bulk micromachining. An etchant commonly used for this purpose is tetramethylammonium hydroxide (TMAH). In crystalline silicon, TMAH etches (100) planes approximately 25-50 times faster than (111) planes depending upon temperature and concentration of the TMAH solution[30]. For the purposes of discussion, the (111) etch rate will be considered negligible.

The deformable mirrors are fabricated on p-type (100) wafers. This crystalline orientation was selected because of the anisotropic etch properties of the crystal planes. The (100) surface is preferentially etched so that the exposed (100) surface can be uniformly etched down, creating the desired cavity beneath the device. In figure 3-3 the elliptical opening in the mask covering a (100) silicon wafer will etch as indicated by the dashed lines that form a rectangular polyhedron. The undercut of the elliptical boundary illustrates one complexity that arises from the anisotropic etch: orientation dependent undercutting of mask geometries. Any mask openings not orientated in <110> directions will be undercut to some degree by the selective etch[31].

Because the cavity beneath the mirror is created primarily by the bulk silicon etch, the sacrificial layer thickness can be thinner than would be required if the cavity depth was a function of the sacrificial layer thickness alone. The cavity depth then becomes a variable function of the silicon etch time. To prevent the geometry dependent undercutting illustrated in figure 3, surfactants can be added to the TMAH, decreasing the anisotropy of the etch and leading to a uniform undercut of the perimeter. This also reduces the uniformity of the etched (100) surface. The effect of the surfactant is discussed in detail in the post processing mirror release section of this chapter.

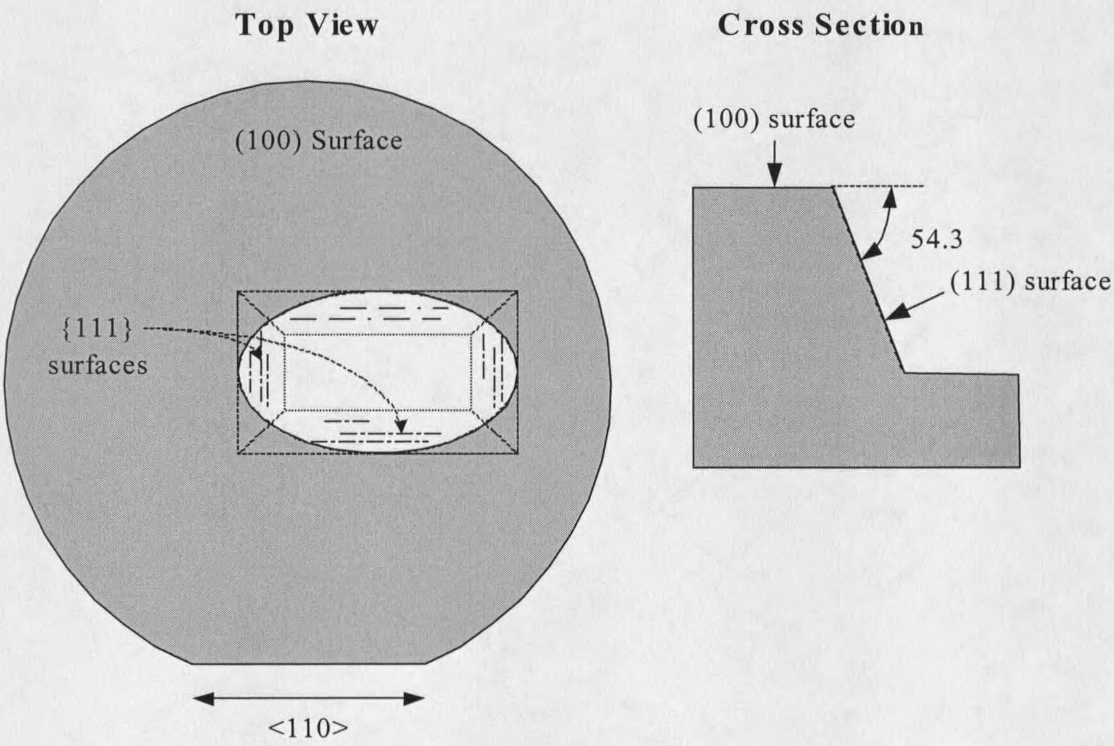

Figure 3-3. Anisotropic etch of a (100) silicon wafer. The top view shows the etch outline due to an elliptical opening in a mask on (100) silicon. The cross section illustrates the angle between the (100) wafer surface and the (111) plane.

Lithography for Micromachining Fabrication

The deformable mirrors were fabricated using an Ultratech 1:1 stepper photolithographic system. Photolithographic masks are quartz plates with a chrome coating. Openings in the chrome form the patterns that are transferred to the photoresist. Using software designed for mask layout, L-Edit, seven masks were created for the deformable mirror processes. A stepper lithography system repeats the mask pattern (die) on the wafer in a user defined array as illustrated in figure 3-4. The die layout blueprint used for this project patterns 62 dies on a 4" wafer. Die by die lithography allow individual process steps to be included/excluded on portions of the wafer. This flexibility permits mirror designs to be tested while eliminating wafer-to-wafer fabrication variation. Alignment between mask levels is accomplished using the Ultratech's automated alignment system.

Masks

Seven mask levels are shown in figures 3-5 and 3-6 for a 1mm circular membrane. An additional mask was used that only etched alignment marks into the wafer. This alignment mask was used as the first step to etch alignment marks into the silicon wafer. Each mask has the device layout as shown in figure 3-4 with each level having the individual features shown in figures 3-5 and 3-6.

Pattern Alignment

Alignment marks are used to align process levels on the wafer. Processing affects the accuracy and usefulness of the alignment marks. Built for IC production, Ultratech alignment targets are required to be either plateau or trench cross patterns 2μm wide, 200μm long and should have no more than a micron of vertical relief. The Ultratech provides two sets of five separate alignment mark positions allowing additional alignment marks to be etched onto the wafer at stages in the process. Because the alignment marks are automatically acquired, failure of the Ultratech lithographic equipment to obtain alignment is catastrophic. The first process level must etch alignment target(s) into the layer allowing subsequent masks to be aligned to previous layer. The subsequent mask may etch additional alignment marks into the wafers as processing allows. Details of how to create the alignment targets can be found at Stanford's SNF web site[32]. The alignment targets undergo the same processing as the wafer and they can become unusable due to processing. The specific alignment scheme for the deformable mirrors will be discussed in the process flow section.

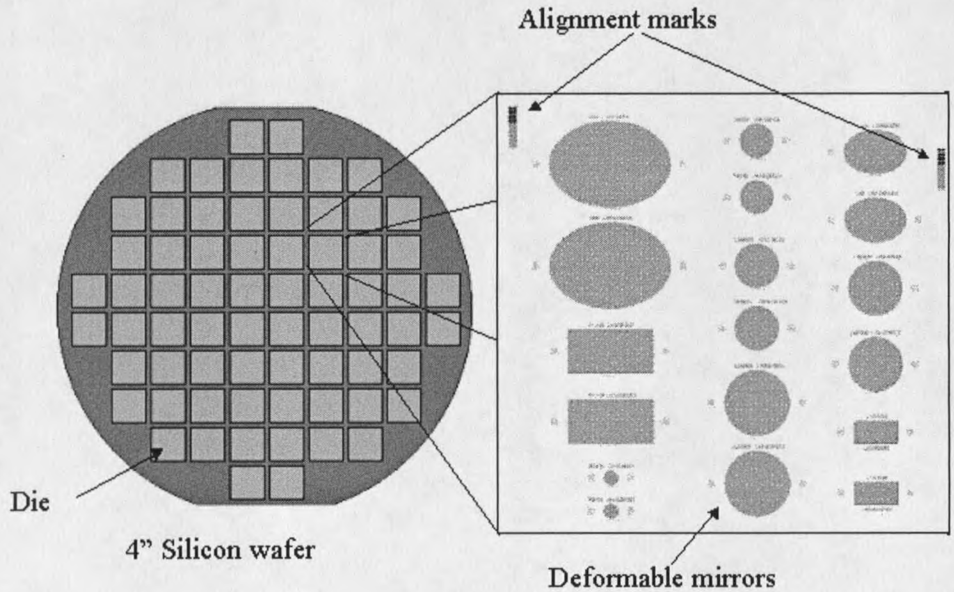

Figure 3-4. Die layout on wafer with exploded view of the device layout on the photolithographic mask.

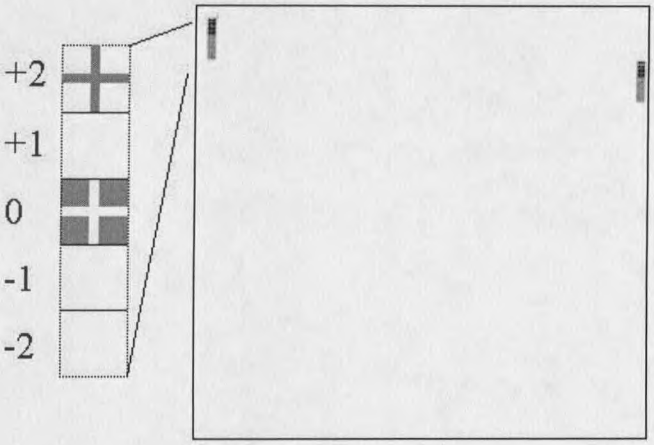

Mask1. Ultratech alignment marks. The center mark is always an open cross. It and the four additional mark positions are shown in the illustration to the left of the mask layout. A closed center cross is illustrated in the +2 mark position

Mask level 2. Electrical isolation thermal oxide.

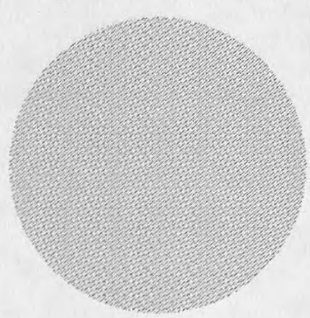

Mask level 3. Sacrificial oxide pad.

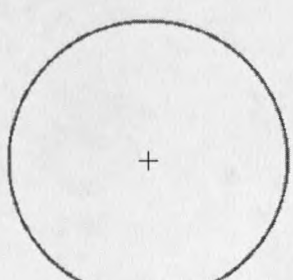

Mask level 4. Thinned perimeter.

Figure 3-5: Patterns used at each mask level for a 1mm circular mirror used in the fabrication of the deformable mirrors. Mask levels are in the order they are used for fabrication. Mask1 is used to etch initial alignment marks into the blank wafer.

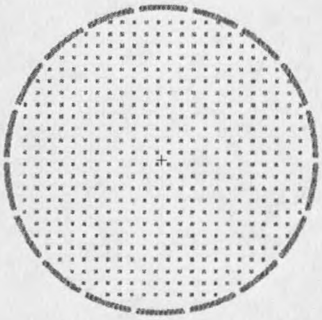

Mask level 5. Segmentation and via nitride plate etch.

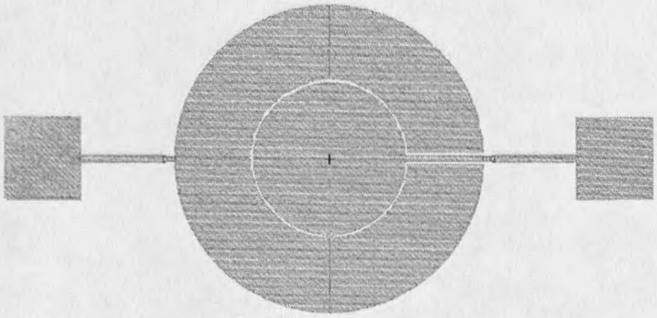

Mask level 6. Metallization pattern.

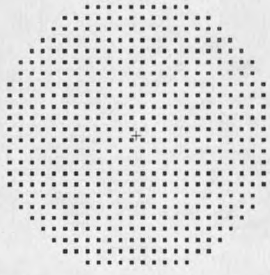

Mask level 7. Metallization vias.

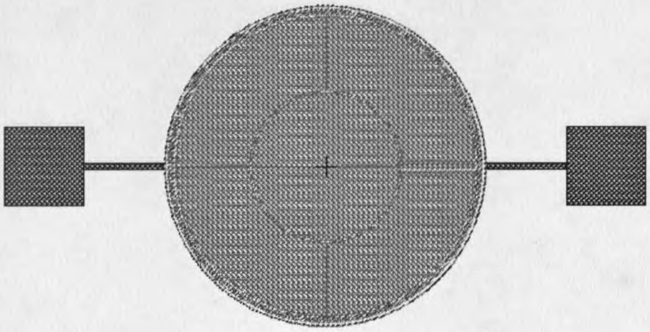

Composite of mask levels 1-7.

Figure 3-6: Masks used in the fabrication of the deformable mirrors. Masks are in the order the are used for fabrication. The composite mask overlays the 7 process masks for the 1mm diameter mirror.

Fabrication Sequence

Implementing the mirror design into a fabrication process requires converting design parameters into fabrication steps. The relevant considerations are

1. Constructing a cavity beneath the mirror for actuation
2. Defining the mirror's perimeter
3. Creating a thinned plate region along the circumference
4. Segmenting the perimeter
5. Creating actuating zones

Secondary considerations are the choice of equipment and the materials needed for the construction of the mirrors. The specifics for designing a fabrication plan depend upon what micromachining technique is used.

Fabrication Method.

The methodology chosen for the fabrication of the deformable mirrors is a combination of surface and bulk micromachining using silicon nitride. Combining surface micromachining with bulk micromachining allows an arbitrary cavity depth to be made after clean room fabrication is completed. Details about this technique are given in the modified surface micromachining section of this chapter. An arbitrary cavity depth gives a flexibility that is important for tailoring the deformable mirrors for specific tasks. The cavity depth determines what voltage is necessary for a particular focal length provided that the cavity depth is sufficient for actuation. (See figure 2-12 in chapter 2 actuation design)

Perimeter Definition

The selected method of perimeter definition uses the sacrificial oxide pad to establish the perimeter of the mirror. Undercutting of the perimeter will occur during the bulk silicon etch because the (111) : (100) etch ratio is not infinite. This ratio varies between 1:10 and 1:100 depending upon the etching solution and temperture. The perimeter variability with etch depth is a potential problem. This method also creates an irregular perimeter outline due to the anisotropic nature of the silicon etch (see figures 3-3 and 3-11). Pad thickness ranging from 0.2μm to 1.0μm were used for the deformable mirror devices.

Mirror membrane

Control of the deformable mirror's surface figure is achieved, in part, by the boundary conditions of the mechanical plate and the tensile stress of the plate. Although it is impossible to implement a simple supported boundary condition, an approximation to this boundary condition was attempted by segmenting and thinning the plate's perimeter. FEA analysis suggested that such perimeter weakening approximated a simple boundary.

Fabricating a thinned perimeter required the use of two separate processing cycles. Shown in the fabrication sequence in figure 3-7 steps 3 and 4, the two step nitride deposition process is necessary because there is no reliable method to etch into nitride to a specified depth without an etch stop. After the first deposition, a ring of nitride can be etched using the PSG sacrificial layer as the etch stop. A subsequent second conformal nitride layer becomes the thinned support and adds to the final nitride mirror thickness.

The mirror plate is made of low stress silicon nitride. This nitride is a non-stoichiometric, silica rich ratio of silicon to nitrogen which is designed to have a minimum residual stress. Sources of stress in LPCVD silicon nitride are related to the deposition mechanism. In LPCVD nitride the residual stress is thought to be due to bond lengthening and cavity formation that occurs as the LPCVD nitride is grown[33]. Silicon nitride can be deposited using either plasma enhanced chemical vapor deposition (PECVD) or low pressure chemical vapor deposition (LPCVD). PECVD nitride can be deposited with a lower residual stress and the stress can be tailored to a desired value.[34] However, reputed material repeatability for the available PECVD equipment is poor. Nitride mirrors in this study are made using the LPCVD low stress nitride because of equipment availability and the problematic PECVD nitride quality and consistency at the fabrication facility.

Residual stress in LPCVD nitride films can be as low as 10 MPa. Measurements made using Guckel rings and pointers fabricated in the same processing run as the deformable mirrors gave residual stresses of 100 Mpa. In theory, the tensile stress in the plate can be tailored with the fabrication process[35] but in our studies this parameter remained fixed.

The vias are 5x5 μm in size and are spaced 30 μm apart over the extent of the sacrificial pad. Optically, the vias are detrimental so via spacing is made as large as possible while still allowing mirror release without significant etching of the structural layer.

Metallization

To actuate the deformable mirror, a voltage will be applied between two conductive surfaces. The top surface will be the reflective metal layer, the bottom surface will be the silicon wafer. For the top surface, aluminum, tungsten, titanium, silver, chrome, and gold are some common metals that can be used. Choosing which metal depends upon several considerations. Reflectance and inertness to HF and silicon etchant are both requirements of the metal layer. For wavelengths in the visible/NIR, aluminum has the highest reflectance but cannot be used due to incompatibility with a subsequent anisotropic silicon etchant. Gold was chosen because it has a relatively high reflectance in the region of interest and is resistant to the device release process.

Two difficulties are associated with gold; an adhesion layer is needed to adhere gold to silicon nitride and gold is not compatible with integrated circuit (IC) processing. Chrome is a useful adhesion layer material, that also is compatible with th erelease process. Chrome has a very high tensile stress, requiring that the chrome thickness be minimized. A layer of ~ 50 A to 100 A of chrome was used for adhesion. Gold is incompatible with semiconductor processing, so after gold deposition equipment use is restricted to selected "gold contaminated" equipment. The equipment limitation creates a bottleneck for subsequent processing steps.

Process Flow

The mirror components discussed in the previous five sections must be combined into a feasible fabrication order to construct the deformable mirrors. The fabrication process steps are illustrated in figures 3-7, and 3-8.

The first step in the process is to etch alignment marks into the silicon wafer. These marks will be used for mask alignment in the next three process steps. Silicon (100) wafers have a 0.4 μm thermal oxide layer grown to provide electrical isolation between the silicon and the metallized areas. Only areas with metal overlying the silicon are protected with the thermal oxide. In this way the mirror perimeter is not undercut by the HF release except at the support strip traces. LPCVD PSG oxide is then deposited and etched leaving sacrificial pads. The thermal oxide and LPCVD oxide etches are both performed using a HF solution in a wet etch. The oxide present over the alignment marks initially etched into the wafer is cleared during both of these etches. A 0.5μm thick layer of LPCVD low-stress silicon nitride is then deposited. The thinned perimeter support is etched into this nitride layer. Additional alignment marks are etched with this nitride etch. A second 0.5μm nitride layer is then deposited for a combined 1.0μm thick nitride layer. To create an ohmic contact between the chrome/gold metal layer and the silicon wafer an ion implant is needed[36]. The backside of the wafer is first cleared of the deposited nitride, then ion implantation is carried out. The silicon wafers are p-type so Boron was implanted at a implant energy of 80 keV with a dose of 1×10^{15} ions/cm^2. After ion-implantation, a 2 hour thermal anneal at 850 C was performed to activate the implanted ions. Minimization of the anneal temperature is desired to avoid introducing

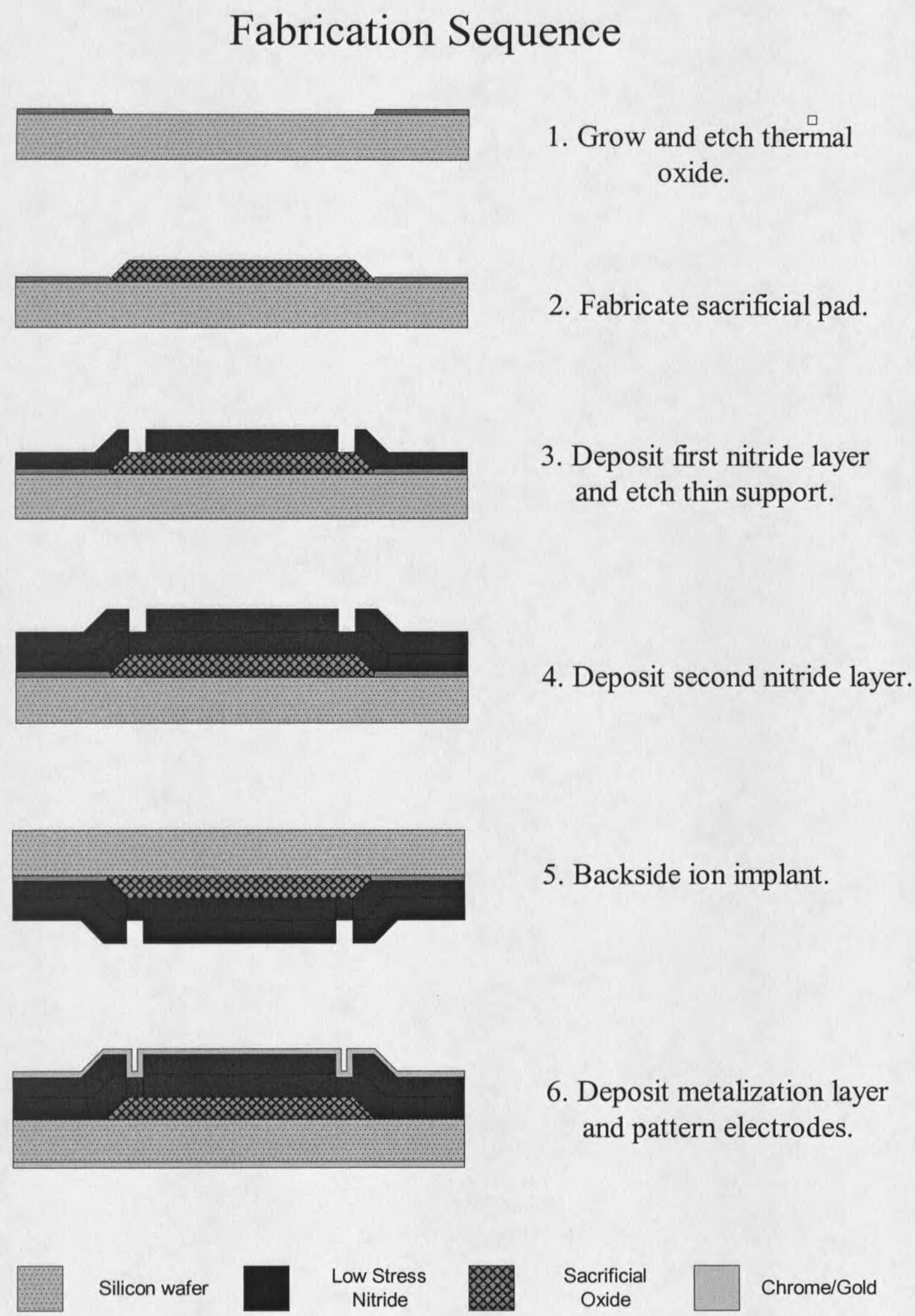

Figure 3-7. Fabrication sequence for deformable mirror

additional stress into the low-stress nitride[35]. A long 850 C anneal temperature was sufficient to anneal the ion implant and avoid increasing the residual stress. A 50 Å chrome seed layer followed with a 1000 Å gold layer is then sputtered onto the front surface and patterned to form the mirror electrodes, contact pads, and traces. The gold and chrome are subsequently etched with a wet etchant. The nitride perimeter segmentation and vias are then patterned and the nitride etched through the entire nitride thickness. A chrome/gold metal contact layer is sputtered onto the wafer backside for electrical contact. This metal layer also provides protection of the ion implanted silicon during the silicon etch in the release process.

Mirror Release

Introduction

Release of the deformable mirrors begins with the removal of the PSG oxide sacrificial layer. This etch step is accomplished using hydrofluoric acid. Subsequently, a TMAH anisotropic etch etches the underlying silicon exposed by the PSG etch.

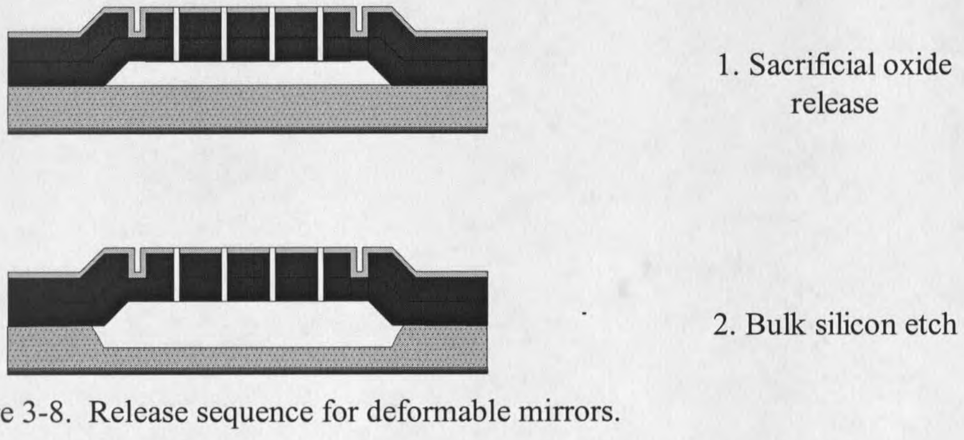

Figure 3-8. Release sequence for deformable mirrors.

<u>Sacrificial layer etch</u>

The etch rate of the PSG is governed by two parameters, the concentration of HF used and the diffusion rates of the products and reactants of the etch process. To remove the PSG oxide used as the sacrificial layer a 3:1 ratio of water:HF (49% concentrated) was used. This concentration was found to have a sufficient etch rate for the geometries of the mirrors released in this research. The etch rate of the 8% PSG oxide is given as 6000Å/min for 6:1 BOE in literature for open surfaces [37]. Due to the geometric constraints of the mirror cavity the PSG etch rate is much lower for the mirror air gaps.

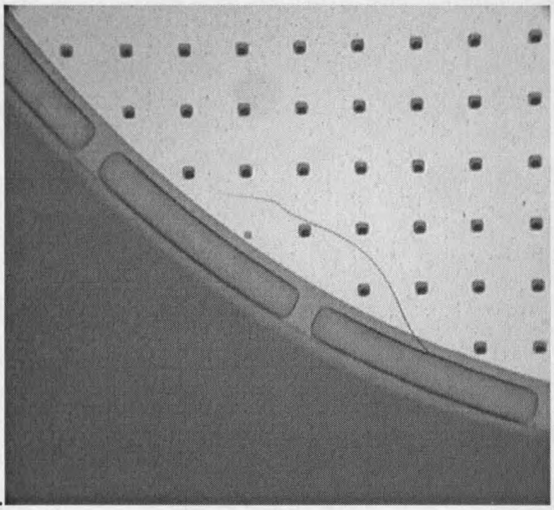

Figure 3-9. Crack in 1mm segmented mirror edge during HF etch

The geometric constriction reduces the diffusion rate of the etchant and etched products[38]. A non-segmented mirror with a 4000Å thick PSG layer requires approximately 60 minutes to release. The same device with a 2000Å PSG sacrificial layer will require 90 minutes to fully release. Segmented mirrors release quicker than non-segmented mirrors due to the openings along the perimeter. This is beneficial because nitride etches at ~50Å/minute in a concentrated (49%) HF solution. Extended HF etch times requires that exposed nitride surfaces be sufficiently thick to withstand the limited etching they will undergo in the release process. A 1μm thick mirror would be thinned to 0.60μm thick after a 1 hour etch presuming an unimpeded etch surface.

During sacrificial etching, device failure of segmented mirrors due to cracking along the mirror edge (Figure 3-9) or breaking of the support strips was observed. It has been reported that stress concentrations can occur during sacrificial etch release of surface micromachined structures.[39] A silicon "pre-etch" of the regions at the device perimeter before the sacrificial layer etch was observed to significantly reduce edge cracking and support strip failure. A 1:1 TMAH: H_2O solution was used for the pre-release silicon etch. The etch was performed at 70 C for 5minutes in duration.

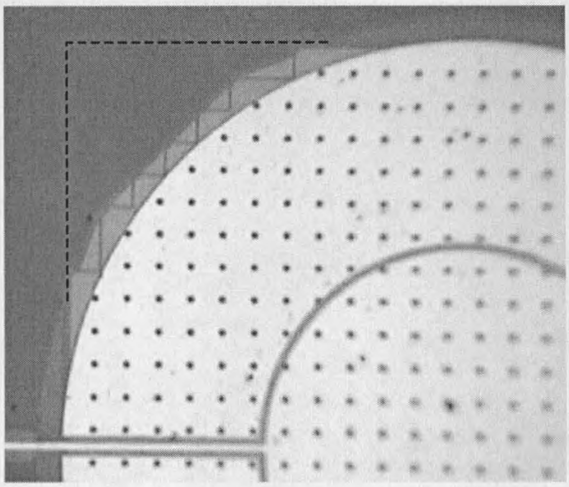

Figure 3- 10. Anisotropic TMAH etch of a 1mm non segmented circular mirror. Extent of possible undercut indicated by dashed lines

Bulk silicon etch

Bulk etching of the silicon was carried out using tetramethylammonium hydroxide (TMAH). TMAH is an anisotropic etchant of silicon, it attacks the (100) crystal planes of silicon with an etch rate up to 50 times that of the (111) crystal planes. The staircase pattern seen in figure 3-10 results from the etch front propagating away from the etch vias. At the perimeter of the sacrificial oxide pad the 100 surface is no longer directly exposed to the etchant and the etch will proceed the quickest on the intersection of the (111) planes. Eventually the etch will undercut the corner as indicated by the dashed lines. The extent of undercutting is related to the etch depth, deeper cavities requiring long etch times which, in turn, cause large lateral undercuts.

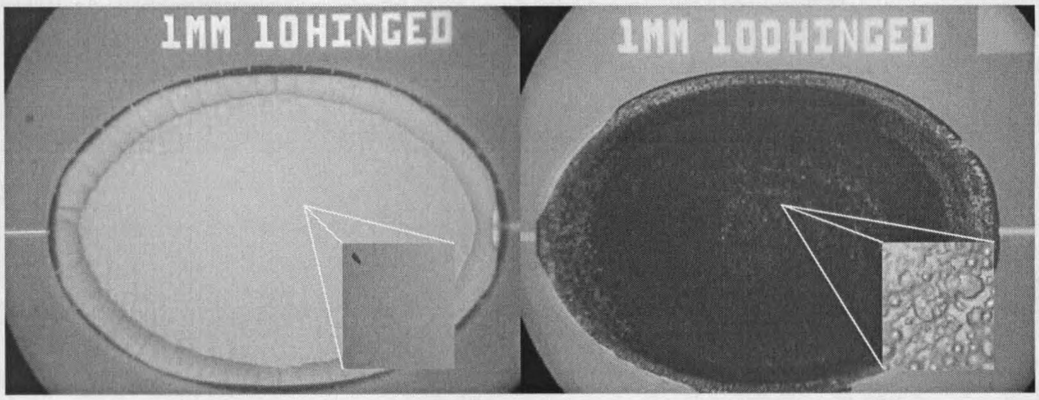

Figure 3-11. The underlying silicon substrate after a TMAH etch with a surfactant additive. The roughened surface may be due to a diffusion limited TMAH etch

A byproduct of the silicon etch is hydrogen gas. Formation of large H_2 bubbles beneath the mirror during the TMAH etch can lead to failure of the mirrors. Adhesion of the H_2 to the silicon is considered a cause of hillocks which leads to a roughened surface. Accumulation of these H_2 bubbles forms large gas bubbles which can rupture the overlying mirror[40]. A method discussed in the literature for the prevention of gas formation and elimination of hillocks is the addition of ammonium persulfate to a THAH:water mixture[41]. Inconclusive results were obtained etching with the TMAH-ammonium persulfate solution. Studies by Paranjape suggest that the ammonium persufate must be added at intervals to keep a constant concentration in the etchant solution[42]. Restricted etchant flow beneath the mirror could cause concentration variation which, in turn, may be the reason for the failure of the ammonium persulfate solution to eliminate hydrogen gas.

Effort was redirected from preventing the formation of H_2 gas to preventing accumulation of the gas on the underside mirror surface. By adding the surfactant NCW-601A, manufactured by Wako Pure Chemical Industries, Ltd. in Japan, to the TMAH solution both segmented and non-segmented mirrors were successfully released. Inclusion of WACO NCW-601A into the TMAH etch solution reduced the anistropic properties of the TMAH and slowed the etch rate. The surfactant also reversed the dependence of etch rate on concentration[43]. Silicon etch rates with 12w.t. % TMAH in water and 0.5% Waco NCW-601A surfactant at 70C were measured to be ~3μm/hour for the segmented and non-segmented mirrors. In figure 3-11, the etched silicon bottom of segmented and non-segmented elliptical mirrors from the same die are shown. These mirrors were etched in a 20 w.t.% TMAH:water solution with a 0.2% surfactant added. The etch rates were measured to be approximately 7 μm/hour for the non-segmented and

20 μm/hour for the segmented mirror. The difference in etch rate between either mirror type etched in 12% solution and the 20% solution is ascribed to the higher TMAH concentration because the etch rate is reported to be insensitive to the surfactant concentration[44].

The etch rate of the segmented and non-segmented mirrors varied from both having the same rate to the segmented mirrors etching at three times the rate of the non-segmented mirrors. An equal etch rate between mirrors with different perimeter types suggests the silicon etch is reaction limited and not diffusion limited. The etch rate difference for the segmented and non-segmented mirrors for the 20% TMAH etch concentration could be caused by a combination of phenomena. The 20% TMAH concentration etch rates may cause the etch reaction to become diffusion limited for the non-segmented mirror resulting in the uneven etch surface. Additionally, hydrogen bubbles temporarily adhering to the surface could cause the uneven etch by masking the substrate region from the etchant. Based on surface quality and an etch rate independent of segmentation the preferred etch solution is 12% TMAH at 70 C with ~ 0.1% NCW-601A surfactant.

CHAPTER 4

CHARACTERIZATION OF DEFORMABLE MIRRORS

Introduction

Characterization of the deformable mirrors is accomplished with three measurements: static surface figure, dynamic response and optical reflectance. Optical profilometery gives data on surface figure and actuation. The inner and outer, annular zone, voltages control the deformation and determines the realized optical properties of the deformable mirrors. Because these devices are used in beam scanning systems, characterization of the mirror's dynamic behavior is necessary. System resonance is a function of two physical phenomena: mechanical resonance and electrical resonance. The mechanical resonance of the mirror is determined solely by the properties of the mirror's structural material and the geometry of the structure. Electrical resonance is due to the impedance of the deformable mirror. Optical reflectance is the ratio of reflected light power in the desired diffracted order to incident light power. The reflectance of the mirrors is dependent upon the metal used for the reflective layer, surface roughness, and surface geometry such as via density and via size.

Optical Profilometery

Surface Figure

The deformable mirror is a coupled nonlinear electromechanical system. The surface figure is the shape of the deformable mirror's surface and is the defining characteristic of the device. To measure the surface figure, an interference pattern is created by incorporating the deformable mirror's surface as one arm in a Mirau interferometer. The generated interference pattern of the surface is then imaged onto a CCD video camera. A cross section of the resulting image is analyzed by polynomial fitting for quadratic and quartic curvature. These values can then be expressed in terms of optical design parameters such as focal length and aberration. Actuation parameters are also obtained from the optical profilometery data, since dependence of the deflection on applied inner and outer voltages can be determined.

Imaging Interferometer

A tabletop interferometer was built to gather the optical profilometery data. The apparatus shown in figure 1 can be broken up into three sections: illumination, interferometer, and CCD imaging. For surface profile data, an interference pattern of the deformable mirror must be superimposed on an image of the deformable mirror. The choice of an illumination source depends upon balancing the coherence that can be tolerated in imaging with the depth of focus necessary for the interference pattern. For

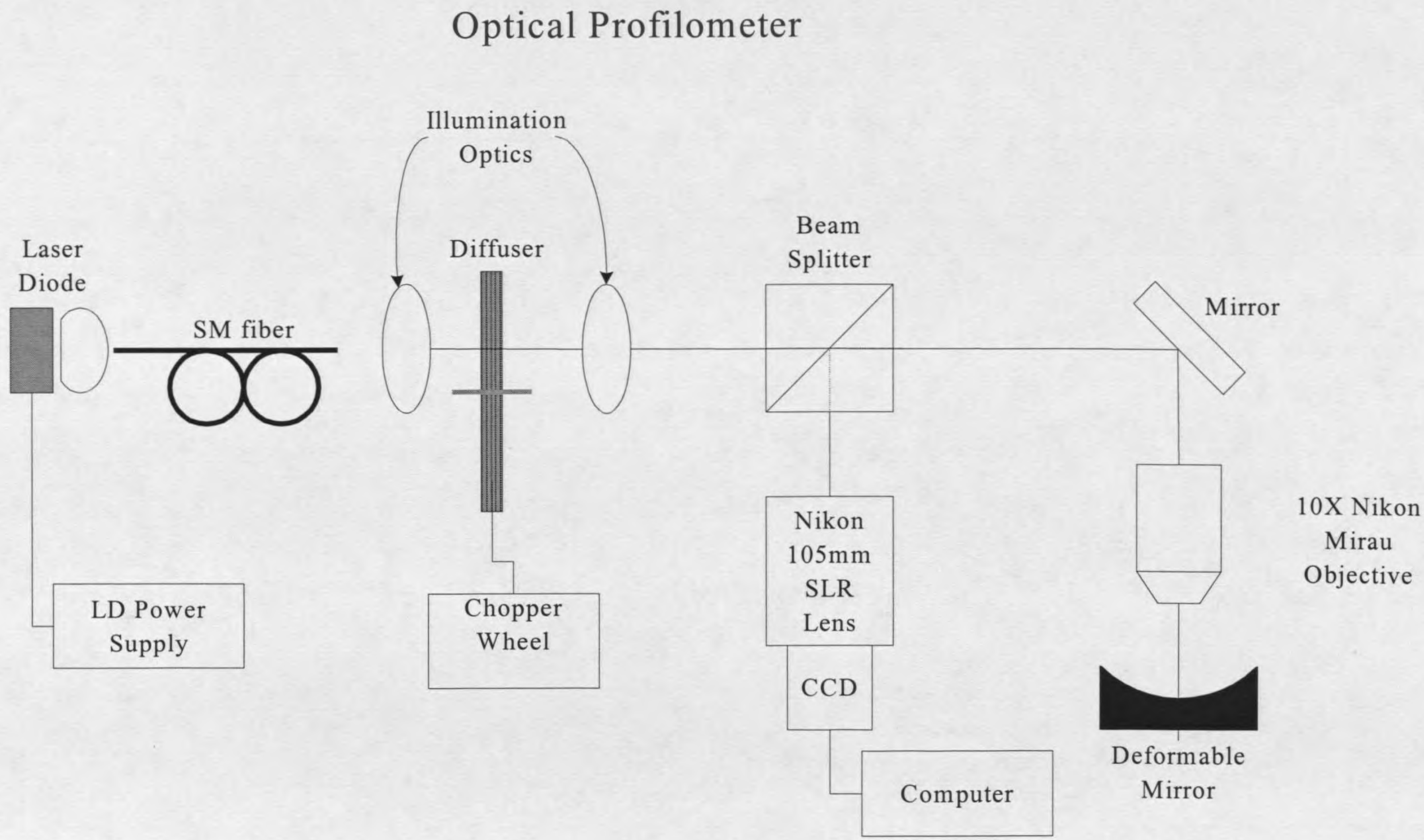

Figure 4-1. Optical profilometer layout. A 660nm laser diode with low temporal coherence is used as the illumination source. The diffuser removes effects of spatial coherence. Light backreflected from the deformable mirror is imaged onto the CCD camera .

imaging, incoherent illumination is optimal, while for interference, coherent light is optimal.

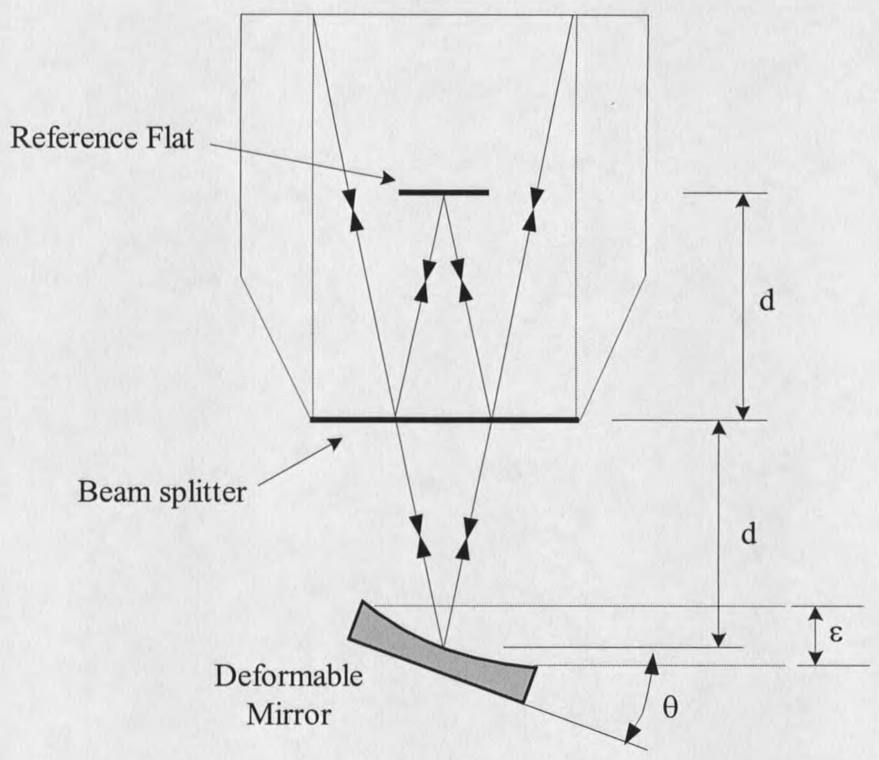

Figure 4- 2 Mirau Interferometer schematic.

The temporal coherence of an illumination source is inversely proportional to the source's spectral bandwidth. A white light source has a very short temporal coherence length (100's of nanometers) while a He-Ne laser has a temporal coherence length of about one meter [45]. The depth of field necessary for the interference measurements is shown as ϵ in figure 2. A depth of field of $10\mu m$ is adequate for the number of interference lines desired at a wavelength of 660nm. A temporal coherence length longer than 10μm is then sufficient for a clear image and a visible interference pattern. Laser diodes have temporal coherence lengths of millimeters, so a Hitachi 660nm laser diode was chosen for the illumination source.

In addition to temporal coherence, laser sources also have spatial coherence. Spatial coherence causes speckle from a reflecting surface that can obscure the image. The effects of spatial coherence are lessened by using a diffuser rotating at a frequency greater than the video frame rate. This removes any speckle from the combined image and interference pattern.

A beamsplitter is used to direct the light into the interference objective and redirect the image to a CCD camera. To generate the interference pattern, a Nikon Mirau interferometric microscope objective is incorporated into the tabletop imaging apparatus. This is a 10X objective with a numerical aperture of 0.25. The geometry of this interferometer is shown in figure 4-2. A 50/50 beam splitter on the front of the objective reflects ½ of the light to a reference mirror inside the microscope objective and transmits ½ the light out onto the deformable mirror. The reflected light from the deformable mirror recombines with the light from the reference mirror. As long as ϵ, defined in figure 2 as the difference in path lengths, is less than the coherence length of the light source, an interference pattern results. An image from the optical profilometery setup is shown in figure 4-3. The reference reflector aperture of the microscope objective is the outer circular feature that defines the extent of the fringe lines. The microscope objective was designed for use in a microscope with a tube length of 210mm and a working distance of 4mm. The tube length is the distance between the rear of the objective and the image generated by the objective. The working distance is the distance between the front of the microscope objective and the deformable mirror; this distance d is illustrated in figure 4-2.

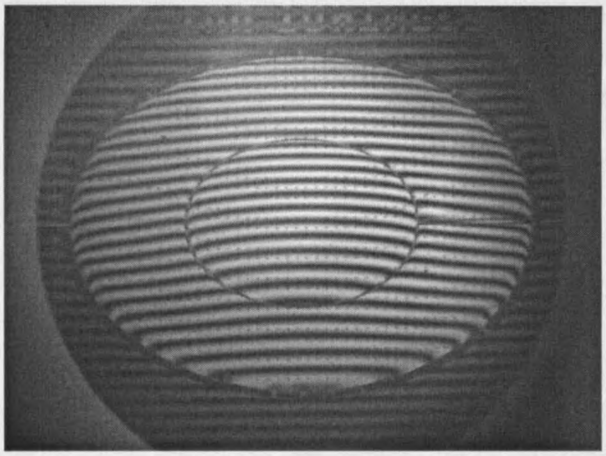

Figure 4-3. An interference pattern of a deformed elliptical deformable mirror is shown. Note the straight interference lines located off of the mirror due to the tilt of the die.

The interference pattern generated by this objective lens is imaged onto the CCD camera by a 105mm Nikon SLR lens. Using a c-mount Nikon adapter ring, the SLR lens is mounted onto a JAI CCD monochrome video camera. This camera has a 2/3" interline-transfer CCD (actual size is 8.8 mm X 6.6 mm) and outputs a video image using the EIA (RS-170) video format. This gives 485 TV lines of output using 494 effective pixels.

The number of fringes that can be resolved in an image is limited by fringe contrast and the spatial resolution of the CCD array. By tilting the deformable mirrors, the mirror edges move away from the focal plane of the microscope objective and must be accommodated by the depth of focus of the Nikon interferometer optics and the coherence length of the laser diode as discussed in the illumination section of this chapter. The magnification of the interference fringe imaging system is estimated to give 323 lines/mm of resolution. This number represents the ratio of the number of horizontal TV lines on the monitor to the spatial distance on the mirror surface. A minimum of 2 TV lines per fringe requires that the fringes are 6.2 μm wide on the mirror surface.

Digitization of the video signal is accomplished with a SONY DVMC-DM2 media converter. The DVMC-DM2 digitizes standard analog video signals for input to a PC computer using a high speed firewire (IEEE 1394) connection. A 640X480 image can be obtained which is the EIA video resolution.

Fringe Analysis Software

MATLAB code is used to analyze the images obtained from the interferometer. The JAI CCD video camera outputs an image using the EIA(RS-170) format with 480 horozontial lines of resolution. Maintaining a pixel aspect ratio of 1:1 in the 3:4 video format gives a maximum pixel resolution of 480x640. The image is loaded into MATLAB as a basic multilingual plane (BMP) format image.

A line cross-section is selected perpendicular to the interference fringes across the image as shown in figure 4-4. The resulting image intensity data is then passed through a low pass filter to remove any high frequency spatial noise. An interpolation that refines the data by a factor of ten is then carried out to refine the location of the interference peak minima. A Spline fit is used in the interpolation because the interference fringes are

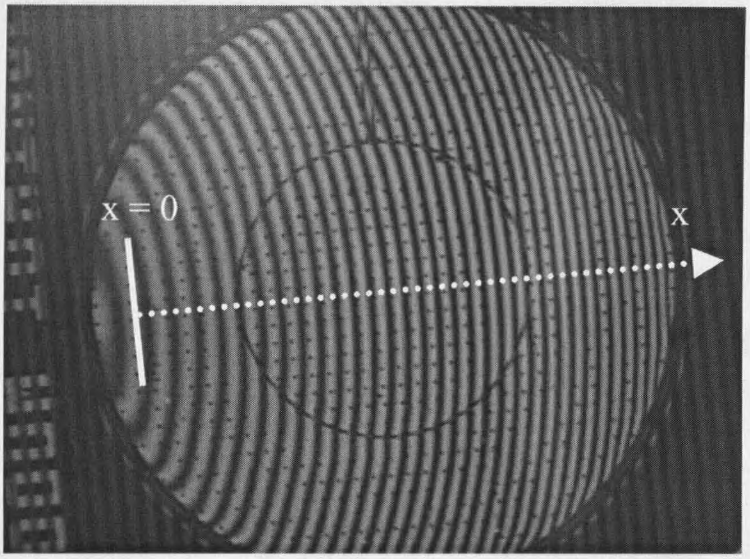

Figure 4-4. Interference image of 1mm deformable mirror. Note the fringe line thickness variation across the image. The white dashed line corresponds to the graphs in figure 4-5.

sinusoidal in nature. After interpolating the data, fringe minima are located using a fixed width window that is moved through the data looking for local minimum. Any extraneous points can then be manually removed. The relative spatial locations of the interference minima represent the tilt in addition to the curvature of the mirror. In figure 4-5a, the minima locations have been located on the line cross-section indicated by the dashed line on the interference image shown in figure 4-4. In figure 4-5b, the interference minima from 4-5a are plotted vs the calculated height, where each fringe represents a $\lambda/2$ height variation. Using a first order polynomial curve fit, the linear portion of the curvature is removed, leaving the curve shown in figure 4-5c. This curve is the surface curvature of the mirror. A even order polynomial curve fit then yields the 2^{nd} and 4^{th} order curvature coefficients which represent the quadratic and quartic curvature respectively.

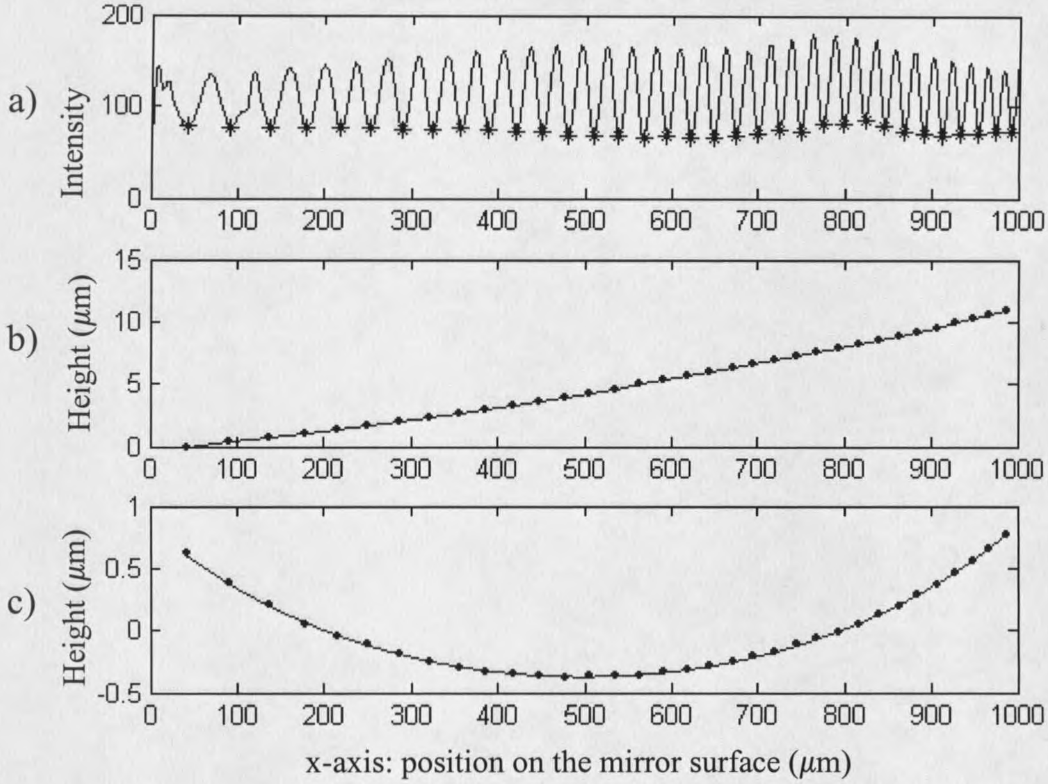

Figure 4-5. Interference data from line cross-section of 1mm mirror shown in figure 4-4. The x-axis is the location on the mirror surface and is the same axis drawn in figure 4-4. The y-axis represents the brightness of the image. a) Interference amplitude data with minima indicated with asterick. b) Plot of minima spacing versus position. Tilt of sample gives rise to $12\mu m$ tilt. c) Fringe minima with tilt removed. A 4^{th} order polynomial fit to the data is plotted.

Data analysis for two mirror configurations must be performed. For small deformations of the mirror, the die is tilted, producing parallel fringe lines across the undeformed mirror. This tilt is subsequently subtracted from the data in order to analyze the curvature of the device. As the mirror deflection increases, the fringe period increases on the downward edge of the mirror and decreases along the upward edge of the mirror, which ultimately limits the maximum mirror deformation the optical profilometer can accommodate. The mirror is therefore positioned flat for large deflections, making the fringe lines symmetric about the center of the mirror.

Dynamic Properties

Introduction

For operation in an optical beam scanning system, the deformable mirror benefits from video-rate bandwidths for focus and aberration correction. Large bandwidth will allow intra-line (or potentially pixel-by-pixel) adjustment of focus and aberration correction. Achieving these bandwidths is possible with MEMS devices due to the small size of the devices. To measure mechanical resonances a laser beam is reflected from the mirror surface into a photodector. Electrically, the mirrors have a small capacitance (~ picofarads) and an infinite input resistance. With a low impedance voltage source the electrical bandwidth is much greater than the mechanical bandwidth. This makes the deformable mirror system's bandwidth mechanically limited. Due to the low Q of the device in air, a resonance peak may not be measured. Several optical geometries can be used to measure the dynamic properties of the deformable mirrors.

Apparatus

A schematic of the dynamic measurement apparatus is shown in figure 4-6. The laser source is a He-Ne laser that is filtered through neutral density filters to prevent saturation of the photodetector. A 50/50 beamsplitter allowing normal incidence reflection is used to separate the incident beam from the reflected beam. The reflected beam passes through a 100μm diameter aperture located in front of the photodectector.

By using an aperture, variation of the reflected beam's focal length produces a variation in intensity transmitted to the photodectector.

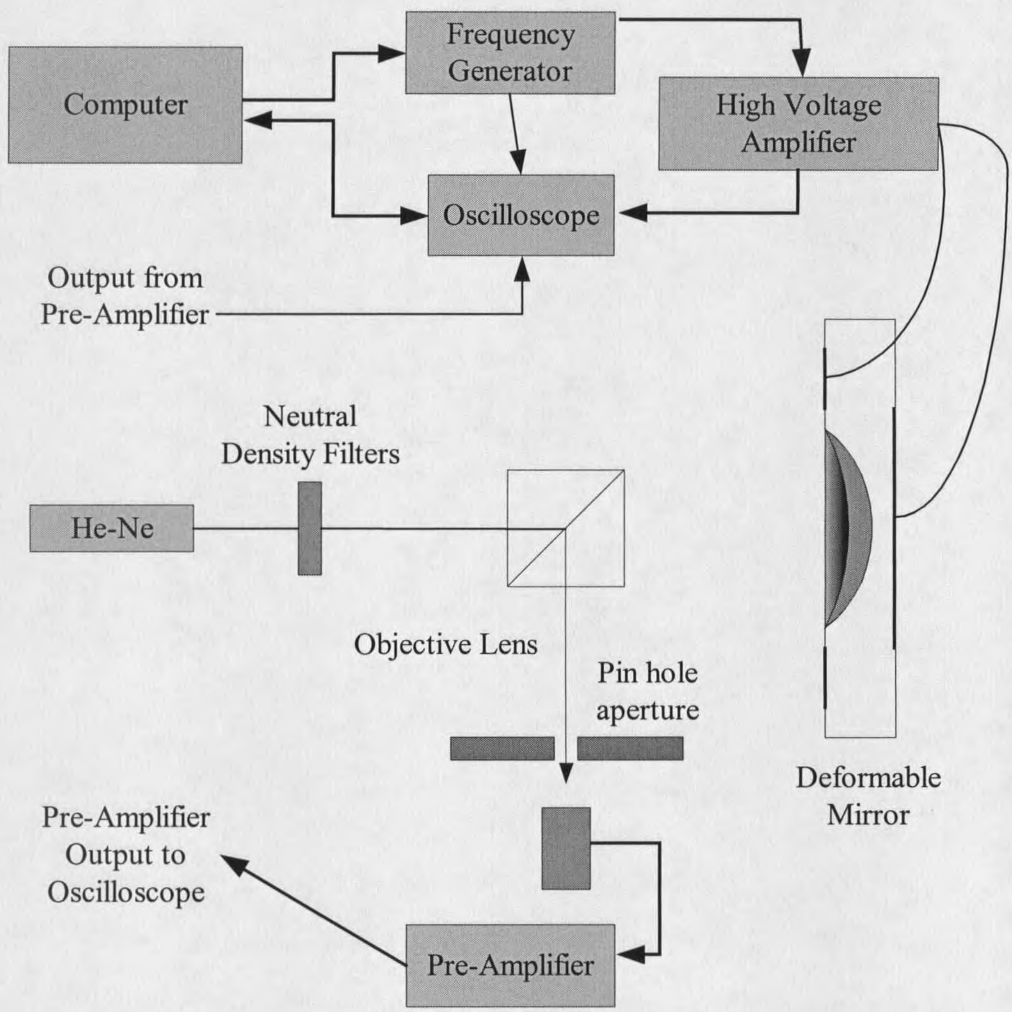

Figure 4-6. Experimental layout of dynamic response of deformable mirror.

The dynamic response measurements are controlled, via GPIB interfacing, by computer. Labview software sets the frequency and applied voltage of the HP function generator and acquires data from the oscilloscope. A Hewlett Packard 33120A function generator provides the input drive signal to a TreK model 603 power amplifier. The power supply has a 3dB 150 KHz output bandwidth at 250 volts. The photodectector is a New Focus model 2031 that has a bandpass of 1MHz. This bandwidth setting has a relatively low gain; therefore a Stanford Research Systems SR560 pre-amplifier is used to amplify the output signal before it is sent to a Tektronix TDS380 oscilloscope. Photodetector and power supply voltage amplitudes are measured by the oscilloscope and subsequently recorded in the computer.

Because the TreK power supply is limited by a 150 KHz bandwidth, corrections to the dynamic experimental data are necessary for all measurements made over 150KHz. At frequencies beyond this bandwidth, the input voltage gain is lower than the gain specified and decreases as the input frequency increases. Peak-to-peak voltages of 20 to 60 volts were used to uniformly actuate the mirrors for the dynamic measurements. This actuation voltage range corresponds to mirror deflections of approximately 0.07μm, for the 300μm mirror non-segmented mirror, to 0.15μm for the 1500μm segmented mirror. These voltages are significantly less than the 250 volt maximum output voltage of the power supply, this extends the usable bandwidth of the power supply but gain correction is needed. The measured deflection data are corrected for the finite amplifier bandwidth.

Reflectance

Input optical power to an optical system is partly determined by the reflectance of the system's components. High reflectivity is desired to minimize the required input power and prevent damage to components due to absorption of optical power. Serving the dual purpose of a mirror and electrode, sputtered gold is used as the reflective layer. Gold was chosen because it has a large reflective bandwidth from the visible into the infrared and is inert to the chemical processing used. The deformable mirror reflectance is measured by detecting the reflected optical power from a deformable mirror as compared to a gold reference mirror. The reflected beam consists of a primary reflection spot and higher order diffraction spots arising from the via pattern on the mirror surface.

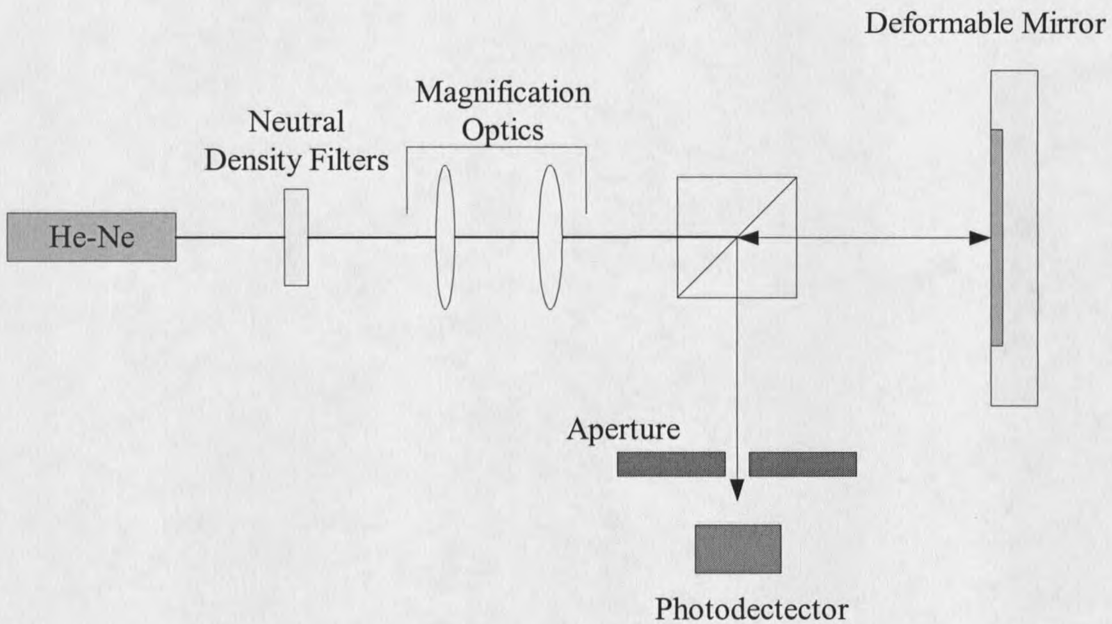

Figure 4-7. Reflection measurement experimental configuration.

The experimental setup for reflectance is shown in figure 4-7. To prevent overfill of the laser beam on the mirror, the incident laser beam is demagnified to be less than 1mm in diameter. The reflected beam passes through a 100μm diameter aperture and into a photodectector; the aperture blocks the diffracted light created by the vias. To measure the total optical power, diffracted plus reflected, the aperture is removed and a plano-convex lens is used in front of the photodetector to collect all of the light. Incident optical power is measured using a $\lambda/10$ flat gold mirror. This provides a reference point for the losses due to mechanisms other than the reflectance of the gold.

CHAPTER 5

EXPERIMENTAL RESULTS

Introduction

Experimental results obtained with the deformable mirrors are used to relate design and process variations to device performance. The tested variations discussed in chapters 2 and 3 are listed in table 5-1 along with the device performance characteristic under evaluation.

Table 5.1 List of design variations and affected operating characteristics.

Design and process variations	Operating characteristics
Diameter	Maximum usable pupil size
Thinned support	Focal range
Segmented support	Spherical aberration
Annular electrodes	Actuation voltage
Cavity depth	Bandwidth
Sacrificial layer thickness	Initial (zero volt) curvature

The design and process variations discussed are for circular mirrors that are designed for focus control and correction of spherical and defocus aberration in an on-axis optical system. Four diameters of the circular devices are examined: 1500μm, 1000μ, 750μ and 300μm. Mirrors were fabricated with and without perimeter segmentation and thinning. All mirror designs have annular electrodes, but uniform actuation can be used to emulate a single actuation zone. Cavity depth is determined during the release process and can be varied to maximize the mirror deflection for each diameter. Sacrificial layer thickness was varied during the fabrication process and mirrors with sacrificial layer thickness of 0.7μm, 0.4μ, and 0.2μm were fabricated and released. Because of the nature of the mirror fabrication process, residual stress was not studied but residual stress has a significant role in the behavior of the devices, in both surface figure and frequency response. The physical origin and consequences of residual stress is discussed in the fabrication process section of chapter 3.

The operating characteristics are those that are necessary for implementation of a deformable mirror into a beam scanning optical system. Pupil size is the largest diameter optical beam that can be accommodated by the mirror for the intended purpose of a specified optical system. Focal length and spherical aberration are the primary optical qualities to be tested. To achieve a specific focal length and/or spherical aberration it is necessary to deflect a mirror an amount δ which is dependent upon the load, diameter, and perimeter support. Optical systems using a deformable mirror typically have dynamic requirements that specify an acceptable lower bandwidth. The bandwidth fixes an upper limit on dynamic correction of focus and aberration with the mirror. Initial curvature of the mirror limits the longest possible focal length obtainable by that mirror. Ideally, the released mirror should be flat, yielding an infinite focal length with no aberration. Characterization of deformable mirror design variations will be based on results obtained using a 1mm device where possible, without thinning or segmentation of the perimeter, as a reference device to which other devices will be compared.

Device design variation

Attributing variations in design and process parameters to the operational characteristics requires isolating the effect of each of the variations on the operational characteristics. Isolating design variation effects is complicated because of the interdependence of the operating characteristics for each design or process change. The influence of the diameter on the device characterization can be understood from theory as long as no other modifications to the mirror geometry are made. The transition from plate to membrane behavior occurs as mirror diameters increase for small displacements under uniform loads. Perimeter modification carried out as perimeter thinning or segmentation may alter the initial curvature of the mirror edge as well as change the curvature at the mirror perimeter as a load is applied to the device. The effects of perimeter modification manifest themselves as changes in both 2^{nd} and 4^{th} order curvatures for a given applied pressure. Cavity depth determines the necessary actuation voltage to deform the device. The greater the cavity depth, the further a mirror may be deformed, with the cost being a higher actuating voltage. The maximum voltage that can be applied is the limiting operating parameter of these mirrors, the maximum voltage being fixed by the breakdown voltage of the nitride/oxide dielectric beneath the electrode and arcing between the inner and outer electrode.

Surface figure

Circular deformable mirrors used for focus control typically require minimal spherical aberration of the mirror's surface. The magnitude of acceptable aberration is ultimately fixed by the intended optical system, but $\lambda/10$ is adopted as a target maximum amount of optical aberration which can be introduced by the deformable mirrors described in this paper. Because the mirror introduces twice the aberration, into the reflected optical wavefront, that is present on the mirror surface, $\lambda/20$ is the maximum allowable mirror surface aberration. Unless otherwise stated, all aberration discussed in this chapter will be the optical aberration of the wavefront. The usable focal length of a deformable mirror is determined by the amount of center deflection for a given diameter and the ability to zero out spherical aberration at that deflection.

Comparison of focusing results with uniform actuation and independently actuating the inner and outer electrodes demonstrates the effectiveness of an outer annular electrode. The effect of segmentation and thinning of the perimeter can be seen by comparing mirrors with and without the perimeter alterations.

Surface curvature data fitting

Surface figure data was acquired using a Mirau interferometer as described in the imaging interferometer section of chapter 4. A line profile is obtained from the

$$z = a_2 r^2 + a_4 r^4 \qquad (5\text{-}1).$$

interference image and fit to an even term 4^{th} order polynomial (equation 5-1). Error due to resolution constraints of the interferometer limits the accuracy of the surface curvature fit.

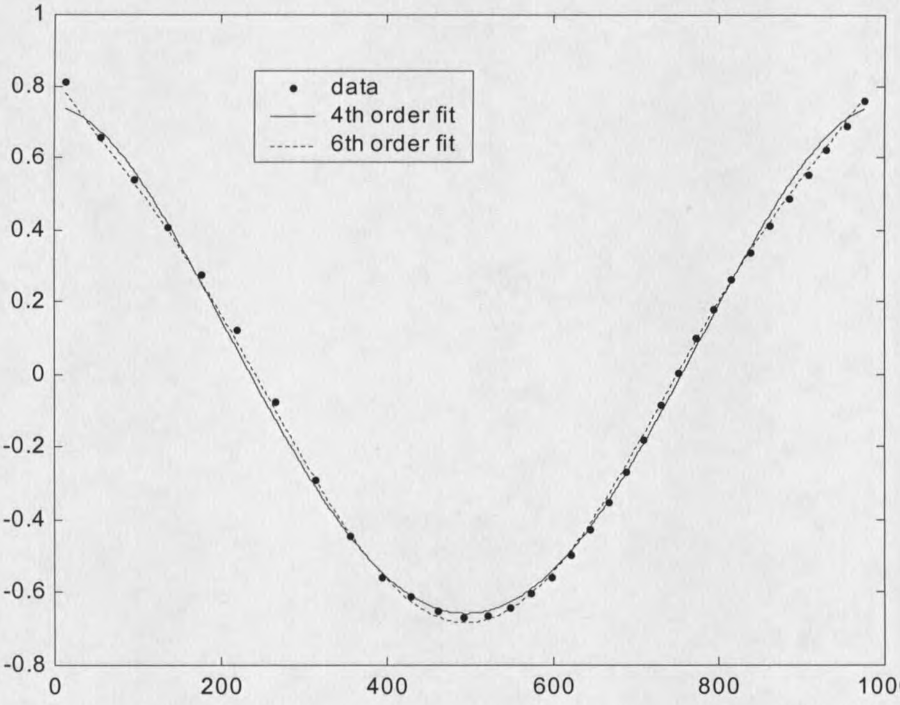

Figure 5- 1. Cross section profile of 1mm 10% support mirror showing 4^{th} and 6^{th} order curvature. Maximum 4^{th} order error is 0.11λ at 640nm illumination.

In chapter 2, it was shown that the surface curvature of clamped and simply supported plates with residual stress had a modified Bessel function solution given by equations 2-18 and 2-19. It can be seen that a 4^{th} order polynomial is an approximation to the actual curvature of these plates. Error can arise from omitting higher order terms. To ascertain the experimental error incurred in the surface figure measurement by approximating the curvature with equation 5-1 a "goodness of fit" of the polynomial approximation is used to define the distance between the fit polynomial and the mirror surface. For example in figure 5-1, the surface curvature of a 1mm mirror is fit to a 4th order polynomial with a maximum error of 0.11λ using 0.66nm light. This maximum error occurs at a radius of 486μm from mirror center. This result represents a worst case scenario, the mirror being actuated using zero outer voltage and the maximum inner voltage allowed by snapdown.

The surface profile experimental apparatus (see chapter 4) has a surface figure accuracy of approximately λ/20 estimated by imaging the surface profile of a flat reference mirror. This profiling resolution gives a noise floor to measured focal length and spherical aberration values, obtained from the interference image data, corresponding to deflection distances of ~0.033μm.

Membrane Behavior

From theoretical considerations it is known that a membrane deforms with parabolic curvature. Insofar that a mechanical plate with a large residual stress acts as a membrane, applying an equal voltage on both electrodes should produce purely quadratic curvature of the device.

Shown in figure 5-2, spherical aberration experimental data from 300, 750, 1000, and 1500μm mirrors are plotted verses uniform actuation pressure on the mirror. The deviation of the mirrors from a parabolic curvature demonstrates that presuming membrane behavior under a uniform load is incorrect.

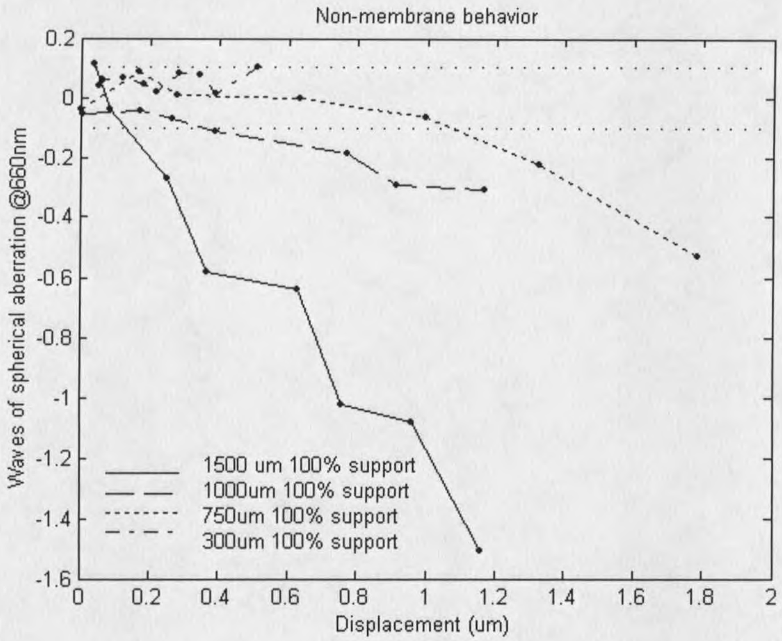

Figure 5- 2. Spherical aberration with uniform loading. Mirrors 0.30, 0.75, 1.0, and 1.5mm in diameter subject to a uniform load. Experimental data is indicated by the dots. Cavity depths for the mirrors are all 7μm except for the 300μm mirror which has a 6μm air cavity depth.

As shown in figure 5-2, spherical aberration for the 300 and to a lesser extent the 750 μm mirrors is less then $\frac{\lambda}{10}$ for center deflections less than 1μm. The source of spherical aberration in the larger mirrors is thought to be the non-uniform pressure experienced by the deflected mirrors. Center displacement of the mirror creates a non-uniform cavity depth beneath the mirror. The pressure created from the electric field is dependent on the inverse square, r^{-2}, of the gap between the bottom of the cavity and the mirror. The 1500μm mirror has an air cavity of approximately 7μm so a deflection of 1μm with a voltage of 70 Volts creates a pressure difference of 200 Pascals between the mirror center and perimeter. For a 1500μm mirror, this pressure difference is significant;

a pressure of 200Pa causes 0.3μm of deflection in mirrors 1500μm in diameter. The air cavity beneath the 1000 and 750μm mirrors is also approximately 7μm so the pressure difference from center to edge is the same for these mirrors. The 300μm mirror has an air cavity of 6μm.

In summary, the larger diameter mirror's curvature is more susceptible to aberration, caused by a radial pressure difference due to the lower actuation pressures needed for mirror deformation. The fractional percent of the cavity depth that the mirror is displaced is important in calculating the degree of the differential pressure, experienced by the mirror surfacee, as pressure is applied. To correct for the spherical aberration, caused by non-uniform pressure across the mirror surface, actuation zones can be used.

Actuation Zones

Active surface figure control for the deformable mirrors is achieved using two actuation zones. This surface figure control allows spherical aberration adjustment and focus control to be accomplished using a single optic. The influence of two-actuation zones on a surface figure was studied using FEA (as discussed in chapter 2). A large degree of curvature control was indicated although intrinsic stresses were not included in the model. This limits the scope of the model's applicability. Curve fitted experimental data shown in figure 5-3 for a 1 mm mirror illustrates the effectiveness of this two-zone actuation scheme. The curve labeled (- -) is the curvature created by actuating only the inner electrode. The negative optical spherical aberration caused by the mirror surface is $-2.25\times10^{-11}\mu m^{-3}$ corresponding to -2.1 λ of spherical aberration at 0.66μm illumination. Actuating only the outer electrode creates the curvature shown by the dotted line. Mirror curvature with this actuation profile creates $1.095 \times 10^{-11} \mu m^{-3}$ of positive spherical aberration in the mirror curvature. This corresponds to $+1.04\ \lambda$ of spherical aberration. Surface curvature under uniform actuation is shown for comparison. The obtained spherical aberration range for the $1000\mu m$ mirror with 10% segmentation is $3.1\ \lambda$ at $0.66\mu m$ illumination.

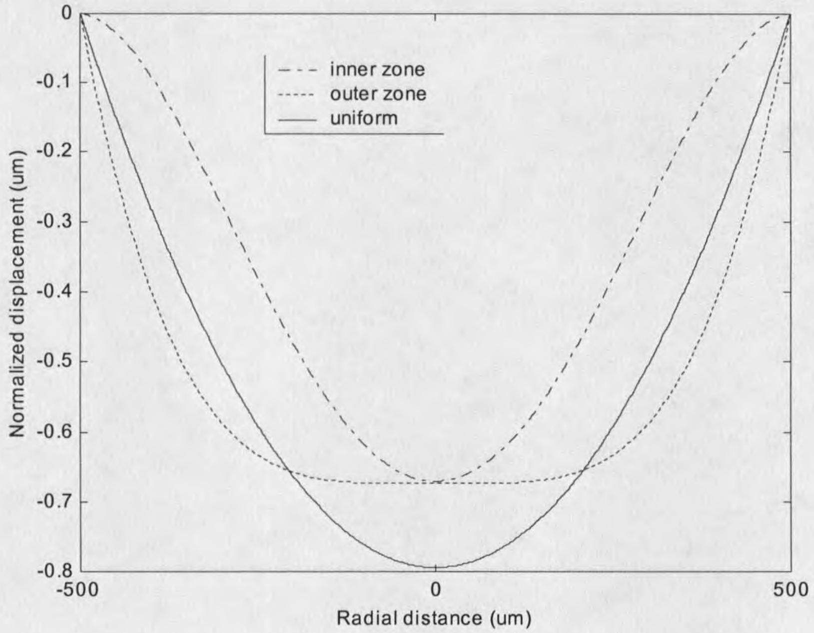

Figure 5- 3. Zonal actuation comparison. Curvatures are for a 1mm 10% supported mirror. Surface figure profiles for inner actuation, outer actuation and uniform actuation are shown.

Contour plots showing the focal length and spherical aberration ranges for a 1mm non-segmented mirror with a $7\mu m$ air cavity depth are shown in figure 5-4 and 5-5. The focal length range is contoured using the quadratic coefficient a_2 in equation 5-1, in units of μm^{-1}. Similarly in figure 5-5 the spherical aberration is given in terms of the quartic coefficient a_4 from equation 5-1, in units of μm^{-3}. A rectangular grid of data points is generated from experimental data and the grid data is used to create the contour plots. The x-axis represents the inner zone actuation voltage and the vertical axis represents the outer zone actuation voltage. Positions on the contour plots are given in terms of a voltage pair denoted with brackets {inner voltage, outer voltage}. Profile resolution error for the 1mm mirrors is approximately $1.3x10^{-7}$ μm^{-1} in quadratic curvature and $5.3x10^{-13}$ μm^{-3} in quartic curvature.

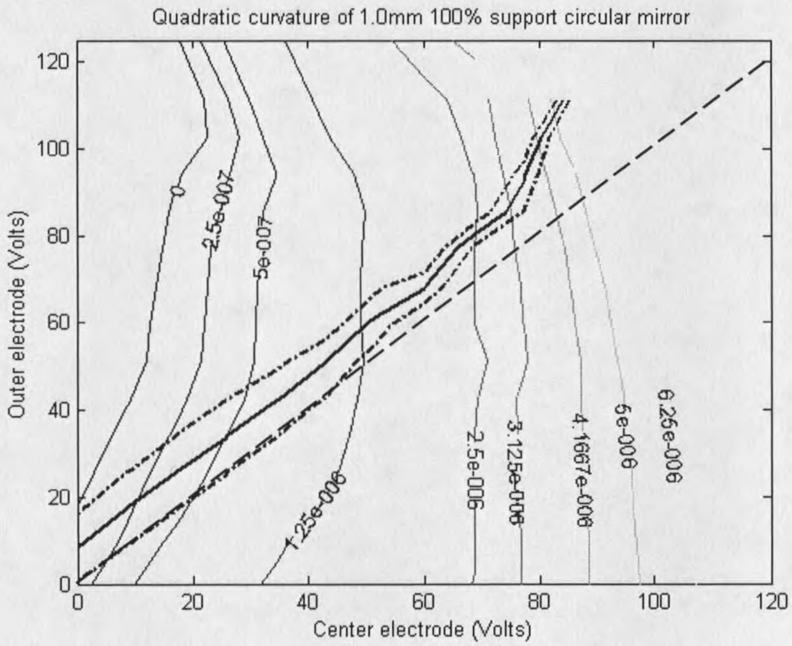

Figure 5- 4. Contour plot of the quadratic curvature, a_2, for a 1mm non-segmented mirror. The two dash-dot outer lines denote $+\lambda/10$ (top left) and $-\lambda/10$ (bottom right) optical spherical aberration. The central solid line denotes zero spherical aberration. Uniform actuation is given by $V_{inner}=V_{outer}$ and is indicated by the dashed line connecting the voltage pairs (0,0) to (120,120). Mirror cavity depth for the mirror tested is $7\mu m$.

Overlaying the quadratic curvature contours in figure 5-4 are three contours of constant quartic curvature. The center solid line represents zero spherical aberration.

The two outer dashed lines demark positive and negative λ/10 optical spherical aberration for 0.66μm light, the top line locating positive λ/10 spherical aberration and the bottom line negative λ/10 spherical aberration. Note that optical spherical aberration is twice that of the surface curvature spherical aberration. The mirror behavior changes at a quadratic curvature of $3.1x10^{-6}$ corresponding to a displacement of 0.78μm of displacement. In figure 5-4, from voltage pair {80,80} to {100,100}, the mirror's zero aberration curve shows a greater dependence upon the outer electrode for spherical aberration control. This is thought to be due the non-uniform loading resulting from the non-uniform gap. Overall the mirror's inner electrode primarily controls the quadratic curvature with the outer electrode having a minor effect.

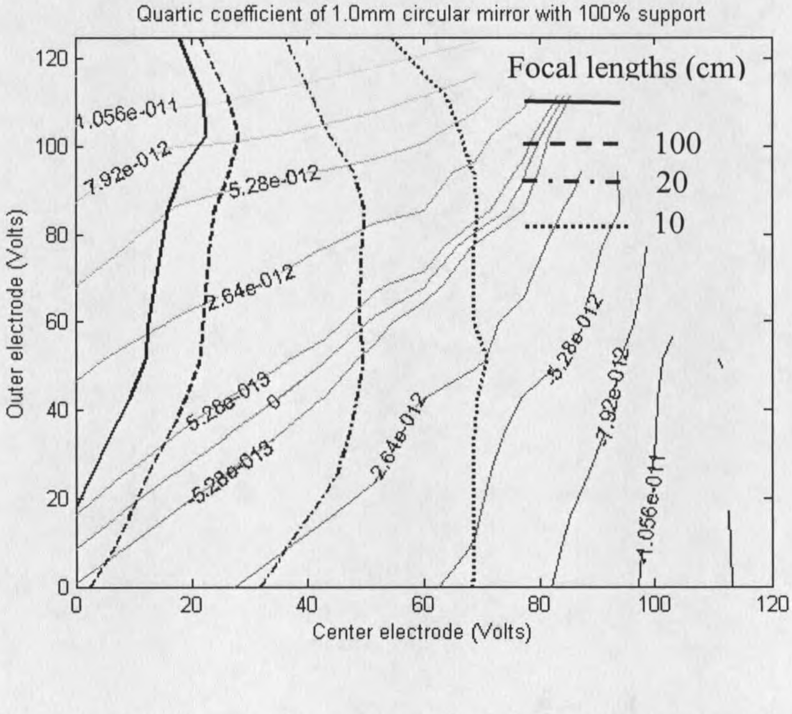

Figure 5- 5. Contour plot of a quartic curvature for a 1mm non-segmented mirror. Contours of constant quadratic curvature are plotted as focal lengths of ∞, 100, 20, and 10cm as indicated in the legend. The mirror cavity depth is 7μm

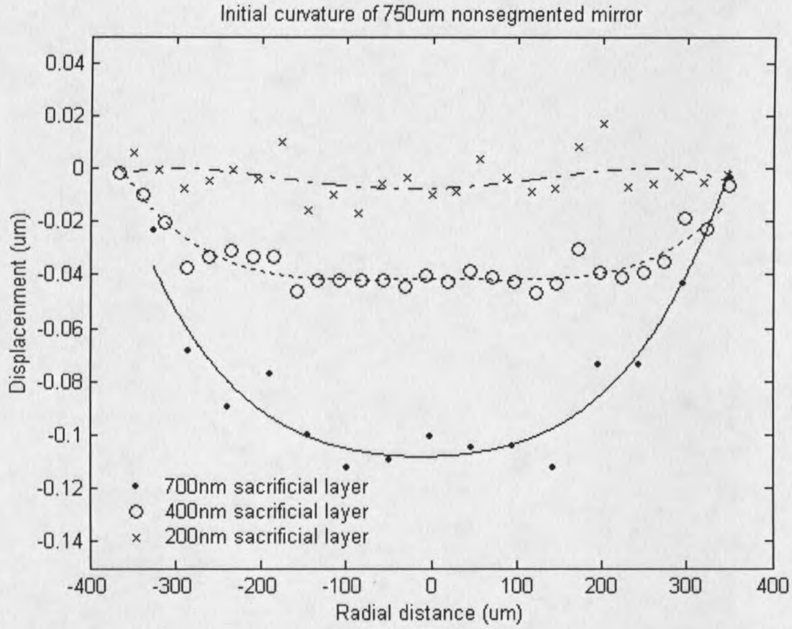

Figure 5- 6. Surface curvature of a 750μm 100% supported mirrors with zero voltage applied. Mirrors have 700nm, 400nm, and 200nm of sacrificial oxide beneath a 1μm structural layer of silicon nitride.

Spherical aberration of the 1mm mirror is shown in figure 5-5 with overlying lines of constant quadratic curvature. From left to right in figure 5-5, the lines of constant quadratic curvature are 0, 2.5x10^{-7}, 12.5x10^{-7}, and 2.5x10^{-6} μm^{-3}. These curvatures correspond to focal lengths of ∞, 100cm, 20cm, and 10cm respectively as indicated on the figure. Quadratic curvature is related to the focal length by $a_2 = \frac{1}{4f}$ where f is the focal length. As seen in figure 5-5, the quartic curvature range is more dependent on the quadratic curvature of the mirror.

Sacrificial layer thickness variation

Due to the modified surface micromachining process, the sacrificial layer thickness can be varied. The thinning the sacrificial layer is advantageous for reducing the bending moment at the boundary, (as discussed in chapter 3) but detrimental since they increase release etch times. Observed variation of mirror surface figure for non-actuated mirrors has also been attributed to the sacrificial layer thickness. The sacrificial layer of PSG oxide beneath the nitride mirror creates a sloping step-up onto the mirror surface. Mirrors with thicker PSG layers have longer and or steeper sidewalls on the mirror perimeter, producing a larger bending moment. These sidewalls are thought to be responsible for the surface figure variation.

Surface figures for 750μm diameters mirrors with 0.2μm, 0.4μm, and 0.7μm of PSG oxide are compared in figure 5-6. With 0.7μm of PSG, a 750μm diameter mirror has $\{a_2, a_4\}$ coefficients of $\{3.6\text{x}10^{-7}, 3.6\text{x}10^{-12}\}$ representing an initial center deflection of 0.12μm. The 0.4μm PSG mirror has $\{a_2, a_4\}$ coefficients of $\{0.3\text{x}10^{-7}, 2.4\text{x}10^{-12}\}$ representing an initial center deflection of 0.04μm. The 0.2μm PSG mirror has $\{a_2, a_4\}$ coefficients of $\{1.9\text{x}10^{-7}, -1.3\text{x}10^{-12}\}$ with a center deflection of 0.002μm, which is evidence that the polynomial coefficients a_2 and a_4 are fitting noise. This is also seen in figure 5-6. Measurement error for 750μm diameter mirrors is $1.4\text{x}10^{-7}\mu\text{m}^{-1}$ and $1\text{x}10^{-12}$ for a_2 and a_4 respectively.

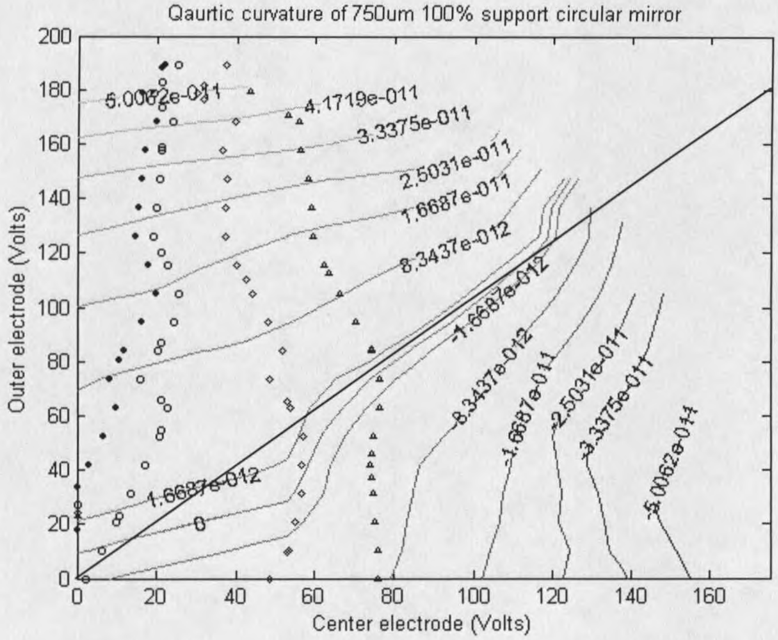

Figure 5- 7. Quartic curvature contour plot of 750μm diameter 100% support mirror with 0.2μ thick PSG sacrificial pad. Contours of constant focus are plotted as follows: ●= 0, ○=100cm, ◊=20cm, and Δ=10cm focal length. The solid black line delineates the V_{inner}=V_{outer} line.

Data for comparing the 0.2μm and 0.4μm sacrificial layer effects on surface curvature are obtained from 750μm diameter mirrors without segmentation. Quartic curvature for the 750μm mirror with 0.2μm of PSG is shown in figure 5-7. Etched cavity depth was measured to be approximately 7μm. Figure 5-8 is the equivalent contour plot for a 750μm diameter mirror fabricated with a 0.4μm thick sacrificial layer. Looking at the uniform loading behavior (V_{inner}=V_{outer}) it is seen that mirror with the 0.4μm sacrificial layer will deform with larger negative spherical aberration. Also, the thicker sacrificial layer leads to more zero-voltage spherical aberration, and aberration free focus is not achieved until V_{inner} is greater than ~35 volts with a focal length less than 100 cm.

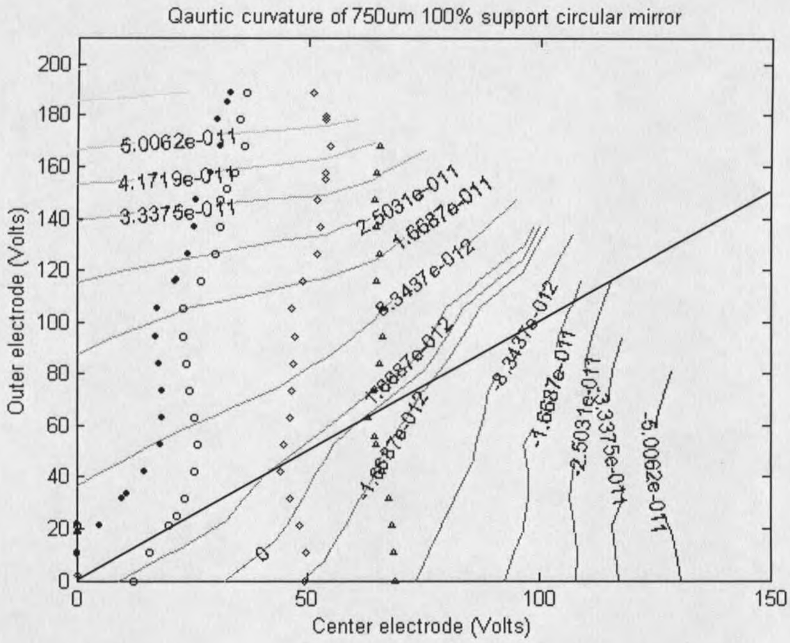

Figure 5- 8. Quartic curvature contour plot of 750μm diameter mirror with 0.4μ thick PSG sacrificial pad. Contours of constant focus are plotted as follows: ●= 0, ○=100cm, ◊=20cm, and Δ=10cm focal length. The solid black line delineates the $V_{inner}=V_{outer}$ line.

Perimeter modification

The deformable mirror's primary role is as a focus control mirror. A mirror with a simply supported boundary under a uniform load deforms with less spherical aberration than a mirror with a clamped boundary (shown in chapter 2). A weakened perimeter should also reduce the applied load necessary for actuation, i.e. lower the operating voltage of the device. Emulating the simple supported boundary condition was accomplished by segmentation and thinning of the mirror boundary.

Segmentation The effect of the segmentation is examined for influence on focal range, spherical aberration and actuation requirements. Segmentation of the perimeter was chosen so that there was 10% support along the boundary making 36° of the perimeter supported. A support every 15° was chosen, resulting in 24 nitride support strips. For the 1mm mirrors this corresponds to support strips approximately 13μm wide. Comparison of the segmented mirror curvature data, shown in figures 5-9 and 5-10, is made to non-segmented mirror curvature data, shown in figures 5-4 and 5-5, for effects of the segmentation. Comparison with voltage data is possible because the cavity depths are 7μm for the two mirrors.

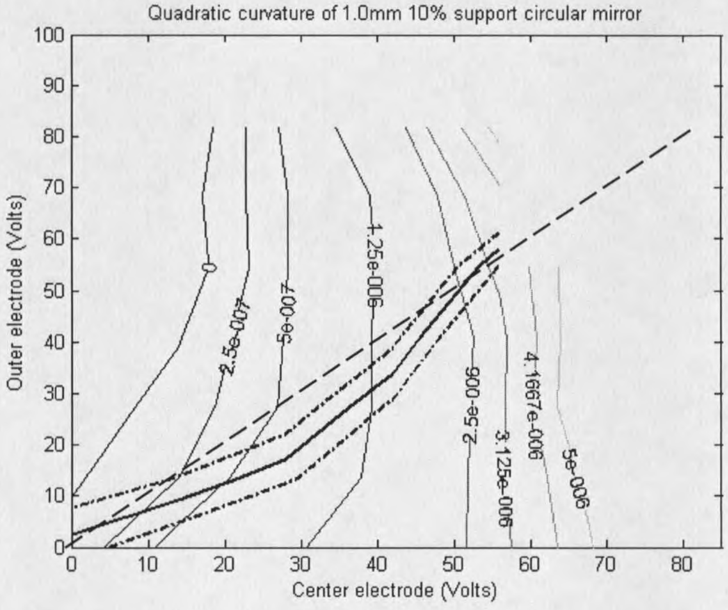

Figure 5- 9. Quadratic curvature of a 1mm 10% supported mirror. The two dash-dot outer lines denote $+\lambda/10$ (top left) and $-\lambda/10$ (bottom right) spherical aberration. The central solid line denotes zero spherical aberration. Uniform actuation is given by $V_{inner}=V_{outer}$ and is indicated by the heavy dashed line connecting the voltage pairs (0,0) to (80,80).

A contour plot of the quadratic curvature dependence upon inner voltage and outer voltage is shown in figure 5-9. Contours of +/- $\lambda/10$ and 0 waves of spherical aberration for 0.66μm light overlay the quadratic contours. As in figure 5-3, the two outer dashed lines demarcate positive and negative λ/10 optical spherical aberration for 0.66μm light, the top line locates positive λ/10 aberration and the bottom line negative λ/10 spherical aberration. The center solid contour is zero spherical aberration. Initial focus control along the contour on zero spherical aberration, less than 40 volts applied to the inner actuator, is seen to have a shallower slope with regards to the inner electrode voltage.

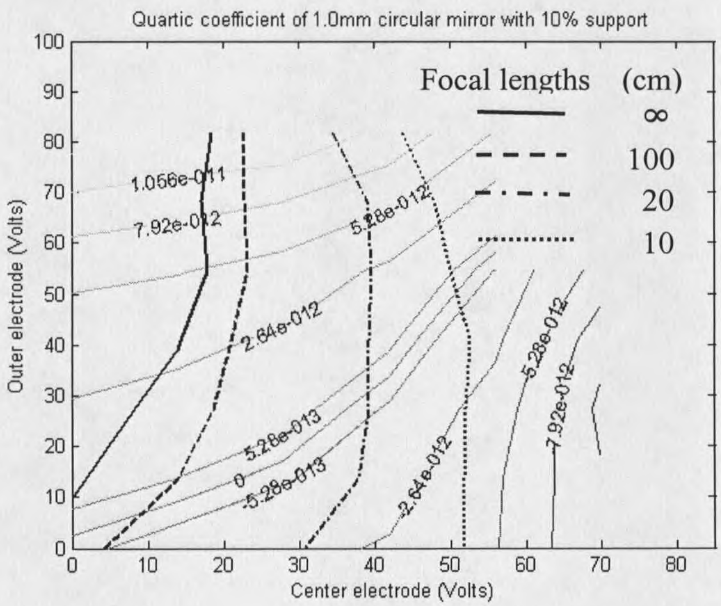

Figure 5- 10. Quartic curvature of a 1mm 10% supported mirror. The mirror cavity depth is 7μm. Contours of constant quadratic curvature are plotted as focal lengths of ∞, 100, 20, and 10cm as indicated in the legend.

At larger quadratic curvatures (shorter focal lengths) the segmented mirror exhibits a compliance not seen in the non-segmented mirror quadratic contour data. The curvature implies that a smaller voltage applied to the 10% segmented mirrors can create a larger deflection, i.e. a shorter focal length. This is anticipated due to the weakened perimeter. Table 5-1 lists minimum and maximum quadratic curvature values for segmented and non-segmented 1000μm diameter mirrors. This data is from the zero spherical contours shown in figures 5-3 and 5-5. Both mirrors were released with an air cavity depth of 7μm +/-1μm so the applied voltage to the inner and outer electrodes can be compared between

Table 5-2. Quadratic coefficient range for 1000μm diameter mirrors maintaining zero spherical aberration.

		Perimeter modification	
		Non-segmented	10% segmented
Maximum quadratic coefficient		$4.17x10^{-6}$ (f = 6 cm)	$3.56x10^{-6}$ (f = 7 cm)
	Inner voltage	80	56
	Outer voltage	101	61
Minimum quadratic coefficient		$8.75x10^{-8}$ (f = 285 cm)	$6.9x10^{-8}$ (f = 362 cm)
	Inner voltage	0	0
	Outer voltage	9	2

the mirrors without converting to an applied pressure. The minimum quadratic curvatures of both mirrors listed in table 5-1 are within the measurement error of the surface profile measurement. That the maximum obtained quadratic curvature of the non-segmented mirror is greater than the segmented mirror is expected, but the stated values should not be assumed to be the maximum possible values. Error in cavity depth measurement coupled with the sensitivity of mirror behavior in proximity to the snapdown threshold would make such an assumption suspect. The compliance of the 1000μm segmented mirror's perimeter results in increased focus for the same center electrode pressure and a greater sensitivity of spherical aberration to the outer electrode load.

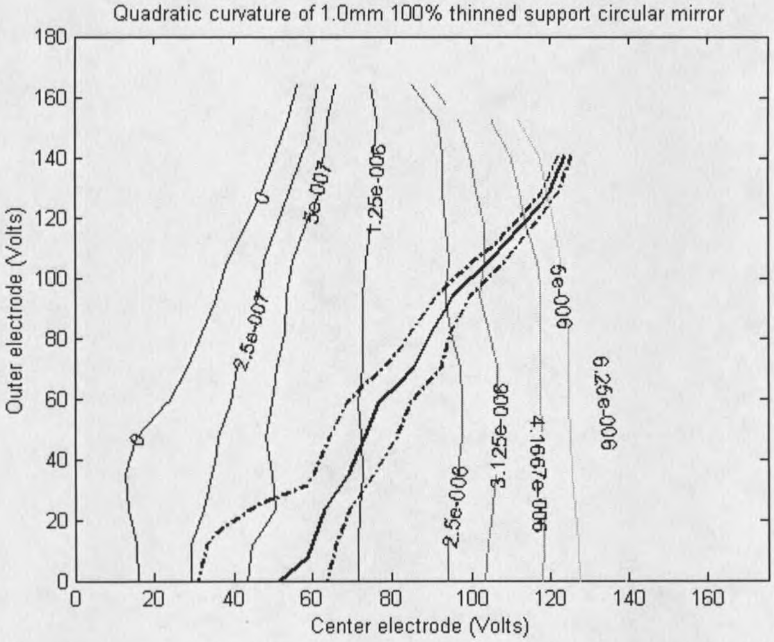

Figure 5- 11. Contour plot of quartic curvature vs applied voltage of 1 mm thinned support mirror

<u>Thinning</u> Similarly, thinning of the perimeter is also examined. Thinning was performed along a 5μm wide annular ring along the mirror's perimeter. The amount of thinning for the mirror tested was measured with an AFM to be 0.28μm leaving a 0.70μm thick support. The mirror tested is a 1000μm mirror without segmentation. Sacrificial pad thickness was 0.4μm for this device, so surface figure variance due to the sacrificial

pad thickness must be accounted for. The thinned mirror has initial curvature, giving a positive spherical aberration at zero voltage.

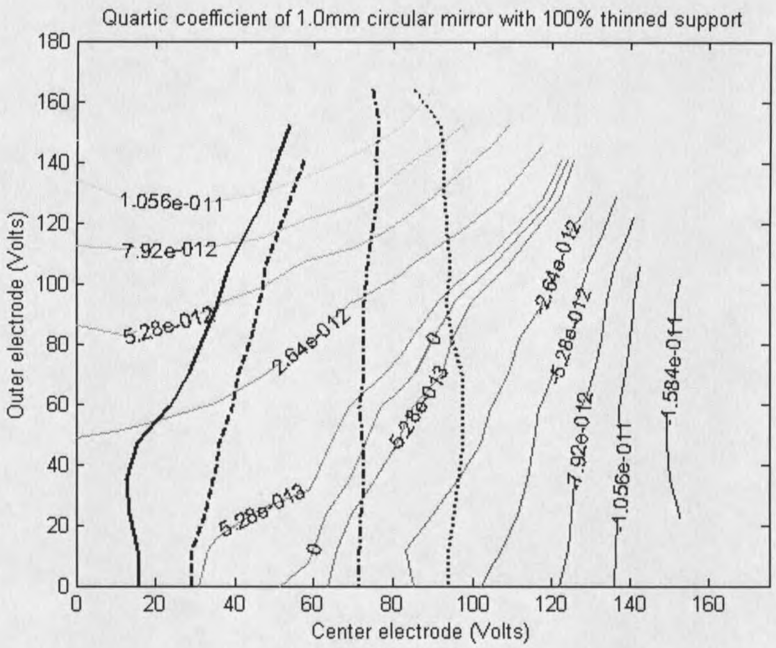

Figure 5- 12. Contour plot of quartic curvature of an actuated 1000μm diameter mirror.

Quartic curvature range for the 1000μm diameter deformable mirror is given in table 5-3 for non-segmented, segmented, and thinned perimeter mirrors. Data are given for two focal lengths: 100cm and 10cm. Variation of the quartic curvarture range with quadratic curvature is seen in the contour plots for each type of perimeter, so the difference between minimum and maximum quartic curvatures is expected to vary. The large minimum quartic curvature, at a 100cm focal length, for the thinned 1000μ mirror is attributed to the thicker sacrificial layer of that device. For the three perimeter types, negative spherical aberration is produced by inner electrode actuation.

Table 5-3. Influence of perimeter modifications on spherical aberration range for 1000μm diameter mirrors.

Quartic coefficient range (λ values assume optical abberation @ 660 nm)				
		Perimeter modification		
		Nonsegmented	10% segmented	Thinned
Infinite Focal length	Maximum quartic coefficient	1.6×10^{-11} λ ~ 3	1.17×10^{-11} λ ~ 2.2	1.51×10^{-11} λ ~ 2.8
	Inner voltage	17	18	56
	Outer voltage	127	78	159
	Minimum quartic coefficient	5.78×10^{-13} λ ~ 0.1	7.2×10^{-13} λ ~ 0.13	1.08×10^{-12} λ ~ 0.2
	Inner voltage	0	0	16
	Outer voltage	9	10	0
10cm Focal length	Maximum quartic coefficient	1.03×10^{-11} λ ~ 1.95	4.3×10^{-12} λ ~ 0.81	9.1×10^{-12} λ ~ 1.72
	Inner voltage	57	49	92
	Outer voltage	118	70	152
	Minimum quartic coefficient	-5.7×10^{-12} λ ~ -1.1	-4.4×10^{-12} λ ~ -0.83	-4.1×10^{-12} λ ~ -0.78
	Inner voltage	69	53	94
	Outer voltage	0	0	0

The effect of perimeter modification on spherical aberration for a mirror under a uniform actuation voltage is shown in figure 5-13. Sacrificial layer thickness is 0.2μm for the non-segmented and 10% segmented mirror. The thinned mirror has a 0.4μm sacrificial layer spacing, causing the initial positive spherical aberration. The overall effect of the sacrificial layer thickness is to shift the curve to the right on the graph. The cavity depth for the segmented and non-segmented mirrors is 7μm and for the thinned mirror 9μm. The deeper cavity depth requires a larger actuation voltage and non-linear cavity depth effects will be less for the thinned mirror at a given displacement. This may explain the lower spherical aberration for the thinned mirror. Weakening of the perimeter is seen to have a mitigating influence on the spherical aberration for mirror displacements up to 1.2μm. The optical spherical aberration exceeds $\lambda/10$ at 0.35, 0.96, and 1.12μm of displacement for the non-segmented (100%), segmented (10%), and non-segmented, thinned mirror boundary respectively.

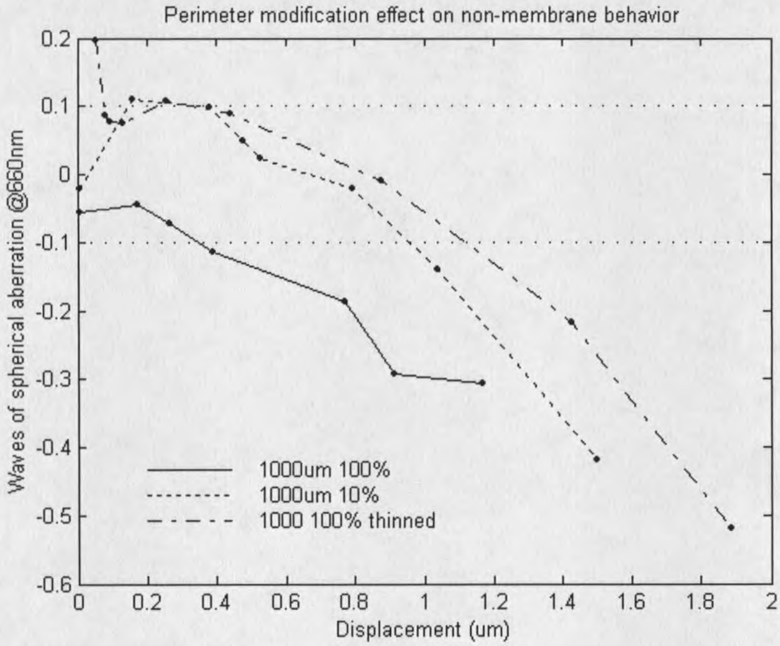

Figure 5- 13. Influence of perimeter modifications on non-membrane behavior under uniform loading. Waves of spherical aberration at 660nm illumination are plotted vs center displacement of 1000μm mirrors for the three perimeter variations. Air cavity depth is 7μm for the segmented and non-segmented mirrors. Cavity depth is 9μm for the thinned mirror.

Actuation

Electrostatic actuation is used to deform the mirrors. By applying a voltage between the top surface of the deformable mirror and the underlying substrate, the electrostatic field, created by the voltage difference, causes mirror deformation. As discussed in chapter 2 in the actuation theory section, this force is always attractive and is given by equation (2-8) for parallel plate capacitor geometry. For small deflections under uniform loading, the deflection varies linearly with applied pressure, ($z \alpha P$) where z is the displacement and P denotes the applied pressure. For large deflections under uniform loading, the deflection-loading relationship changes to the deflection varying as the cubed root of the load ($z \sim P^{1/3}$)[46]. Residual stress influences at what load the transition between small deflection and large deflection behavior occurs. The large deflection behavior is not observed with the mirrors under examination due to the large residual stress. Different voltages on the inner and outer zones, perimeter modifications, and the effect of non-uniform cavity depth further complicate the deflection-load relationship.

In figures 5-14 and 5-15 the mirror center deflection verses applied uniform pressure is graphed. Data for 750μm, 1000μm, and 1500μm diameter mirrors are shown with corresponding lines given by first-order, polynomial fits of the data. These pressure-displacement lines predict the deflection-pressure ratio for each of the mirrors. Also plotted on the graph is a line representing maximum deflection possible as a function of applied pressure. This curve is calculated assuming a maximum sustainable voltage of 250 volts between the plate and the substrate, It also assumes that the maximum deflection occurs at the point of snapdown, when the displacement is equal to 1/3 the cavity depth. The right vertical axis indicates cavity depth corresponding to three times the displacements indicated by the left vertical axis. The intersection of a particular displacement vs. pressure curve for a mirror with the maximum displacement line provides the maximum displacement possible for that mirror design, at an applied voltage of 250 volts, and also the optimum cavity depth to achieve this displacement. For our nitride mirrors, the residual stress keeps the deflection in the linear deflection regime.

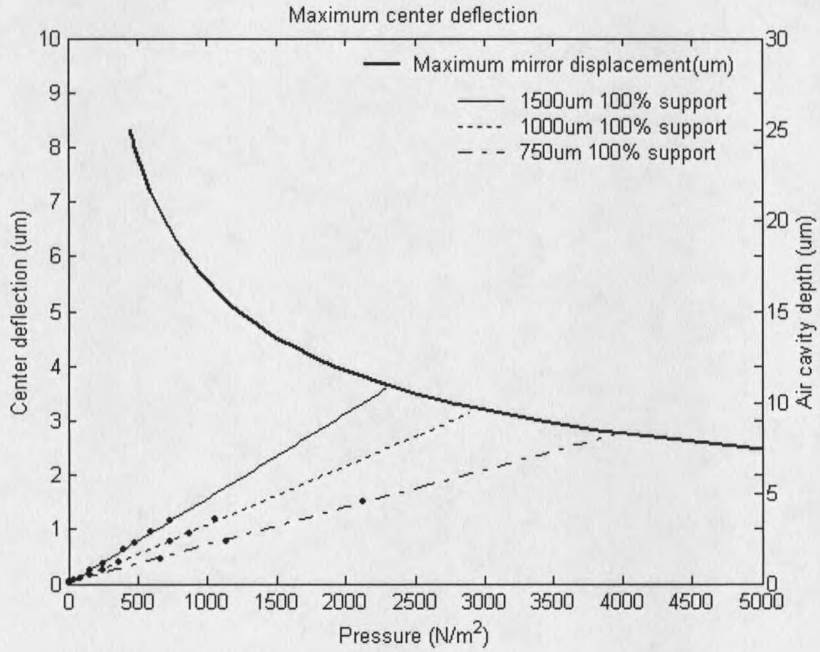

Figure 5- 14. Plot of center deflection vs applied uniform pressure for 1500μm, 1000μm, and 750μm diameter mirrors. The largest center deflection for a maximum applied uniform voltage of 250 Volts is given by the intersection points.

For the non-segmented 1500, 1000, and 750μm mirrors, the optimal cavity depths are 10.9, 9.7, and 8.3μm respectively. The increased maximum deflection distance with mirror diameter is due to the maximum pressure limit, smaller diameter mirrors require more pressure to achieve the same deflection. From the nonlinear theoretical work of Sheplak and Dugundji[28] the increased linearization of the displacement-pressure relationship can be seen from pressure load charts with incremental residual stress curves shown in their cited work. For a 1500μm diameter plate with 100MPa of residual stress, the maximum pressure before the onset of nonlinear deflection is approximately 6400Pa; a corresponding deflection would be 7.8μm. For comparison, the transition for a 1500μm plate with zero initial tension is approximately 2.5Pa, giving a deflection of 0.44μm.

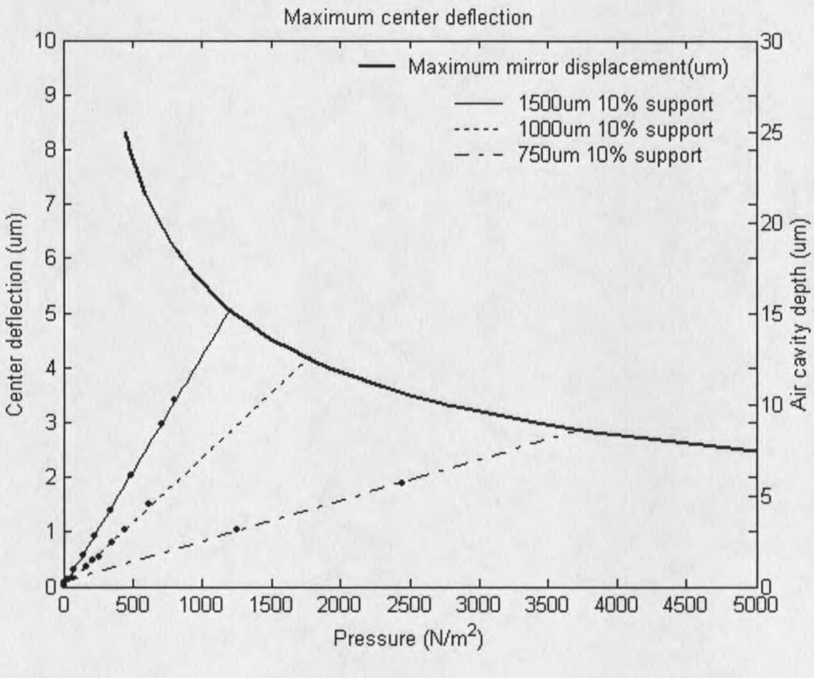

Figure 5- 15. Plot of center deflection vs applied uniform pressure for a 1500μm, 1000μm, and 750μm diameter mirror with 10% segmented support. The largest center deflection for a maximum applied uniform voltage of 250 Volts is given by the intersection points.

Increased maximum deflection is seen for the three segmented mirrors plotted in figure 5-15. For the 10% segmented 1500, 1000, and 750μm mirrors, the optimal cavity depths are 15.1, 12.5, and 8.6μm respectively. This result can be related to the pressure-deflection behavior of the deformable mirrors. Segmenting and thinning the perimeter both have the effect of reducing the pressure required for a given deflection. The results for segmentation are given in table 5-3 for 1500 and 1000μ mirrors at a maximum deflection given by 250 applied volts. A comparison of the effect of perimeter modification on the pressure-deflection behavior is shown directly in figure 5-16. Data for 1000μm mirrors with 100% support, 10% support, and thinned with 100% support are shown. The ratio of pressure to deflection for the non-segmented, non-thinned mirror is 0.0011μm/Pa, for the thinned mirror 0.0012μm/Pa, and for the segmented mirror 0.0024μm/Pa.

Table 5-4. Maximum possible deflections of 1500, 1000, 750μm diameter mirrors for a uniformly applied 250Volt voltage limit.

	100% support		10% support	
	Maximum Deflection (μm)	Pressure (Pa)	Maximum Deflection (μm)	Pressure (Pa)
1500	3.6	2320	5	1200
1000	3.2	2970	4.2	1770
750	2.8	4020	2.9	3740

An approximate, maximum differential voltage between the inner and outer electrodes has been measured to be less than 300 volts. Shorting between electrodes occurs for voltages higher than this due to several possible causes: Paschen breakdown (ionization of the air), a surface current arising from surface contamination, or dielectric breakdown of the insulating material. Optimization of the differential voltage limit is possible by increasing the spacing between electrodes. At one atmosphere of pressure the minimum sustained electric field for breakdown occurs in the vicinity of five microns.[47]

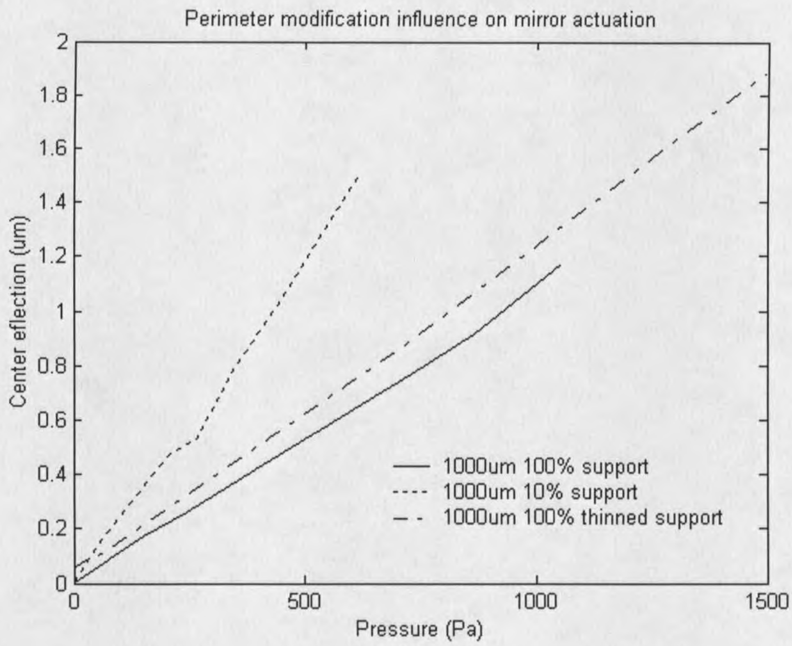

Figure 5- 16. Actuation data of a 1000μm mirror with and without perimeter modifications are shown. Segmentation clearly reduces the required pressure for deflection. Additionally, the segmented mirror retains linear pressure-load behavior as was expected for the mirror without any perimeter modification.

Dynamic Behavior

The dynamic behavior of the deformable mirrors is dominated by the mechanical resonance of the nitride plates. From mechanical plate theory it can be shown that the effect of the residual stress is to increase the resonant frequencies of the mirrors from values expected for plates without initial stress.[48]

The cavity depth does not directly affect the bandwidth of the mirrors but can have an effect on the damping experienced by the devices. For this reason, displacement of the devices during measurement was minimized.

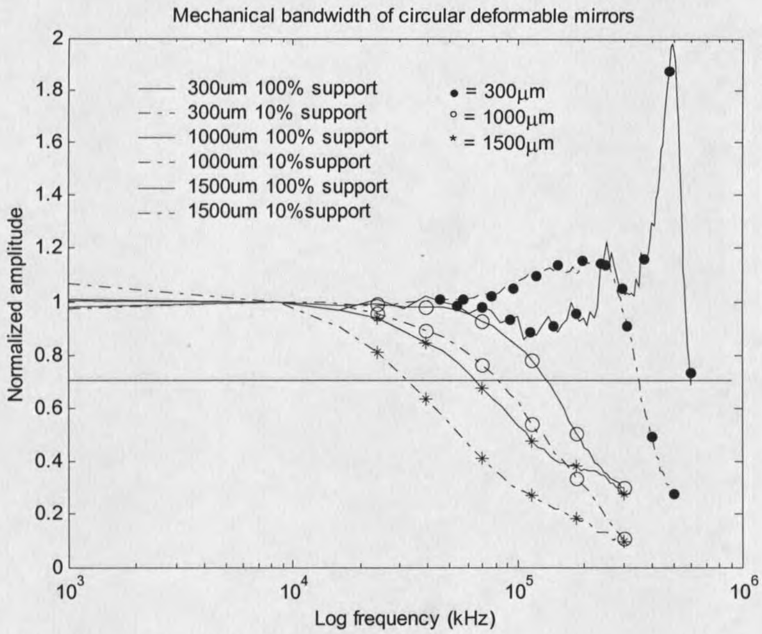

Figure 5- 17. Deformable mirror 3dB bandwidth.

Figure 5-17 shows frequency response data for the deformable mirrors with varying diameters and perimeter modifications. The mirror data are denoted by * for the 1500μm mirrors, ○ for the 1000μm mirrors and • for the 300μm mirrors. Non-segmented and segmented mirror data are differentiated with a solid line for the non-segmented data and a dashed line for the 10% supported mirror data. Figure 5-17 shows that all segmented mirrors have lower 3dB bandwidths than the non-segmented mirrors. The larger diameter mirrors have a lower bandwidth as predicted by mechanical plate theory. Resonant peaks are visible for the 300μm diameter mirrors. In the 300μm non-segmented mirror curve the small peak at ~250kHz may be a sub-harmonic of the main resonance. This resonance feature was not observed for the 1000 and 1500μm diameter mirrors.

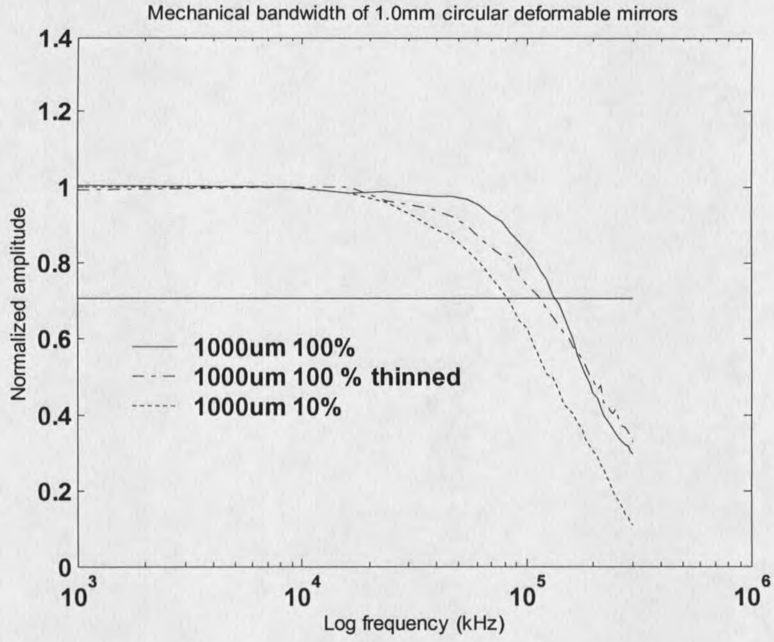

Figure 5- 18. Influence of perimeter modification on 1.0mm mirror bandwidths.

As shown in figure 5-18, thinning the perimeter of the 1mm diameter mirror lowers the bandwidth of the mirror by 13% while segmenting the mirror 10% lowers the bandwidth by 40%. The 3dB bandwidths for the three devices are given in table 5-3.

The fundamental mode of oscillation for the mirrors is a single drumhead mode. That this mode dominates is supported by the predicted resonances of the next higher order drumhead modes.[49] The next highest mode occurs at a frequency 1.6x the fundemental. The next highest symmetric mode (which would be excited by the symmetric electrode geometry) is at 2.3x the fundemental. For a 1mm non-segmented mirror this mode would occur at 305 kHz (predicted by membrane theory).

Table 5-5. Frequency response data for 1μm thick silicon nitride deformable mirrors. Data is measured 3dB decay of focus response to a bipolar sinusoidal load.

3dB bandwidth of circular devices (kHz)			
Mirror diameter	1.5mm	1mm	300um
Non-segmented	64	133	600
Thinned	50	115	n.a.
10% segmentation	32	80	350

Reflectance

The reflectance of the deformable mirror must be sufficient for the intended application. For imaging, available optical power will determine an acceptable reflectance. Optical energy that becomes scattered light can cause degradation in the imaging of an optical system if appropriate blocking apertures are not present. The deformable mirrors have reflectance losses associated with the reflectivity of the metal coating, surface roughness, and the release vias in the mirror surface.

The intrinsic reflectivity of the metal layer causes absorption of the optical energy and becomes important for high power or low intensity applications. For the intended imaging applications, this absorption is not large enough to cause concern. Surface roughness of the deformable mirrors is approximately 3nm RMS measured with a Digital Instruments IIIA atomic force microscope (AFM). This is sufficient for our application.

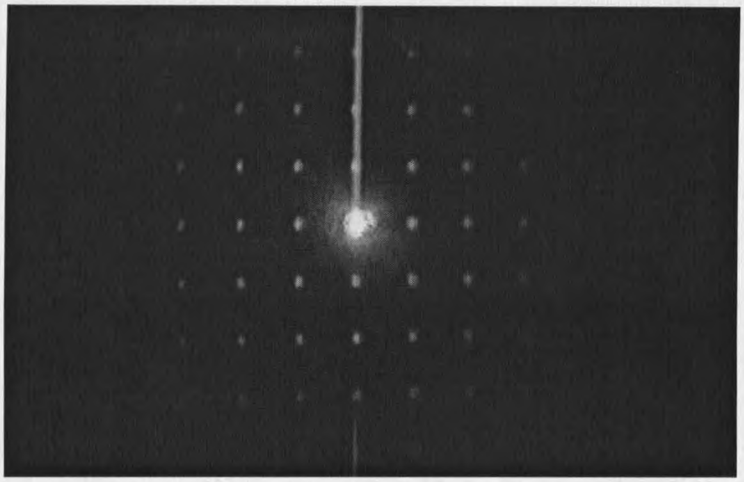

Figure 5- 19. Diffraction pattern from a 1.5mm deformable mirror. The bright vertical line results from saturation of the CCD caused by the central reflection spot.

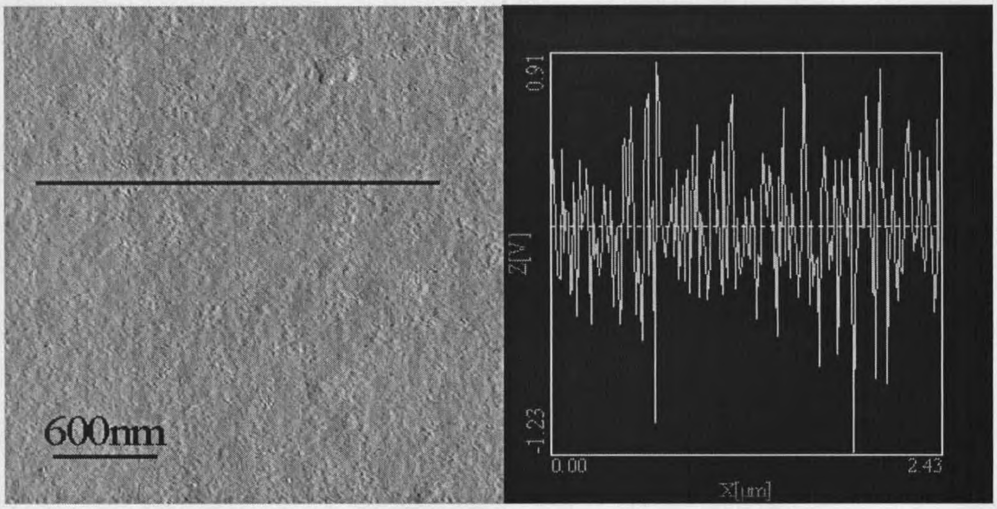

Figure 5- 20. AFM amplitude map of a 3x3 μm area on the mirror surface. The surface profile for the black horizontal line in the left hand figure is given in the right side figure. The vertical scale for the right side graph is nanometers.

The primary optical loss from the deformable mirrors is due to diffraction caused by the release vias. These vias are 5μm square with a 30μm center-to-center spacing.

Measured reflectivity loss due to diffraction is approximately 4% at 632 nm. The realized reflectivity of the deformable mirrors including scattering is 94%, relative to a reference gold mirror.

CHAPTER 6

CONCLUSION

Introduction

Using a modified surface micromaching process, novel micro-optic silicon nitride deformable mirrors have been successfully fabricated and operated. Characterization of surface figure and frequency response has been performed with regard to the mirror's dependence on process and design variables. Deformable mirrors ranging in size from 1500μm to 300μm in diameter have focal adjustment from 11cm with 2 waves of spherical aberration correction to 0.3cm with 1.5 waves of spherical aberration correction respectively. Mirror 3dB frequency ranges from 32kHz, for a 1500μm segmented mirror, to 600kHz for a 300μm non-segmented mirror. These mirror properties make them uniquely suited to provide focus control in real-time imaging and display applications. Subsequent design, fabrication, and release processing modifications based on these characterization results (discussed in chapter 5) allow these deformable mirrors to be built, satisfying specified system integration requirements.

Silicon nitride surface micromachining process

The cavity depth determines the ultimate deflection distance and the load that can be applied to the mirrors. Surface micromachined devices using the standard release process were limited to a range of motion one-third that of the sacrificial layer thickness with practical deflection distances of less than 1μm being typical. The release process is modified by using bulk silicon etching following the standard sacrificial oxide release etch. This release process allows sacrificial oxide thickness to be varied without affecting the actuation range of the mirror. The cavity depths beneath the mirrors can be set based on the desired actuation range.

Tailoring the thickness of the sacrificial layer allows a thin sacrificial layer to be incorporated into the design. Thinning the sacrificial layer is beneficial for two reasons: mirrors have flatter initial curvature and deformable mirrors with higher intrinsic stress can be released. A non-actuated 750μm mirror with 0.7μm of PSG has a focal length of 70cm with 0.22 waves of optical spherical aberration at 660nm illumination. Mirrors with 0.4 and 0.2μm of PSG have initial focal lengths greater than 1.4m, limited by measurement accuracy. Spherical aberration of the 0.4μm PSG mirror was 0.14 waves. Device yield improved when sacrificial oxide thickness was reduced from 0.7 μm to 0.2 μm.

The bulk silicon etch was also a source of structural failures. Hydrogen gas, a byproduct of the silicon etch, accumulats beneath the mirror and forms large bubbles, eventually causing structural failure of the silicon nitride structural layer. Most failures occurred with the non-segmented mirrors where 5μm square vias are the sole opening for the escaping hydrogen from beneath the mirror. With the addition of a surfactant combined with slower silicon etching, all mirrors ranging from 300μm diameter to 1500 μm diameter both segmented and non-segmented, have been successfully released.

Device parameter's impact on performance

A deformable mirrors performance is determined by focal range, spherical aberration, frequency response, reflectivity and operational voltage of the mirror. The design parameters evaluated are actuation zones and perimeter weakening. Mirror actuation voltage, surface figure and frequency response are the deformable mirror's performance criteria used to determine the suitability of using a mirror in an optical system.

Surface Figure

Adequate control of the deformable mirror's surface figure, with regards to zero aberration focus control, is obtained using two annular actuation zones. The compliance of the 1000μm segmented mirror's perimeter results in increased focus for the same center electrode pressure and a greater sensitivity of spherical aberration to the outer electrode load. Performance gains in actuation through the use of segmentation are evident in pressure-displacement curves shown in figure 5-14 and 5-15. The improvement with mirror diameter is due to the higher pressure necessary to deflect smaller diameter mirrors.

Dynamic behavior

Implementation of the deformable mirrors into beam scanning systems requires a bandwidth at least twice that of the line scanning rate. For SVGA video this lower limit is approximately 40kHz. The mechanical frequency response of the mirrors must then be greater than this bandwidth. The minimum 3dB frequency of the devices tested is for the

1.5mm 10% segmented mirror with a 3dB frequency of 32kHz. All other mirrors have resonant frequencies well above the desired limit.

Operation of the mirrors at a constant voltage poses instability problems due to charge migration effects in the silicon nitride structural layer. The effect of this charge migration is drift of the mirror's focal length over time. The shift is due to limited conduction in the silicon nitride dielectric layer. This charge drift can be eliminated using a high frequency AC voltage actuation source. A constant focal length is then produced by actuating the mirrors using an AC voltage at a frequency well above the mirror's 3dB frequency.

Future work

Future work with the deformable mirrors entailes new geometries for specific optical applications and variation of processing to tailor specific performance attributes. Applications outside of beam scanning systems can also be explored.

Alternate geometries

Several possible geometries can be used to implement deformable mirrors into an optical system. Two alternate techniques for implementation of the deformable mirrors into an optical system are the use of a center hole in the mirror coupled with a retro-reflector and an off-axis parabolic reflector.

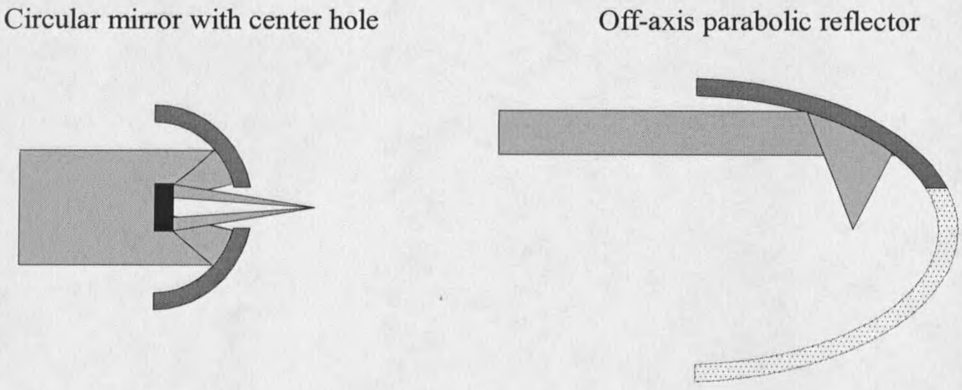

Figure 6-1. Alternate geometries of deformable mirrors. a)Mirror with center hole used in conjunction with a flat reflector. b) An off-axis parabolic reflector

Optical aberrations in addition to field curvature and spherical aberration can be corrected using deformable mirrors. To correct astigmatism, rectangular mirrors supported along two opposite boundaries will deform along a single axis, allowing astigmatism along one orientation to be corrected. Asymmetric electrode placement may allow for correction of coma.[22]

Process variations

Variations in process conditions, materials, and techniques should enable the deformable mirrors discussed in this dissertation to be implemented in a wider variety of optical systems. Benefits from process variations may include: reduction in actuation voltage, larger deflection distance, and higher reflectivity.

Residual stress plays an important role in the behavior of the deformable mirrors studied in this project. Surface curvature, actuation response and dynamic behavior are all influenced by the level of residual stress in the mirrors. Lowering the stress would provide benefits in terms of reducing the applied pressure (a.k.a. voltage) needed to achieve a given deflection and by increasing the device yield. Detrimental effects include a decrease of the mechanical resonance of the mirrors

An increase in reflectivity is possible for particular wavelengths by changing the metal used for the actuation and reflective surface. Using the current processing technique, the metal surface must survive the sacrificial PSG etch and the silicon etch. Aluminum can withstand the PSG etch. And aluminum can survive the bulk silicon etch, with the appropriate additives. Another method, allowing different metals to be used, is an additional low temperature protective layer deposition, after the metal deposition, that would create a protective coating over the aluminum.

Electrostatic actuation used for the deformable mirrors is a primary technique used to manipulate micromachined devices. A limiting factor of electrostatic actuation is that the applied force is unidirectional with only attractive forces possible. Actuation may be improved by the use of a net charge in a dielectric layer. In this manner, repulsion is possible between two electrodes, allowing convex and concave surface shapes to be formed. This requires an active electron injection technique or dielectrics that can retain a net charge to form one electrode. If the structural layer of the deformable mirror could be charged in such a manner, other useful surface could be created.

Applications

Flat and parabolic micro-mirrors have been used in applications such as Fabry-Perot interferometers as sensors and filters.[50,51] With only outer electrode actuation, these deformable mirrors deform with a flat central portion. Because the mirrors deforms in this way they can be used as a mirror in an interference cavity. A deformable mirror with parabolic curvature used in conjunction with a flat mirror forms a micro-resonator. A high finesse cavity would require that the reflectivity could be improved. To improve reflectivity, dielectric stacks can be deposited on micro-mirrors without adversely affecting initial mirror curvature.[52]

Medical diagnostic instruments for in-vivo examinations of biological systems are being developed that use optical imaging systems. Some diagnostic techniques, such as optical coherence tomography (OCT) have fixed focal length imaging systems and their performance could be improved with focus adjustment. Other instruments such as confocal microscopes are being miniaturized. The present technique of controlling focus, via mechanical movement of the sample stage, is not readily scalable. Use of deformable membrane technology could add focus control to such devices without any bulk moving parts.

BIBLIOGRAPHY

[1] H. W. Babcock, "The possibility of compensating atmospheric seeing", Publications of the Astronomical Society of the Pacific,Vol. 65, No. 386, p. 229-236, 1953
[2] Kenneth R. Spring, Mortimer Abramowitz, and Michael W. Davidson, Olympus Microscopy Resource Center, http://www.olympusmicro.com/primer/anatomy/objectives.html
[3] John Hardy, "Active Optics: A new technology for the control of light", Invited paper, Proceedings of the IEEE, Vol 66, No 6. June 1978, pg. 651-697
[4] Robert Tyson, "Principles of adaptive optics",pp 36-37, Academic Press Inc., ISBN 0-12-705900-8, 1991
[5] Lijun Zhu, Pang—Chen Sun, Dirk-Uwe Bartsch, William Freeman, and Yeshaiahu Fainman, "Adaptive Control of a micromachined continuous-membrane deformable mirror for aberration correction", Applied Optics, Vol. 38, No. 1, January 1999, pp.168-176
[6] Glab Vdovin and P.M. Sarro, "Flexible mirror micromachined in silicon" Applied Optics, Vol. 34, No. 16, June 1995, pp. 2968-2972
[7] Thomas Bifano, Raji Krishnamoorthy Mall, John Kyle Dorton, Julie Perreault, Neisimar Vandell, Mark Horenstein, and David Castanon, "Continuous-membrane surface-micromachined silicon deformable mirror", Optical Engineering, Vol. 36, No. 5, may 1997, pp. 1354-1360
[8] Adisorn Tuantranont and Victor M. Bright, "Segmented Silicon-Micromachined Microelectromechanical Deformable Mirrors for Adaptice Optics", IEEE journal on selected topics in quantum electronics, Vol. 8, No. 1, January 2002, pp.33-45
[9] Michael Roggeman, Victor Bright, Byron Welsh, William Cowan and Max Lee, "Micro-electro-mechanical deformable mirrors for aberration control in optical systems", Optical and Quantum Electronics, Vol. 31, 1999, pp.451-468
[10] Gleb Vdovin, "Quick focusing of imaging optics using micromachined adaptive mirrors", Optics Communications,Vol. 140, August 1997, pp. 187-190
[11] M.L. Plett, D.W. Rush, P.R. Barbier, and P. Polak-Dingels, "Blind optimization of optical power into a single mode optical fiber using a mems deformable mirror", Adaptive optics for industry and medicine, Editor Gordon Love, University of Durham, World Scientific, England July 12-16, 1999
[12] F. Gonte, A. Courteville, E. Rochat, K. Haroud, N. Collings, R. Dandliker, G. Vdovin, and S. Sakarya, "High power laser diode to fiber coupling using a membrane mirror", Proc. of the 2nd International workshop on adaptive optics for Industry and medicine: University of Durham, England 12-16 July 1999, Gordon D Love editor, World Scientific 1999.
[13] Yves-Alain Peter, Frederic Gonte, Hans Peter Herzig, and Rene Dandliker, "Micro-optical fiber switch for a large number of interconnects using a deformable mirror", IEEE photonics Technology Letters, Vol. 14, No. 3, March 2002

[14] R.M. Boysel, T.G. Mcdonald, G.A. Magel, G.C. Smith, and J.L. Leonard, "Integration of deformable mirror devices with optical fibers and waveguides", SPIE volume 1793 Integrated Optics and Microstructures, 1992

[15] Vincent Laude, "Twisted-nematic liquid-crystal pixilated active lens", Optics Communications 153, July 15, 1998, pp. 134-152

[16] Ariel Kaplan, Nir Friedman, and Nir Davidson, "Acoustic-optic lens with very fast focus scanning", Optics Letters, Vol. 26, No. 14, July 15, 2001, pp.1078-1080

[17] Si-Hong Ahn and Yong-Kweon Kim, "Proposal of human eye's crystalline lens-like variable focusing lens", Sensors and Actuators A, Vol. 78, 1999, pp. 48-53

[18] Takashi Kaneko, Takuhiro Ohmi, Nobuyuki Ohya, and Nobuaki Kawahara, "A new, compact and quick-response dynamic focusing lens", IEEE transducers 1997, International conference on solid state sensors and actuators, Chicago, June 16-19, 1997, pp.63-66

[19] B.R. Peters, P.J. Reardon, and J.K.Wong, "Preliminary investigation of an active PLZT lens", Proceedings of SPIE, Integrated Optics Devices V, Vol 4277, 2001

[20] D.M. Burns, and V.M. Bright, "Micro-electro-mechanical focusing mirrors", Proceedings of the IEEE Microelectromechanical Systems(MEMS), Jan. 25-29, 1998, pp.460-465

[21] Mark J. Mescher, Michael L. Vladimer, and Jonathan J. Bernstein, "A novel high-speed piezoelectric deformable varifocal mirror for optical applications", MEMS 2002; the fifteenth IEEE international conference on microelectromechanical systems, Las Vegas, Nevada, Jan. 20, pp. 511-515

[22] David Dickensheets, Paul Ashcraft and Phillip Himmer, "Pixel-by-pixel aberration correction for scanned beam micro-optical instruments", Proceedings of the SPIE 3878, 48 Santa Clara, Ca., 1999

[23] David Dickensheets and Gordon Kino, "Silicon-micromachined scanning confocal optical microscope", IEEE Journal of Microelectromechanical Systems, vol. 7,no. 1, pp. 37-48, March 1998

[24] David Dickensheets, Phillip Himmer, Robert Friholm, B. Jeffery Lutzerberger, "Miniature high-resolution imaging system with 3-dimensional MOEMS beam scanning for Mars exploration", Proceedings of the SPIE conference on Micromachining and Microfabrication, Santa Clara, Ca., Sept. 18-20, 2000

[25] Alan C. Traub, "Stereoscopic Display Using Rapid Varifocal Mirror Oscillations", Applied Optics, Vol 6, No. 6, June 1967, pp. 1085-1087

[26] J. C. Muirhead, "Variable focal length mirrors", Rev Scientific Instruments, Vol. 32, p. 210 ,1961

[27] Virendra N. Mahajan, Aberration theory made simple, SPIE optical engineering Press, Vol TT6, 1991, pp. 55

[28] Sheplak M. and Dugundji J.,"Large Deflections of Clamped Circular Plates Under Initail Tension and Transitions to Membrane Behavior", Journal of Applied Mechanics **65**, 107 (1998)

[29] Xing Yang, Frances M. Siu, and Yu-Chong Tai, "Strength of surface micromachined Diaphragms", MRS Spring Meeting, San Francisco, April 12, 1998
[30] Osamu Tabata, Ryouji Asahi, Hirofumi Funabashi, Keiichi Shimaoka and Susumu Sugiyama, "Anisotropic etching of silicon in TMAH solutions", Sensors and Actuators A, Vol 34, 1992, pp. 51-57
[31] E.Bassous, "Fabrication of novel three-dimensional microstructures by the anisotropic etching of (100) and (110) silicon", IEEE transactions on electron devices, Vol ed-25, No. 10, October 1978, pp. 1178-1184
[32] http://snf.stanford.edu/Equipment/ultratech/ultratech.html
[33] M. Stadtmueller, "Mechanical Stress of CVD-Dielectrics", J. Electrochemical Society, Vol 139, No. 12, December 1992
[34] Gregory T.A. Kovacs, "Micromachined Transducers Sourcebook", McGraw Hill1, 1998, ISBN 0-07-290722-3, p. 83
[35] P.J. French, P.M. Sarro, R. Mallee, E.J.M. Fakkeldij, and R.F. Wolffenbuttel, "Optimization of a low-stress silicon nitride process for surface-micromachined applications", Sensors and Actuators A, Vol. 58, 1997, pp. 149-157
[36] Sze S. M., "Physics of Semiconductor Devices", 2ed, John Wiley and Sons, 1981, pg 304
[37] "Etch Rates for Micromachining Processing", Kirt Williams and Richard Muller, IEEE Journal of Microelectromechanical Systems, Vol. 5, No. 4, 1996
[38] J. Buhler, F.P. Steiner, and H. Bates, "Silicon dioxide sacrificial layer etching in surface micromachining", Journal of Micromechanical microengineering, 7, 1997, pp. R1-R13
[39] S. Qin and H. Wang, "Residual stresses in micro-structures fabricated by the IC-compatible sacrificial layer technique", Mechatronics, vol 8, 1998, p. 427-440
[40] Robert Friholm, "title", Masters Thesis, Montana State Univeristy, 2001
[41] Erno H. Klaassen, Richard J. Reay, Christopher Storment, and Gregory T.A. Kovacs, "Micromachined thermally isolated circuits", Sensors and Actuators A, Vol. 58, 1997, pp. 43-50
[42] M. Paranjape, S. Brida, V. Guarnieri, and M. Zen, "Characterization of TMAHW silicon etchant using Ammonium Persulfate as an oxidizing agent", Canadian Conference of Electrical and Computer Engineering, Edmonton, Canada, May 1999
[43] P.M. Sarro, D. Brida, W. v.d. Vlist, G. Pignatel, S. Brida, "Effect of Surfactant on Surface Quality of Silicon Microstructures Etched in Saturated TMAHW Solutions", Eurosensors XIII, Sept 1999, pg 389-392
[44]M. Paranjape, S. Brida, V. Guarnieri, and M. Zen, "Characterization of TMAHW silicon etchant using Ammonium Persulfate as an oxidizing agent", Canadian Conference of Electrical and Computer Engineering, Edmonton, Canada, May 1999
[45] Bahaa E.A. Saleh and Malvin Carl Teich, "Fundementals of Photonics", John Wiley & Sons, Inc.,1991

[46] Sheplak M. and Dugundji J.,"Large Deflections of Clamped Circular Plates Under Initail Tension and Transitions to Membrane Behavior", Journal of Applied Mechanics **65**, 107 (1998)
[47] M. Madou, "Fundamentals of Microfabrication", CRC Press, Boca Raton, Florida, 1997.
[48] Arthur W. Leissa, "Vibration of Plates", Scientific and Technical Information Division, NASA SP-160,1969
[49] Alexander Fetter and John Drik Walecka, "Theoretical Mechanics of Particles and Continua", McGraw-Hill Publishing Company, 1980
[50]. Jaeheon Han, Jiyoung Kim, Tae-Song Kim and Jeong-Seog Kim, "Performance of Fabry-Perot microcavity structures with corrugated diaphragms", Sensors and Actuators A, vol 79, 2000, p. 162-172
[51]. H. Alause, F. Grasdepot, J.P. Malzac, W. Knap, J. Hermann, "Micromachined optical tunable filter for domestic gas sensors", Sensors and Actuators B, vol 43, 1997, p. 18-23
[52]. Ke Cao, W. Liu, and Joseph Talghader, "Curvature compensation in Micromirrors with High-Reflectivity Optical Coatings", Journal of Microelectromechanical Systems, Vol. 10, No. 3, September 2001